Technical Physics Letters, Vol. 31, No. 12, 2005, pp. 1001–1003. Translated from Pis'ma v Zhurnal Tekhnicheskoĭ Fiziki, Vol. 31, No. 23, 2005, pp. 17–23.

Mass Spectrometry of Carbon Nitride C_3N_4

O. F. Pozdnyakov[a,*], L. N. Blinov[b,], Mohammad Arif[b], A. O. Pozdnyakov[a], S. N. Filippov[a], and A. V. Semencha[b]**

[a] *Ioffe Physicotechnical Institute, Russian Academy of Sciences, St. Petersburg, 194021 Russia*
[b] *St. Petersburg State Polytechnical University, St. Petersburg, 197376 Russia*
*e-mail: * of.pozd@mail.ioffe.ru; ** lnblinov@ftim.spbstu.ru*

Received July 4, 2005

Abstract—Carbon nitride has been synthesized in macroscopic amounts by means of the original method based on an ecologically safe technology using inorganic initial compounds. The product has been characterized by mass spectrometry (MS), X-ray diffraction, and quantitative chemical analysis. The MS and thermochemical data show that stoichiometry of the samples of carbon nitride obtained using the proposed method corresponds to the empirical formula C_3N_4. © *2005 Pleiades Publishing, Inc.*

The possibility of the existence of carbon nitride with the chemical formula C_3N_4, where carbon atoms exhibit sp^2 hybridization, was predicted in 1985 by Cohen [1]. Later, the possible existence of a group of polymorphic modifications of carbon nitride was theoretically substantiated based on quantum-mechanical calculations, and a series of such compounds including α-C_3N_4, β-C_3N_4, cubic C_3N_4, and some others was obtained in experiment [2]. These substances can possess promising (e.g., mechanical) properties.

The results of subsequent investigations showed that the crystalline carbon nitride polymorph β-C_3N_4 is thermodynamically unstable under normal conditions, but the lifetime of this compound in a metastable state is still undetermined [3, 4]. An analysis of the available published data showed that carbon nitride was obtained by various researchers in microscopic amounts and the samples had nonstoichiometric compositions with the general formula $C_3N_{4\pm x}$. The syntheses were performed in most cases by chemical deposition from a gas phase containing nitrogen and carbon, whereby the products were obtained in the form of a fine disperse powder or thin films [5–10]. The films were most frequently deposited onto substrates made of metals, quartz, silicon and germanium single crystals, and some other semiconducting materials.

The interest in the synthesis of C_3N_4 is related mostly to the fact that this material possesses extremely high hardness comparable with that of diamond and, hence, can be used for obtaining superhard coatings on the surface of tools, instruments, and various articles including prostheses, etc. The main difficulty in the synthesis of C_3N_4 is related to its thermal instability [11], since this compound exhibits decomposition at temperatures above 800°C.

Experimental. Carbon nitride was synthesized using the original method described elsewhere [12–14], which is based on an ecologically safe technology using inorganic initial compounds. The X-ray diffraction measurements were performed on a DRON-2 diffractometer using FeK_α radiation. The content of nitrogen and carbon in the synthesized samples was determined by method of reductive melting in a carrier gas (helium) flow at a temperature of ~2800°C with chromatographic detection. The error of this method of elemental analysis was ±3%. In addition, the carbon content was determined using a CS-200 gas analyzer (LECO, USA) with an IR absorption detector.

The mass-spectrometric thermal analysis (MTA) was carried out using a modified MX-1320 mass spectrometer with direct sample introduction. A sample weighing about 1 mg was placed on an electric-current-heated substrate (a tantalum ribbon with spot-welded thermocouple), introduced into the spectrometer chamber, and placed in the immediate vicinity of the ionization source. The chamber was evacuated to a residual pressure of about 10^{-4} Pa, and the sample was analyzed in one of the two modes: (i) stepwise heating (at an increment of ~50 K) with recording of the mass spectrum of volatile products in each step; (ii) relatively rapid heating (~25 K/s) with recording of the temperature dependence of a selected peak in the mass spectrum of volatile products.

Results and discussion. The quantitative chemical analyses showed that the powdered products of dark-brown color, which were obtained using the proposed method, contained 61 ± 1.8 wt % of nitrogen and 39 ± 1.2 wt % of carbon. These values correspond to a stoichiometric carbon nitride composition of C_3N_4.

Figure 1 shows the typical X-ray diffraction pattern of synthesized carbon nitride, which displays peaks corresponding to reflections from a system of atomic planes with the interplanar distances d = 3.276, 2.506, 2.361, 2.105, 1.875, and 1.613 Å. Montigaud *et al.* [15]

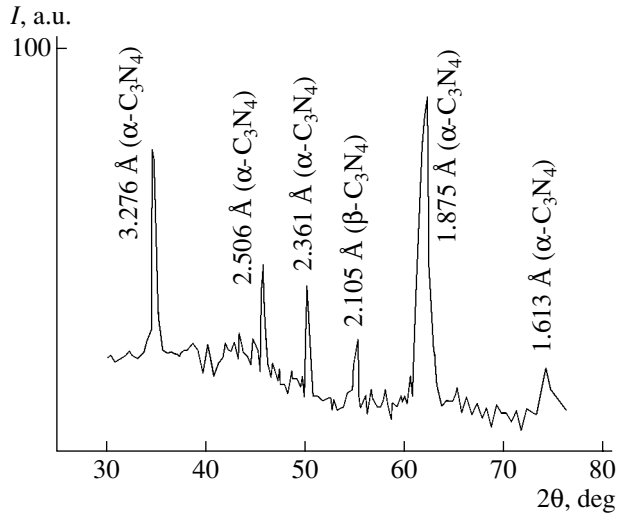

Fig. 1. The X-ray diffractogram of powdered carbon nitride (see the text for explanations).

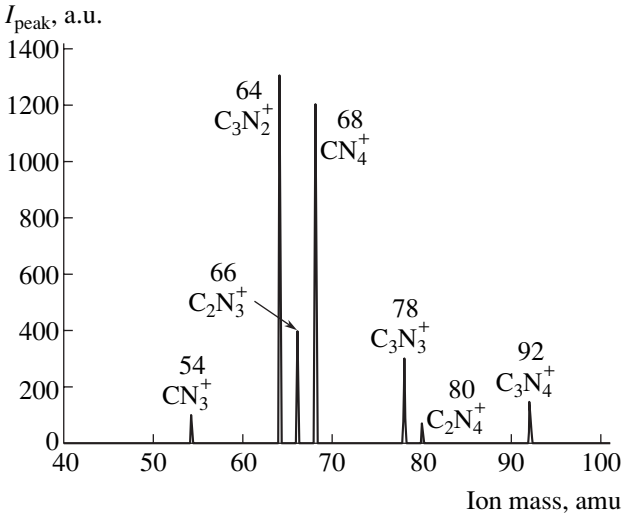

Fig. 2. The mass spectrum of the products of thermal decomposition of carbon nitride at $T = 750$°C.

considered only the peak at 3.27 Å and assigned it to C_3N_4. As can be seen from Fig. 1, our diffractograms of the product contain several peaks. We interpret these peaks as being predominantly due to α-C_3N_4, and this assignment is in good agreement with the data of Hallen *et al.* [16].

The results of MTA allowed the mechanism of thermal decomposition of the synthesized compound to be considered in detail. In interpreting these data, it is necessary to take into account that MTA is a two-fold destructive method. First, the initial sample structure exhibits molecular decomposition on heating, which proceeds according to the special mechanisms of thermolysis. In this process, both "monomeric" structural units (in out case, C_3N_4 molecules) and various fragments of the molecular network (as well as their agglomerates) can be formed. Second, each of these neutral fragments can exhibit dissociation under the action of the ionizing electron impact (electron energy, $E = 70$ eV), which leads (with different probabilities) to the formation of fragment ions constituting the total mass spectrum of the products of thermal decomposition of the initial compound.

Since a reference mass spectrum of the volatile products of thermal decomposition of pure carbon nitride was unavailable, we performed a formal analysis of the set of peaks observed in the mass spectra of samples synthesized by the proposed method. By formal analysis of the mass spectrum, we mean the search for only peaks having even mass to charge (m/z) ratios corresponding to various combinations of C and N atoms (although the volatile products may, in principle, also contain large fragments with $m/z > 92$). In accordance with the published data [17], we consider the structure of carbon nitride as a molecular network consisting of quasi-azine cycles linked via nitrogen atoms. The thermal decomposition of this molecular network begins, as a rule, with the fracture of weak and defect chemical bonds. The high stability of cyclic compounds—in particular, C_3N_4—suggests that their structures are retained with high probability under the conditions of both elevated temperatures and electron impact. Indeed, the mass spectra of the products of C_3N_4 decomposition observed in the temperature interval 500–850°C contain a peak corresponding to ions with a mass of 78 amu ($m/z = 78$). The main peaks in these spectra are assigned to the following species (in the order of decreasing intensity): $m/z = 64$ (C_3N_2), 68 (C_1N_4), 66 (C_2N_3), 78 (C_3N_3), and 92 (C_3N_4) (Fig. 2). In addition, we observed several less intense peaks with different m/z ratios, including those corresponding to ions with odd masses, which are related to features of the synthesis technology, purity of the initial reactants, and incomplete purification of the target product (carbon nitride) from side products. The presence of the peak with $m/z = 78$ indicates that the synthesized product contains C_3N_3, which is the key structural element. The entire combination of peaks in the observed mass spectrum shows that the obtained compound has the chemical formula C_3N_4.

Important supplementary information to the static MTA data, which confirmed the above conclusions, was provided by the results of thermokinetic investigations. Figure 3 shows the typical temperature dependence of the intensity of the peak with $m/z = 78$ characteristic of the azine cycle. The evolution of this cycle was characterized by a bimodal kinetics, with maxima in the 500–700°C and 700–850°C intervals. We believe that this result is indicative of the presence of carbon nitride in at least two states—for example, amorphous and crystalline—in the samples studied. Moreover, we may even suggest with a certain confidence that two crystalline phases probably exist in the second temperature interval. The presence of crystalline phases is

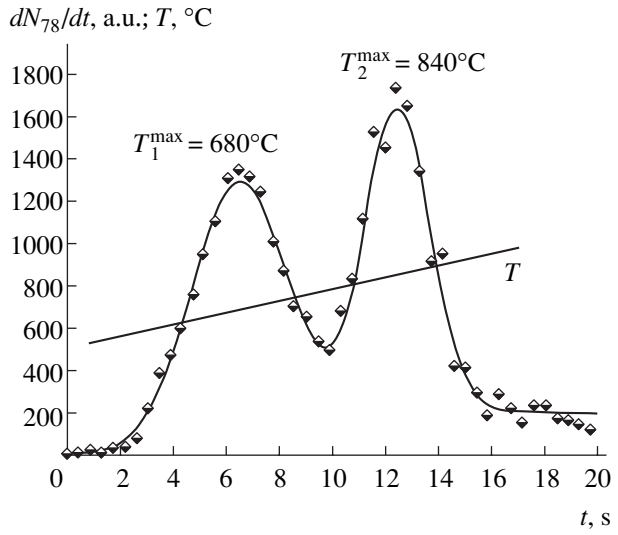

Fig. 3. The temperature dependence of the rate of formation of volatile products during the thermal decomposition of C_3N_4 as reflected by the kinetics of a peak with m/z = 78 in the mass spectrum.

confirmed by the data of X-ray diffraction measurements. We are planning to continue with investigations in this direction.

Acknowledgments. This study was performed within the framework of the program "Novel Materials and Structures" supported by the Department of Physics of the Russian Academy of Sciences.

REFERENCES

1. M. L. Cohen, Phys. Rev. **32**, 7988 (1985).
2. D. M. Teter and R. J. Hewley, US Patent Application No. 005,981,094A (1999).
3. V. V. Odintsov and V. I. Pepekin, Dokl. Akad. Nauk **343**, 210 (1995).
4. J. V. Badding and D. C. Nesting, Chem. Mater. **8**, 535 (1995).
5. M. Sato, H. Niino, Y. Kawaguchi, *et al.*, Jpn. Patent Application No. 2,004,099,982 (2002).
6. Chen Yan, Guo Liping, and Wang En Ge, Chinese Patent No. 1,151,386 (1997).
7. J. Wuning, US Patent No. 4,003,764 (1977).
8. Lee Yun Gwan and Ryu Byeong Gil, Korean Patent No. 00,262,824 (2000).
9. E. L. Galan, F. I. Montero, and S. F. Rueda, Spanish Patent No. 2,138,884 (2000).
10. V. L. Liberman, J. H. Richter, and Y. Yamazaki, US Patent No. 6,658,895 (2003).
11. D. R. Miller, Jianjun Wang, and E. G. Gilian, J. Mater. Chem. **12**, 2463 (2002).
12. L. N. Blinov, Mohammad Arif, O. F. Pozdnyakov, *et al.*, in *Proceedings of the 8th All-Russia Conference on Fundamental Investigations in Technical Universities, St. Petersburg, 2004*, pp. 225–226.
13. Mokhammad Arif, L. N. Blinov, R. Lappalainen, *et al.*, Fiz. Khim. Stekla **30**, 780 (2004).
14. L. N. Blinov, Arif Mokhammad, A. V. Semencha, *et al.*, in *Proceedings of the 12th International Conference "High Intellectual Technologies and Knowledge Generation in Education and Science," St. Petersburg, 2005*, pp. 302–305.
15. H. Montigaud, B. Tanguy, G. Demazeau, *et al.*, J. Mater. Sci. **35**, 2547 (2000).
16. E. E. Hallen, M. L. Cohen, and W. L. Hansen, US Patent Application No. 005,110,679A (1992).
17. V. N. Khabashesku, J. L. Margrave, and J. L. Zimmerman, US Patent No. 6,428,762B1 (2002).

Translated by P. Pozdeev

Technical Physics Letters, Vol. 31, No. 12, 2005, pp. 1004–1006. Translated from Pis'ma v Zhurnal Tekhnicheskoĭ Fiziki, Vol. 31, No. 23, 2005, pp. 24–28.

Features of the Temperature and Concentration Dependences of Resistivity in Disordered Macroscopic Composite Systems of the Insulator–Semiconductor Type

V. A. Sotskov

Kabardino-Balkarian State University, Nalchik, Kabardino-Balkaria, Russia

e-mail: sozkov_va@rambler.ru

Received June 9, 2005

Abstract—The volume resistivity and the imaginary part of the permittivity of a macroscopic composite system of the insulator–semiconductor type have been experimentally studied as functions of the temperature and the content of the semiconductor phase. Specific features in the conductivity of this system are revealed and a qualitative model explaining the observed behavior is proposed. © *2005 Pleiades Publishing, Inc.*

In recent years, percolation systems of the insulator–semiconductor type have been extensively studied using experimental and theoretical methods [1–4]. However, macroscopic systems of this type are also of interest, both from a basic standpoint and in practical applications [1, 2] such as thermistors. This Letter reports the results of experimental investigation of the volume resistivity (ρ) of a macrosystem of the insulator–semiconductor type as a function of the bulk semiconductor content (x) and the temperature (T).

The experiments were performed for an insulator–semiconductor composite with the semiconductor component representing compounds of the A^8B^6 or A^1B^6 types. The former was Fe_2O_3 consisting of nearly spherical particles 25 μm in diameter, and the latter was CuO composed of particles with approximately the same geometry. Prior to mixing and melting the initial charge, particles of Fe_2O_3 powder were demagnetized by the conventional method in an alternating magnetic field. The mixer and other equipment used for the sample preparation and characterization were made of nonmagnetic materials. The insulator component in both composites was paraffin, selected due to its good insulating and technological properties, which made possible the creation of a desired model system [3, 4].

The preparation of samples was described in detail elsewhere [3, 4]. Each sample had the form of a capacitor with solidified paraffin–semiconductor mixture of a certain concentration confined between metal electrodes. The investigation was performed for flat and cylindrical capacitors with electrodes made of pure electrolytic copper. The dc resistance at a preset temperature was measured in the dark by the standard technique using an E6-13A teraohmmeter. The imaginary part of the permittivity (ε") was also determined using conventional methods [2, 4].

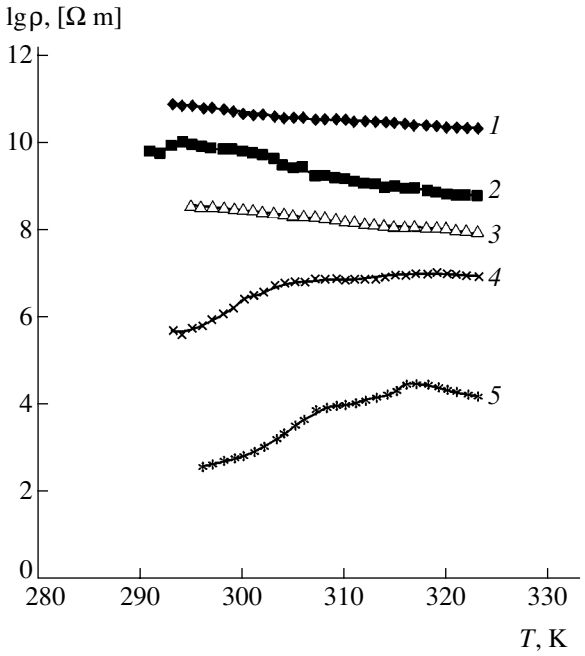

Fig. 1. Plots of the logarithm of resistivity versus temperature for (*1*) a paraffin matrix, (*2*, *3*) paraffin–Fe_2O_3 composites with a bulk Fe_2O_3 content of x = 1.87 and 40.8%, respectively, and (*4*, *5*) paraffin–CuO composites with a bulk CuO content of x = 33 and 56%, respectively.

1063-7850/05/3112-1004$26.00

The results of measurements are presented in Figs. 1 and 2. As can be seen, the resistivity of the paraffin–Fe_2O_3 composite (Fig. 1, curves *1* and *2*) monotonically decreases with increasing temperature. The paraffin–CuO system (Fig. 1, curves *4* and *5*) exhibits the opposite general trend, whereby its resistivity grows with the temperature in most of the same interval. We may suggest that, as the bulk content of the semiconductor filler (Fe_2O_3 and CuO) in the insulating matrix increases, the properties of the composite must approach those of the corresponding semiconductor. Indeed, the temperature coefficient of resistance (TCR) for the maximum concentrations of the semiconductor component was negative for the composites with Fe_2O_3 and positive for those with CuO.

The behavior observed for the resistivity was confirmed by the results of determination of the imaginary part of the permittivity plotted in Fig. 2 as $\lg\varepsilon'' = f(x, T)$ (Fig. 2). For the paraffin–Fe_2O_3 composite, the dielectric losses in the sample capacitor increase with the temperature (Fig. 2, curves *2*, *4*), while those for the paraffin–CuO system (Fig. 2, curves *5* and *6*) either remain virtually constant or decrease with the temperature in the same interval. The total losses in insulators consist of the electric conductivity losses and the relaxation losses [2]. In the case under consideration, the relaxation losses are insignificant and influence the system behavior only at small concentrations of the semiconductor phase [4]. It should be noted that the paraffin matrix proper has a negative TCR (Fig. 1, curve *1*) [4]. The behavior of the paraffin–CuO composite in this respect is analogous to that observed recently for an insulator–conductor (paraffin–graphite) system [4]. The TCR of the paraffin–CuO composites is negative (like that of the pure paraffin) when the CuO concentration in the mixture is relatively small, not exceeding $x = 0.09$, but the TCR changes sign for composites with a greater bulk content of CuO.

The above results suggest that it is possible to develop composite thermistors having both positive and negative TCR, irrespective of the properties of the insulating matrix. However, the function $\lg\rho = f(T)$ of some composites is nonmonotonic, the most typical example being offered by the behavior of the paraffin–56% CuO composite (Fig. 1, curve *5*), for which the TCR is $\alpha = 0.1217$ (296–300 K), 0.3334 (301–307 K), 0.1478 (308–317 K), and –0.1125 (Ω m)/K (318–323 K). Thus, the TCR of certain composites not only significantly varies in magnitude, but can also change sign depending on the temperature. Let us consider the possible factors responsible for the substantial differences in the TCR behavior observed in various temperature intervals.

Paraffin is a molecular crystal [2] and has a definite melting temperature. The concentrations of components are independent of the temperature both in the whole sample and in various local regions, being the same as that in the initial melt. Therefore, we may suggest that a certain specific structural feature of the conducting (fractal) chains, which has been created still in the melt, can subsequently vary at temperatures below the melting point. This variation can be related to the difference in the coefficients of thermal expansion of paraffin and the filler [4]. In particular, we may suggest that the paraffin–Fe_2O_3 composite contains well-developed, "shaggy" branched chain structures having a relatively small number of chain ends ensuring low resistance between adjacent fractals ("blue" contacts on a model pattern) and a large number of chain ends forming fractal contacts with high resistance ("red" contacts) [5]. In the course of heating, the "red" contacts can transform into "blue" ones, which corresponds to the formation of conducting links. It is natural to suggest that (i) the stochastic character of this process accounts for the possibility of both formation and breakage of contacts depending on the temperature and (ii) the rates of these processes can be different in various temperature intervals.

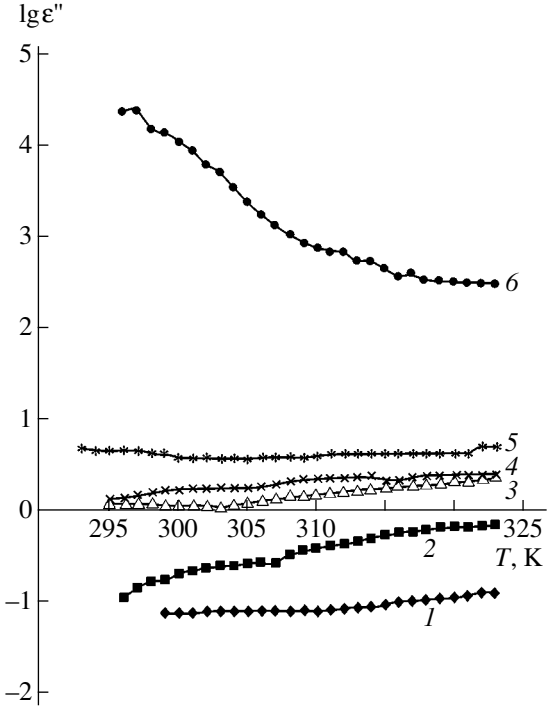

Fig. 2. Plots of the logarithm of the imaginary part of permittivity versus temperature for (*1*) a paraffin matrix, (*2–4*) paraffin–Fe_2O_3 composites with a bulk Fe_2O_3 content of $x = 8.5$, 20.5 and 40.8%, respectively, and (*5*, *6*) paraffin–CuO composites with a bulk CuO content of $x = 17$ and 56%, respectively.

On the contrary, the paraffin–CuO composite is characterized by the formation of "smooth" structures, whereby the side chains at the main conducting channel

are relatively short. In this case, heating of the paraffin matrix leads initially to the breakage of conducting paths. In the temperature interval 318–323 K, where $\alpha = -0.1125$ (Ω m)/K (Fig. 1, curve *5*), the process is reversed, whereby the rate of contact formation becomes greater than the rate of breakage and the branched structures appear. This explanation poses the question as to which properties of the component materials may account for such behavior of the fractal chains. The possible reasons can be of quite different natures, including intermolecular forces and many other factors [4, 5].

REFERENCES

1. E. V. Kharitonov, *Dielectric Materials with Nonuniform Structures* (Radio i Svyaz', Moscow, 1983) [in Russian].
2. V. V. Pasynkov, *Materials for Electronic Technology* (Vysshaya Shkola, Moscow, 1980), pp. 155–160 [in Russian].
3. V. A. Sotskov, Pis'ma Zh. Tekh. Fiz. **30** (11), 38 (2004) [Tech. Phys. Lett. **30**, 461 (2004)].
4. V. A. Sotskov, Fiz. Tekh. Poluprovodn. (St. Petersburg) **39**, 269 (2005) [Semiconductors **39**, 254 (2005)].
5. J. Feder, *Fractals* (Plenum Press, New York, 1988).

Translated by P. Pozdeev

Technical Physics Letters, Vol. 31, No. 12, 2005, pp. 1007–1008. Translated from Pis'ma v Zhurnal Tekhnicheskoĭ Fiziki, Vol. 31, No. 23, 2005, pp. 29–33.

Resonance RF Emission from Water

V. I. Petrosyan

Project "Novel Technologies," Joint-Stock Company, Saratov, Russia
e-mail: mail@pnt-capital.com

Received June 23, 2005

Abstract—The method and results of an experimental investigation of stable intrinsic RF (microwave) emission from water upon EHF 65 GHz ⟶ UHF 1 GHz resonance excitation are described. The Curie point for the radiation quenching is determined at 95°C. The mechanism of emission is explained in terms of conservation of the synchronization and polarization of the superthermal selective oscillations in the molecular system of water, which are induced by a short-term resonance action of linearly polarized EHF radio waves of low intensity. © *2005 Pleiades Publishing, Inc.*

Water—one of the most widely occurring natural substances—exhibits a number of anomalous physical properties, which are of considerable interest from both basic and technological standpoints. This compound is an essential component of the environment and living organisms: for example, the content of water in the human brain reaches ~75%. For these reasons, investigations into the properties of water are important for the possible technical applications and deeper insight into the functioning of living organisms.

In recent years, a high-frequency resonance wave state of the molecular system of water has been discovered, and a number of resonance effects both in water and in the aqueous components of biological media have been observed, which are related to the intrinsic oscillations of molecular structures existing in water. The spectrum of resonance frequencies corresponding to the excitation of this resonance wave state has been determined [1–5].

In the Rayleigh–Jeans long-wavelength spectral region, two selective series of resonance oscillations (25, 50, 100, 150, … and 32, 65, 130, … GHz) and the corresponding low-frequency harmonics (1 GHz and higher) have been separated on a thermal background. According to the author's data, the first series is determined by the frequencies of the natural molecular oscillations of $(H_2O)_6$ hexagonal water clusters, the second series is due to the natural oscillations of three-atomic H_2O molecules, while fractal clusters such as $6(H_2O)_6$ possess fundamental frequencies on the order of 1 GHz [5]. Since water belongs to the so-called associated liquids, the resonance oscillations excited by external radio waves are transferred from one type of structural fragments to another so that the process of mutual excitation of resonance oscillations in the molecular system of water takes place. In contrast to the resonance absorption at the aforementioned fundamental frequencies, water is transparent for radio waves of nonthermal intensity: the process of radiation propagation involves the entire volume of water and the aforementioned resonances are referred to as translational.

This Letter reports the results of investigations into the stable secondary RF (microwave) emission from water upon EHF 65 GHz ⟶ UHF 1 GHz resonance excitation. The aim of this study was to elucidate the mechanism of intrinsic microwave emission, measure the duration of this process, and determine the Curie point of radiation quenching.

The investigation was performed in a screened box with the electromagnetic background suppressed by 30 dB. The experimental arrangement is schematically depicted in Fig. 1. The emission from column *2* of distilled water ($15 \times 15 \times 50$ mm^3) in ampule *1* was detected with the aid of stripe microwave antenna *3*. The experiments used two frequencies from the resonance spectrum of water: an EHF 65 GHz signal was used for the excitation of intrinsic oscillations, while a UHF 1 GHz signal was used for the detection of this secondary RF (microwave) emission. The microwave excitation was provided by oscillator *4* generating linearly polarized EHF radio waves of THE_{01} type with a power of ~1 mW. The secondary microwave signal detected by antenna *3* was measured by microwave radiometer *5* tuned to a central frequency of 1 GHz with a ±25 MHz bandwidth and a threshold sensitivity of 0.3 K. The temperature of water was measured by thermocouple *6*.

The experimental procedure was as follows. Water was preliminarily irradiated by radio waves at EHF 65 GHz for 5 min and then heated for 10 s at a temperature increased with 5°C steps in the interval from 20°C to a temperature of the secondary radiation quenching. After each heating, water in the ampule was cooled to 20°C, antenna *3* was brought in contact with water *2*, and the microwave output signal was measured. In order to exclude uncontrolled external influence, all manipulations and measurements were performed under distant control.

1063-7850/05/3112-1007$26.00 © 2005 Pleiades Publishing, Inc.

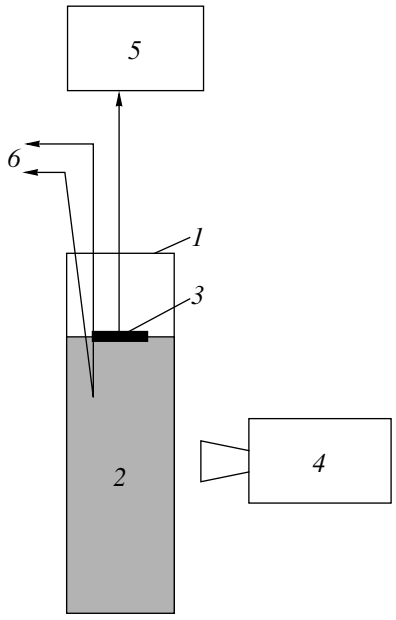

Fig. 1. Schematic diagram of the experimental setup for the investigation of secondary microwave emission from water (see the text for explanations).

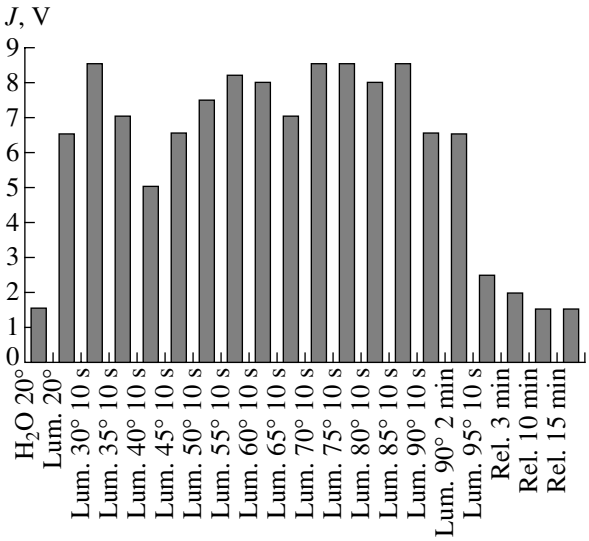

Fig. 2. The temperature-dependent evolution of the EHF-induced UHF microwave emission from water up to the Curie point of radiation quenching.

Figure 2 presents a histogram of the temperature-dependent evolution of the induced microwave emission intensity measured as described above. The measurements were performed on a 100-K sensitivity scale at a voltage responsivity of ~10^{-13} W/(cm^2 V). In order to check for the stability of excited microwave emission near the Curie point, water was doubly (for 10 s and 2 min) heated to a temperature of 90°C. It should be noted that the intrinsic microwave emission from water did not cease during the entire experiment, which lasted typically for about 2 h. The emission continues unless the temperature is increased above the Curie point.

As can be seen from the histogram in Fig. 2, the short-term action of EHF radio waves at a resonance frequency of 65 GHz excites stable secondary intrinsic emission in the microwave range at a natural resonance frequency of 1 GHz. Another interesting feature is a "trough" in the secondary emission intensity observed upon heating of water to 40°C, which falls into the temperature interval of activity of warm-blooded living organisms.

The initial intensity of the EHF-induced microwave emission at 20°C is also stably restored upon heating to 90°C. The radiation quenching takes place at a Curie temperature of ~95°C, after which the initial unexcited state of water is achieved within 10 min. Below the Curie point, the excited intrinsic microwave emission from water is retained for an uncertainly long period of time.

It is believed that the excitation of intrinsic microwave emission from water is related to the synchronization and polarization of intrinsic molecular oscillations induced by an external resonance EHF wave, which eliminates the interference quenching of waves and enhances the resonance emission. In the case under consideration, the intrinsic emission from water is maintained by thermal energy, which is evidenced by a growth of the emission intensity upon heating and by decay in this intensity upon cooling.

REFERENCES

1. V. I. Petrosyan, Yu. V. Gulyaev, E. A. Zhiteneva, *et al.*, Radiotekh. Élektron. (Moscow) **40**, 127 (1995).
2. V. I. Petrosyan, E. A. Zhiteneva, Yu. V. Gulyaev, *et al.*, Radiotekhnika, No. 9, 20 (1996).
3. N. I. Sinitsyn, V. I. Petrosyan, V. A. Yolkin, *et al.*, Crit. Rev. Biomed. Eng. **28**, 5 (2000).
4. V. I. Petrosyan, N. I. Sinitsyn, V. A. Elkin, *et al.*, Elektron. Prom., No. 1, 99 (2000).
5. V. I. Petrosyan, A. V. Maiborodin, S. A. Dubovitskii, *et al.*, Millimetr. Volny Biol. Med., No. 1, 18 (2005).

Translated by P. Pozdeev

Technical Physics Letters, Vol. 31, No. 12, 2005, pp. 1009–1010. Translated from Pis'ma v Zhurnal Tekhnicheskoĭ Fiziki, Vol. 31, No. 23, 2005, pp. 34–38.

Optimized Scheme of a Rubidium All-Optical Frequency Standard

G. A. Kazakov[a,*], B. G. Matisov[a], I. E. Mazets[b], and G. Mileti[c]

[a] *St. Petersburg State Polytechnical University, St. Petersburg, 195251 Russia*
[b] *Ioffe Physicotechnical Institute, St. Petersburg, 194021 Russia*
[c] *Neuchâtel Cantonal Observatory, CH-2000 Neuchâtel, Switzerland*
* *e-mail: kazakov@quark.stu.neva.ru*

Received July 6, 2005

Abstract—A new approach to the creation of a quantum frequency standard based on the phenomenon of coherent population trapping is proposed, which employs linearly polarized radiation and involves signal discrimination at the absorption maximum. © *2005 Pleiades Publishing, Inc.*

In recent years, the creation of quantum frequency standards based on the coherent population trapping (CPT) phenomenon has become an intensively developing field combining basic and applied research [1–6]. The principle of action of the CPT all-optical frequency standard is based on the comparison of the frequency of a quartz oscillator to the frequency of two-photon resonance on a transition between Zeeman sublevels of the ground state, which is insensitive (in the linear approximation) to an external magnetic field. For certainty, below we will consider the sublevels $|F_g = 1, M = 0\rangle$ and $|F_g = 2, M = 0\rangle$ (called working states) of ^{87}Rb atom and the corresponding transition (called 0–0 transition).

Despite considerable effort of numerous research groups, the stability of CPT frequency standards still does not exceed the level achieved in systems employing the traditional schemes of optical pumping [7]. The main obstacle in this respect is a relatively low contrast of dark resonances corresponding to CPT, which results in an insufficiently high figure of merit. Attempts at increasing the fraction of atoms exhibiting CPT in the working states by various means [5] lead to the broadening of dark resonances and the corresponding decrease in the figure of merit.

In this Letter, we propose a new approach to the problem of frequency stabilization. According to this, we suggest to refrain from excitation of the 0–0 resonance and, instead, to compare the frequency of a quartz oscillator to the position of an absorption maximum between two adjacent dark resonances characterized by the total magnetic moment projections $M = \pm 1$.

Let us consider the transmission of a linearly polarized laser radiation through a rubidium vapor cell, the polarization vector being perpendicular to an external homogeneous magnetic field. We assume that the laser frequency is tuned in resonance with the $F_e = 1$ component of the D_1 line of ^{87}Rb atom and split with the aid an electrooptical modulator controlled by a quartz oscillator (it is also possible to use a diode laser with current modulation). The linearly polarized radiation can be represented as a coherent superposition of two fields, with right- and left-hand polarizations relative to the magnetic field direction (this representation is convenient in view of the Zeeman splitting of atomic levels). Using the Wigner–Eckart theorem and the properties of Clebsch–Gordan coefficients [8], one can readily show [9] that no CPT on the working levels takes place under these conditions. At the same time, there are pairs of states $a_1 = \{|F_g = 2, M = +1\rangle, |F_g = 1, M = -1\rangle\}$ and $a_2 = \{|F_g = 2, M = -1\rangle, |F_g = 1, M = +1\rangle\}$ on which CPT is established as a result of the coherent interaction with the excited sublevel $|F_g = 1, M = 0\rangle$ (under the two-photon resonance conditions [10]).

If only the magnetic moment due to the angular momentum of the electron shell is taken into account, the resonance frequencies corresponding to the two-photon transitions inside the pairs of levels a_1 and a_2 coincide with the frequency of the 0–0 transition. However, these frequencies are in fact symmetrically shifted relative to the 0–0 transition frequency because the ^{87}Rb nucleus possesses a magnetic moment. The magnitude of this shift in a weak magnetic field is on the order of 4 kHz/G. As a result, the typical magnitude of splitting of two dark resonances in the magnetic fields with strengths on the order of several tenths of a gauss is equal to the characteristic dark resonance width for a field intensity of 2 mW/cm^2 (typical of the CPT experiments in gas cells). The splitting of dark resonances in a field of such configuration was originally observed for cesium atoms [11] and recently also reported for ^{87}Rb atoms [12, 13].

In practice, it is extremely difficult to create a homogeneous magnetic field with strength below 0.05 G in the entire cell volume [4]. In such a field, dark reso-

1063-7850/05/3112-1009$26.00

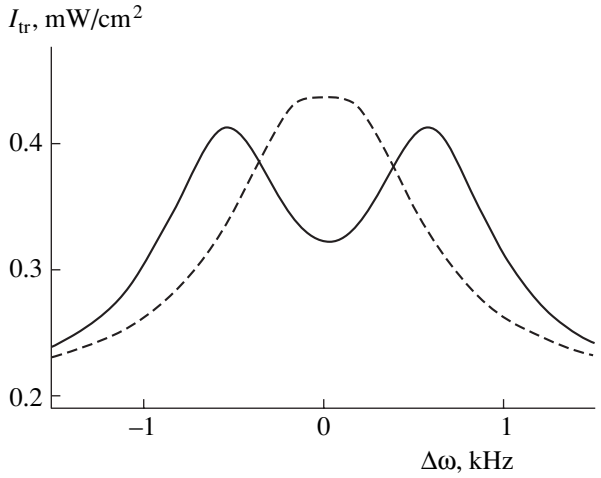

The results of numerical calculations of the intensity I_{tr} of transmitted laser radiation versus detuning Δω of the two-photon transition frequency from the 0–0 resonance frequency for a rubidium cell (see the text for the cell parameters) in a magnetic field of 0.05 G (dashed curve) and 0.2 G (solid curve).

nances with a width of about 1 kHz will not be split. Instead, according to the results of our numerical calculations, a CPT-related minimum in the absorption spectrum appears as "flat." In other words, the slope of the quantum discriminator characteristic (i.e., the second derivative of the laser intensity at the cell output with respect to the oscillator detuning from the 0–0 transition frequency) is much smaller than 1 mW/(cm^2 kHz^2) (the value expected in the absence of magnetic field).

A several-fold increase in the magnetic field intensity will make the dark resonances partly resolved, and an absorption maximum with a quite large contrast will appear between the two minima, exactly at a frequency corresponding to the 0–0 transition. It should be emphasized that there are no special features in excitation of the working levels themselves. Stabilization of the oscillator frequency with respect to this maximum offers a unique possibility to increase the slope of the discriminator characteristic and the length of the linear part of the characteristic curve in the region of their optimum values, thus improving the stability of the rubidium all-optical frequency standard by an order of magnitude in comparison to the presently achieved level.

The results of our numerical calculations of a laser radiation transmission spectrum for a rubidium vapor cell containing a buffer gas are presented in the figure. The buffer gas has to ensure a diffusion coefficient of ^{87}Rb atoms of about 150 cm^2/s (which corresponds to a gas pressure on the order of 1 Torr). The cell has a radius of 1 cm, a length of 3 cm, and operates at a temperature of 50°C. It is assumed that a lens system similar to that described in [4] provides that laser radiation fills the entire cell cross section. The input radiation intensity is 0.5 mW/cm^2. The short-term stability of the all-optical frequency standard based on this cell estimated as described in [7] corresponds to an instability below $10^{-14}/\sqrt{\tau}$ (where τ is the integration time in seconds) for a magnetic field of 0.2 G. This result is much in excess of the best stability level achieved with the frequency standards of the given type [1–6]. In view of the simplicity of the proposed cell design, practical implementation of this approach seems to be quite a real task.

Acknowledgments. The authors are grateful to V.I. Yudin for fruitful discussions.

This study was supported in part by the INTAS–CNES (grant no. 03-53-5175) and the Ministry of Education and Science of the Russian Federation (project no. UR.01.01.287).

REFERENCES

1. J. Kitching, S. Knappe, N. Vukicevic, *et al.*, IEEE Trans. Instrum. Meas. **49**, 1313 (2000).
2. J. Kitching, S. Knappe, and L. Hollberg, Appl. Phys. Lett. **81**, 553 (2002).
3. R. Stahler, R. Wynands, S. Knappe, *et al.*, Opt. Lett. **27**, 1472 (2002).
4. M. Merimaa, T. Lindvall, I. Tittonen, *et al.*, J. Opt. Soc. Am. B **20**, 273 (2003).
5. S. V. Kargapoltsev, J. Kitching, L. Hollberg, *et al.*, Laser Phys. Lett. **1**, 495 (2004).
6. S. Knappe, P. D. D. Schwindt, V. Shah, *et al.*, Opt. Express **13**, 1249 (2005).
7. M. B. Gornyi, B. G. Matisov, G. M. Smirnova, *et al.*, Zh. Tekh. Fiz. **57**, 740 (1987) [Sov. Phys. Tech. Phys. **32**, 448 (1987)].
8. D. A. Varshalovich, A. N. Moskalev, and V. K. Khersonskii, *Quantum Theory of Angular Momentum* (Nauka, Leningrad, 1975; World Scientific, Singapore, 1988).
9. D. V. Kosachev, B. G. Matisov, and Yu. V. Rozhdestvensky, J. Phys. B **25**, 2473 (1992).
10. B. D. Agap'ev, M. B. Gornyi, B. G. Matisov, and Yu. V. Rozhdestvensky, Usp. Fiz. Nauk **163** (9), 1 (1993) [Phys. Usp. **36**, 763 (1993)].
11. S. Knappe, W. Kemp, C. Affolderbach, *et al.*, Phys. Rev. A **61**, 012508 (2000).
12. S. Zibrov, Y. Dudin, V. Velichansky, *et al.*, in *Proceedings of the International Conference on Coherent and Nonlinear Optics Collocated with International Conference on Lasers, Applications, and Technologies ICONO/LAT-2005, St. Petersburg, 2005*, p. ISK8.
13. A. V. Taichenachev, V. I. Yudin, V. L. Velichansky, and S. A. Zibrov, quant-ph/0507090 (2005).

Translated by P. Pozdeev

Technical Physics Letters, Vol. 31, No. 12, 2005, pp. 1011–1014. Translated from Pis'ma v Zhurnal Tekhnicheskoĭ Fiziki, Vol. 31, No. 23, 2005, pp. 39–45.

Reorientation of Local Regions in the Lattice of a Loaded Crystal

E. E. Slyadnikov

Tomsk Scientific Center, Siberian Division, Russian Academy of Sciences, Tomsk, Russia

e-mail: opi@hq.tsc.ru

Received July 20, 2005

Abstract—When an external action exceeds a certain critical level, the state of a structurally unstable crystal with a condensate of autosolitons becomes unstable with respect to the appearance of localized spiral autowaves (vortices). © *2005 Pleiades Publishing, Inc.*

Introduction. The formation of ordered structures in dynamical systems far from equilibrium is among the most interesting physical phenomena. Such structures arise in dynamical systems of substantially different types, such as the thoroughly studied dissipative structures [1, 2], Benard structures in turbulent flows, autowave processes in chemical and biological systems featuring the Belousov–Zhabotinsky reaction, and coherent optical generation in lasers. Less studied phenomena include the coherent states of atoms in a crystal lattice and the generation of elementary collective excitations (autosolitons) in a crystal exhibiting martensite transformations [3], which are accompanied by the appearance of a condensate of autosolitons and the formation of modulated crystal structure (inhomogeneous inelastic microdeformation) of the structurally unstable crystal [4].

Recently, a collective strain mode has been revealed in structurally unstable crystals [5], which leads to reorientation of the crystal lattice via the $\gamma \longrightarrow \alpha \longrightarrow \gamma$ phase transition involving volume deformation of the Bain type. In this case, the high-angle boundaries are formed as a result of the Bain type deformation and, hence, the crystal lattice reorientation according this mechanism (in contrast to the well-known dislocation–disclination mechanisms of reorientation [6]) is not accompanied by real rotation of the crystal lattice in the transition zone. Possessing a purely volume character, the $\gamma \longrightarrow \alpha \longrightarrow \gamma$ phase transition via the Bain type deformation does not involve the formation of stress moments. Spontaneous torque in the region of a ferroelastic structural transition has also been observed in $SrTiO_3$ [7]. Digal *et al.* [8] has developed a model of structural transitions based on the Lagrange theory, in which vortices play the role of topological defects of the system.

The results presented in this Letter show that, when an external action exceeds a certain critical level, the state of a structurally unstable crystal with the Bose condensate of autosolitons becomes unstable with respect to the appearance of localized spiral autowaves analogous to the Abrikosov vortex lines in superconductors.

Equation of the autosoliton condensate evolution. The inhomogeneous complex order parameter $\Psi = \rho\exp(-i\Phi)$, whose square amplitude is equal to the density of the Bose condensate of autosolitons and the phase gradient is proportional to the wave vector of a modulated crystal structure, is described by the evolution equation [3, 4]

$$\dot{\Psi}(\mathbf{r}, t) = \lambda(\rho)\Psi(\mathbf{r}, t) - i\omega(\rho)\Psi(\mathbf{r}, t) + (D_1 + iD_2)\nabla^2\Psi(\mathbf{r}, t), \quad (1)$$

where the upper dot denotes differentiation with respect to time, $\lambda(\rho) = \alpha_1 - \beta_1\rho^2$, $\omega(\rho) = \alpha_2 - \beta_2\rho^2$, $D = D_1 + iD_2$ is the effective complex diffusion coefficient, and ∇ is the nabla operator. The coefficients $\alpha_1 = \gamma_\psi(0) + |V|^2\sigma^*\gamma_d^{-1}$, $\alpha_2 = \Omega(0) + |V|^2\sigma^*\gamma_d^{-2}[\Omega(0) - E]$, $\beta_1 = -|V|^2\sigma^*\gamma_d^{-1}\Psi_1^{-2}$, $\beta_2 = -|V|^2\sigma^*\gamma_d^{-2}\Psi_1^{-2}[\Omega(0) - E]$, $D_1 = (\partial\gamma_\psi/\partial q^2)_{q=0}$, $D_2 = (\partial\Omega/\partial q^2)_{q=0}$ and $\Psi_1^{-2} = 4|V|^2\gamma_d^{-1}\gamma_\sigma^{-1}$ have been calculated in [3]. As can be seen from Eq. (1), the function $\lambda(\rho)$ becomes zero at $\rho = \rho_0 = (\alpha_1/\beta_1)^{1/2}$, is negative for $\rho > \rho_0$, and is positive for $\rho < \rho_0$. Thus, the Bose condensate of autosolitons is an autooscillatory medium described by the λ–ω model [9].

Substituting the complex order parameter expressed as $\Psi(\mathbf{r}, t) = \rho(\mathbf{r}, t)\exp[-i(\omega_0 t + \varphi(\mathbf{r}, t))]$ into Eq. (1), we

obtain the following system of equations for the functions $\rho(\mathbf{r}, t)$ and $\varphi(\mathbf{r}, t)$:

$$\dot{\rho} = \lambda(\rho)\rho + D_1\nabla^2\rho - D_1\rho(\nabla\varphi)^2 + D_2\rho\nabla^2\varphi + 2D_2(\nabla\rho)(\nabla\varphi), \quad (2)$$

$$\dot{\varphi} = [\omega(\rho) - \omega_0] + 2D_1\rho^{-1}(\nabla\rho)(\nabla\varphi) - D_2\rho^{-1}\nabla^2\rho + D_2(\nabla\varphi)^2 + D_1\nabla^2\varphi. \quad (3)$$

In the case of smooth phase distributions with large characteristic lengths L, the amplitude deviations $\delta\rho(\mathbf{r}, t)$ will adiabatically adjust to the values of $\nabla\varphi$ and $\nabla^2\varphi$ at the corresponding points of the condensate. To within terms on the order of $1/L^2$, we have $\delta\rho = \rho_0\tau_{rel}[D_2\nabla^2\varphi - D_1(\nabla\varphi)^2]$, where t_{rel} is the amplitude relaxation time. Substituting $\rho = \rho_0 + \delta\rho$ into Eq. (3), and retaining only terms on the order of $1/L^2$, we obtain the relation

$$\dot{\varphi} = \alpha(\nabla\varphi)^2 + b\nabla^2\varphi, \quad (4)$$

where $a = -(\beta_2/\beta_1)D_1 + D_2$ and $b = (\beta_2/\beta_1)D_2 + D_1$ are coefficients with dimensionality of the diffusion coefficient. As can be seen from Eq. (4), the phase relaxation time τ_L is on the order of L^2/b. Obviously, the obtained relation is only applicable to the description of smooth phase distributions with large characteristic inhomogeneity lengths $L \gg (b\tau_{rel})^{1/2}$. This condition restricts the domain of applicability of the equation of phase dynamics (4).

Waves with a small spatial period, for which $k \geq (b\tau_{rel})^{-1/2}$, usually lose stability in the region of wavenumbers $k \approx (b\tau_{rel})^{-1/2}$ and no longer obey the equation of phase dynamics (4). Therefore, we may expect that stable inhomogeneous distributions of autosolitons with the characteristic scales $l_{dif} \leq 1/k \approx (b\tau_{rel})^{1/2}$ can exist in a structurally unstable crystal and, in particular, have the form of spirals (vortices) rotating at a constant angular velocity. These vortices are the analogs of stationary solitary autowaves spontaneously formed in autooscillatory media [1, 2]. Since both the vortex core size and the diffusion length $l_{dif} \approx (b\tau_{rel})^{1/2}$ are always small and have the same order of magnitude, these inhomogeneities in the Bose condensates of autosolitons have to be described using the complete equations in partial derivatives (2) and (3).

Stationary solutions of the evolution equation. As will be demonstrated below, a spiral wave is the internal driving force of reorientation in local regions of the lattice of a structurally unstable crystal and the internal source of phase waves. Let us restrict the consideration to the case of $D_2 = 0$, whereby the imaginary additive in the effective diffusion coefficient vanishes ($D = D_1$). The condensate performs homogeneous autooscillations with the amplitude ρ_0, determined from the condition $\lambda(\rho_0) = 0$, and the frequency $\omega_0 = \omega(\rho_0)$. The diffusion length in this approximation is $L_{dif} = (b/\tau_{rel})^{1/2} = (D/|\rho_0\lambda'(\rho_0)|)^{1/2}$. In a polar coordinate system (r, Θ), a spiral wave rotating at an angular velocity of ω can be described as

$$\rho = \rho(r), \quad \varphi = \Theta - \chi(r) - (\omega_* - \omega_0)t. \quad (5)$$

Substituting relations (5) into Eqs. (2) and (3), we obtain the following system of equations:

$$\rho_{rr} + r^{-1}\rho_r + (D^{-1}\lambda(\rho) + r^{-2} - \chi_r^2)\rho = 0, \quad (6)$$

$$\chi_{rr} + r^{-1}\chi_r + 2(\rho_r/\rho)\chi_r = (\omega_* - \omega(\rho))/D. \quad (7)$$

Assuming that the functions $\rho(r)$ and $\chi_r(r)$ must be finite at $r = 0$, we infer that $\rho(r) \approx r$ for $r \longrightarrow 0$ and $\chi_r(0) = 0$. By the same token, the wave amplitude $\rho(r)$ must tend to a certain nonzero value ($\rho \longrightarrow \rho_*$) for $r \longrightarrow \infty$. Then, Eqs. (5)–(7) yield $\omega_* = \omega(\rho_*)$ and $\chi_r(r) \longrightarrow \pm k_*$ for $r \longrightarrow \infty$, where $k_* = [\lambda(\rho_*)]^{1/2}$. Thus, the spiral wave has a constant pitch $H_{ar} = 2\pi/|\chi_r| = 2\pi/k_*$ at large distances from the center (i.e., it is an Archimedean spiral) [1, 2]. The spiral pitch is equal to the spatial period of a plane phase wave with the frequency ω_*. The two signs at $\chi_r(\infty)$ correspond to the two possible spiral twist directions.

Since the differential equations (6) and (7) do not admit completely analytical solution, let us use approximate methods for evaluating the spiral wave rotation frequency ω_* and determining the functions $\rho(r)$ and $\chi(r)$. In the particular case of $\omega(\rho) = \omega_0 = \text{const}$ (whereby a nonlinear frequency shift is absent), the spiral wave frequency must also coincide with ω_0. Then, Eq. (7) shows that $\chi_r(r) = 0$ if $\chi_r(0) = 0$ and, according to relations (5), the spiral degenerates into a straight ray rotating at a constant angular velocity of ω_0. This implies that autosolitons in the condensate are redistributed so as to provide for a local reorientation of the crystal lattice.

In the case under consideration, the amplitude $\rho(r)$ obeys the equation

$$\rho_{rr} + r^{-1}\rho_r - \rho/r^2 + \rho\lambda(\rho)/D = 0, \quad (8)$$

which has to be supplemented by the boundary conditions $\rho(0) = 0$ and $\rho(r) \longrightarrow \text{const}$ for $r \longrightarrow \infty$. As can be seen from Eq. (8), the density $\rho^2(r)$ of the condensate at the periphery of the spiral coincides with the density ρ_0^2 of a homogeneous condensate. On approaching the center of the spiral wave, the density exhibits a monotonic decrease and vanishes at $r = 0$. Thus, the conden-

sate of autosolitons features a vortex (exhibits rotation) with a low density of autosolitons in the central part.

Now let us consider the case of a very weak dependence of the rotation frequency ω on the amplitude $\rho(r)$: $\omega(\rho) = \tilde{\omega} = \varepsilon\delta\omega(\rho)$, $0 < \varepsilon \ll 1$ (nonlinear frequency shift). The solution for a spiral wave in the condensate can be found using the method of matched asymptotic expansions [1, 2]. According to this, we introduce a small parameter defined as $q = w'(\rho_0)/|\lambda'(\rho_0)| = \varepsilon\delta\omega'(\rho_0)|\lambda'(\rho_0)|$ ($q \ll 1$) and construct approximate solutions to Eqs. (6) and (7) in the inner ($r \ll \lambda_{dif}\exp(1/|q|)$) and outer ($r \gg l_{dif}$) regions. Since $q \ll 1$, the two regions overlap. Upon matching the approximate solutions in the region of overlap, we determine the frequency $\omega_* = \omega_0 - qDk_*^2$ of the spiral wave rotation and the corresponding wavenumber $k_* = 0.509(|q|L_{dif})^{-1}\exp[-\pi/2|q|]$.

Expanding the wave amplitude in powers of q in the inner region, we obtain

$$\rho(r) = P_0(r) + q^2P_1(r) + \ldots,$$
$$\chi_r(r) = |q|\nu_0(r) + |q|^3\nu_1(r) + \ldots,$$

where

$$\nu_0(r) = -(\lambda'(\rho_0)/\delta\omega'(\rho_0))[rP_0^2(r)]^{-1}\int_0^r yP_0^2(y)[\delta\omega(\rho_0) - \delta\omega(P_0(y))]dy.$$

In the interval $l_{dif} \ll r \ll l_{dif}\exp(1/|q|)$, we have $\nu_0(r) = (l_{dif}/r)[\ln(r/l_{dif}) + C_1]$.

The outer region can be considered as including the near ($l_{dif} \ll r \ll 1/k_*$) and the far ($r \gg 1/k_*$) zones. Then, Eqs. (5)–(7) give

$$\chi_r(r) \approx (l_{dif}/r)\tan\{|q|[\ln(r/l_{dif}) + C_1]\} \quad (9)$$

for the near zone and

$$\chi_r(r) \approx -k_*K_0'(|q|kr)/K_0(|q|kr) \quad (10)$$

for the far zone, where $K_0(x)$ is the modified Bessel function with the asymptotic behavior $K_0(x) \longrightarrow 0$ as $x \longrightarrow \infty$. For $qkr \ll 1$, we can expand $\chi_r(r)$ as

$$\chi_r(r) \approx k_*[1 + (1/2)(q|kr|)^{-1} - (1/8)(qkr)^{-2} + \ldots]. \quad (11)$$

Since the amplitude $\rho(r)$ and the function $\chi_r(r)$ in the outer region are related as

$$\rho(r) = \rho_0 - (r^{-2} + \chi_r^2)l_{dif}^2, \quad (12)$$

the amplitude of oscillations tends to the limit $\rho_* = \rho_0 - (l_{dif}k_*)^2$ as $r \longrightarrow \infty$. Relations (11) and (12) show that

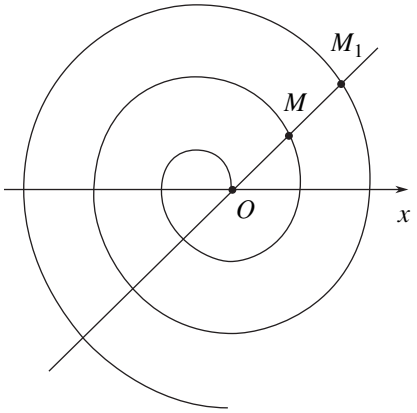

A spiral autowave (vortex) in a structurally unstable crystal.

the spiral wave formed in the condensate of autosolitons accounts for the reorientation of the crystal lattice and serves as the internal source of phase waves.

Discussion. When an external action reaches a critical level, a condensate of elementary defects (autosolitons) appears in a structurally unstable crystal, which represents an autooscillatory medium featuring the propagation of phase waves. The excitation and propagation of such a phase wave in the condensate is a mechanism that provides, on the one hand, an inhomogeneous distribution of the elementary defects and, on the other hand, the formation of a modulated crystal structure [3, 4]. As the external action grows further, the condensate of elementary defects becomes unstable with respect to the development a localized spiral autowaves (vortices). At a relatively large distance from the vortex center, the lines of constant phase have the shape of an Archimedean spiral with a constant pitch (see figure). The frequency of rotation of the spiral wave is a single-valued function of the condensate characteristics and does not depend on the initial conditions, which leads to the appearance of the autowave source. On approaching the center of the spiral wave, the density of elementary defects in the condensate monotonically decreases and vanishes at the center. For this reason, we may consider the core of a spiral wave in a structurally unstable crystal as a region where the density of elementary defects in the condensate significantly differs from that of a homogeneous condensate. The size of the vortex core in the condensate is always small, being on the order of the diffusion length l_{dif}. Each vortex line is characterized by a certain value of the phase gradient circulation over a closed contour containing this line. Since the phase of the wave function of the autosoliton coincides with the phase of the Fourier component of solitary configurational excitations (displacements) of the crystal lattice [3, 4], the formation of a vortex in the condensate of autosolitons leads to reorientation of the corresponding local region of the crystal. Such a spontaneously formed spiral wave is the internal driving force of reorientation in local regions of the lattice of

a structurally unstable crystal and the internal source of phase waves (inhomogeneous inelastic vortex microdeformation), which is indirectly confirmed by the results of experiments on a macroscopic deformation level [5, 7].

REFERENCES

1. V. G. Yakhno, *Autowave Processes in Systems with Diffusion* (IFP AN SSSR, Gorkii, 1981) [in Russian].
2. A. Yu. Loskutov and A. S. Mikhailov, *Foundations of Synergetics* (Nauka, Moscow, 1990; Springer-Verlag, Berlin, 1990).
3. E. E. Slyadnikov, Izv. Vyssh. Uchebn. Zaved., Fiz., No. 7, 69 (2004).
4. E. E. Slyadnikov, Pis'ma Zh. Tekh. Fiz. **30** (24), 82 (2004) [Tech. Phys. Lett. **30**, 1057 (2004)].
5. A. N. Tyumentsev, I. Yu. Litovchenko, Yu. P. Pinzhin, *et al.*, Fiz. Met. Metalloved. **95** (2), 86 (2003).
6. V. I. Vladimirov and A. E. Romanov, *Disclinations in Crystals* (Nauka, Leningrad, 1986) [in Russian].
7. V. V. Lemanov, S. A. Gridnev, and E. V. Ukhin, Fiz. Tverd. Tela (St. Petersburg) **44**, 1106 (2002) [Phys. Solid State **44**, 1156 (2002)].
8. S. Digal, R. Ray, T. Segupta, and A. M. Srivastava, Phys. Rev. Lett. **84**, 826 (2000).
9. Y. Kuramoto, Prog. Theor. Phys. **63**, 1885 (1980).

Translated by P. Pozdeev

Technical Physics Letters, Vol. 31, No. 12, 2005, pp. 1015–1018. Translated from Pis'ma v Zhurnal Tekhnicheskoĭ Fiziki, Vol. 31, No. 23, 2005, pp. 46–54.

A Mechanism of Grain Nucleation during Relaxation of the Latent Energy of Junction Disclinations in the Course of Plastic Deformation

T. S. Orlova[a], A. E. Romanov[a,*], A. A. Nazarov[b,], N. A. Enikeev[b], I. V. Alexandrov[b], and R. Z. Valiev[b]**

[a] *Ioffe Physicotechnical Institute, Russian Academy of Sciences, St. Petersburg, 194021 Russia*
[b] *Ufa State Aviation Technical University, Ufa, Bashkortostan, 450000 Russia*
*e-mail: * aer@mail.ioffe.ru; ** AANazarov@mail.rb.ru*
Received July 25, 2005

Abstract—A model describing the nucleation of a new grain at the boundary of an existing grain during relaxation of the latent energy of junction disclinations formed in the course of plastic deformation is considered. This nucleation mechanism is shown to be energetically favorable. The dependence of the equilibrium size and misorientation of a nucleus on its shape is analyzed. © *2005 Pleiades Publishing, Inc.*

It has been reliably established that large and intense plastic deformation gives rise to the fragmentation of grains in polycrystalline solids [1] and leads to the formation of submicro- and nanocrystalline structures [2]. In particular, a promising way to grain refinement is offered by the method of equichannel angular pressing (ECAP) [3]. By means of ECAP technology, materials with an average grain size as small as 100 nm can be obtained while retaining the initial shape of the articles [2, 4]. The development of methods for obtaining solids with nanocrystalline structures is an important practical task, since such nanostructured materials exhibit modified, frequently improved mechanical properties [2, 4, 5].

This Letter presents a disclination model describing the nucleation of new grains in the course of intense plastic deformation of a polycrystalline solid. The proposed model shows that the appearance of new grains of smaller size in the initial polycrystalline material subjected to inhomogeneous plastic straining is energetically favorable.

In the course of inhomogeneous plastic straining, grains are deformed to different extents, which leads to the accumulation of structural defects (dislocations) at the grain boundaries. These dislocations account for the continuity of material (i.e., for the consistent deformation of grains) and appear as powerful sources of internal mechanical stresses and the latent energy of plastic straining. It was originally shown by Rybin *et al.* [6, 7] that gliding dislocations captured at the grain boundaries form a network of equivalent disclination defects situated at the triple junctions of grains. As a result, the elastic (latent) energy stored in the material can be associated with mesodefects having the form of junction disclinations. In the course of subsequent relaxation processes, this latent energy decreases, thus providing the possibility of structural transformations of a given polycrystalline material [1]. From the standpoint of nanocrystalline structure formation, the most important mechanism is related to the redistribution of shear stresses in grains, which results in the appearance of new misorientation boundaries. In recent years, these notions served as a basis for analysis of the energetic conditions necessary for grain refinement leading eventually to the formation of a nanocrystalline structure [8, 9].

Let us consider an initial grain of rectangular cross section $2a \times 2b$ (for simplicity, we will analyze a two-dimensional problem in the geometry schematically depicted in Fig. 1). Under the conditions of inhomogeneous plastic straining, wedge (difference) disclinations arise at the junctions of the grain, which have generally different strengths ω, $-g\omega$, $k\omega$, and $-q\omega$. Below, we assume that ω is the maximum disclination strength, so that $0 \le (g, q, k) \le 1$. The nucleation and growth of a new grain proceed via the appearance of a misorientation band at the sites of possible stress concentrators on the grain boundaries, followed by the propagation of this band inside the initial grain. Consider the nucleus of such a new grain, also of rectangular shape with dimensions $2l \times 2d$. This nucleus can be described, by analogy with the initial grain, as a new disclination quadrupole with $2l$ and $2d$ arms and a strength of $\pm\omega_x$.

The possibility of grain refinement via such nucleation can be judged from the energy gain achieved due to the formation of a new disclination configuration, which can be evaluated by comparing the system energies before and after splitting of the initial grain. Should the process lead to a decrease in the energy of

1063-7850/05/3112-1015$26.00

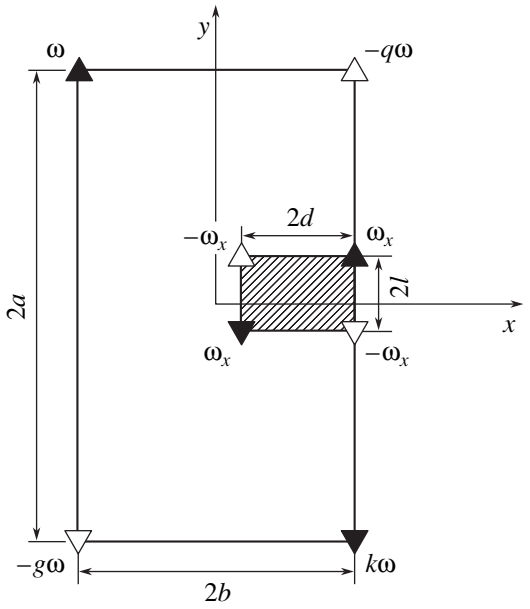

Fig. 1. A diagram illustrating the nucleation of a new grain at one of the initial grain boundaries (*g*, *q*, and *k* are the parameters characterizing the asymmetry of the disclination quadrupole configuration in the initial grain).

the initial grain (or a group of grains), it can be realized in the course of plastic straining of a polycrystalline solid.

The energy difference ΔE for the grain before and after the formation of a nucleus includes the following contributions: (i) the energy of a new disclination quadrupole; (ii) the energy of the interaction of this quadrupole with disclinations at the junctions of the initial grain subject to splitting; and (iii) the total interfacial energy of the new misorientation boundaries. For the system under consideration, the components (i)–(iii) of the energy difference ΔE have been determined as described in [9]. We assume that the nucleation of a new grain can take place provided that at least one disclination at the initial grain junctions reaches a critical strength of $\Omega_c = 1°$. This choice of the criterion of disclination stress relaxation agrees with the theoretical estimates and experimental results obtained previously [1, 10]. Since, according to the model adopted, ω is the maximum disclination strength in the quadrupole configuration, the new grain nucleation takes place for $\omega = 1°$.

Figure 2 shows a plot of the grain energy difference before and after nucleation versus the size l of the nucleus for various relative misorientations $p = \omega_x/\omega$. As can be seen, the formation of a new grain is energetically favorable. The energy minimum can be achieved simultaneously with respect to two parameters (l and p), whereby the nucleus has an equilibrium size l_{eq} and an equilibrium strength p_{eq}.

Let us introduce a parameter characterizing the total symmetry of the initial disclination quadrupole, which is defined as $\lambda = 1 + g + q + k$ (Fig. 1). An analysis of the ΔE value as a function of this parameter shows that, as λ (i.e., the degree of symmetry of the initial quadrupole) grows, the energy gain due to the appearance of a nucleus (i.e., grain fragmentation) increases. This implies that the fragmentation will proceed more readily in grains with smaller differences of strengths of the junction disclinations. Both the energy gain and the size of the equilibrium nucleus depend not only on λ, but also on the ratio of strengths g, q, and k of the separate disclinations at the vertices of the initial grain.

An analysis of the ΔE value as a function of p and l shows that, when the misorientation band appears at the longer side a of the grain (in the case of $a \geq b$), a nucleus can form that has simultaneously the equilibrium values of two parameters: the size l_{eq} and the misorientation p_{eq} relative to the initial grain (for $a < b$, the equilibrium values of these parameters cannot be simultaneously reached within the framework of the adopted model).

Let us consider the influence of the shape of the nucleus on the equilibrium values of misorientation (p_{eq}), the size of the nucleus (l_{eq}), and the corresponding energy gain (ΔE_{min}) for an initial grain with $a \geq b$. Figure 3 shows the dependences of these values on the shape of nucleus, that is, on the length-to-width ratio d/l (aspect ratio) for the initial equiaxial grain with $a = b = 1$ μm. It should be noted that a nucleus equilibrium with respect to two parameters (p and l) simultaneously can form only in the case of $d/l \geq 1$ (for $d/l < 1$, this situation is impossible within the framework of the adopted model). As can be seen from Fig. 3, the energy gain due to the formation of a new grain is maximum when its shape is similar to that of the initial grain, that is, for $d/l \approx b/a = 1$. This property is valid for any values of a and b satisfying the condition $b \leq a$.

It is of interest to compare the energy gain in the two cases, whereby the nucleation takes place at the long ($a \geq b$) or at the short ($a < b$) boundary of the initial grain. Calculations show that the difference in the energy gain for these cases is rather insignificant. An analysis of the ΔE value as a function of the initial grain size shows that, for the model adopted, the fragmentation of grains by this mechanism is possible for the initial grain of any size. However, the energy gain decreases with increasing fragmentation of the initial structure, since this is accompanied by an increase in the role of the energy of newly formed boundaries. It should be noted that the proposed model was formulated with neglect of the contribution of the work of external stresses to the energy balance upon nucleation. During the subsequent growth of the nucleus and the corresponding development of strain-induced boundaries, the contribution of applied stresses can be taken into account. This can be done, for example, within the

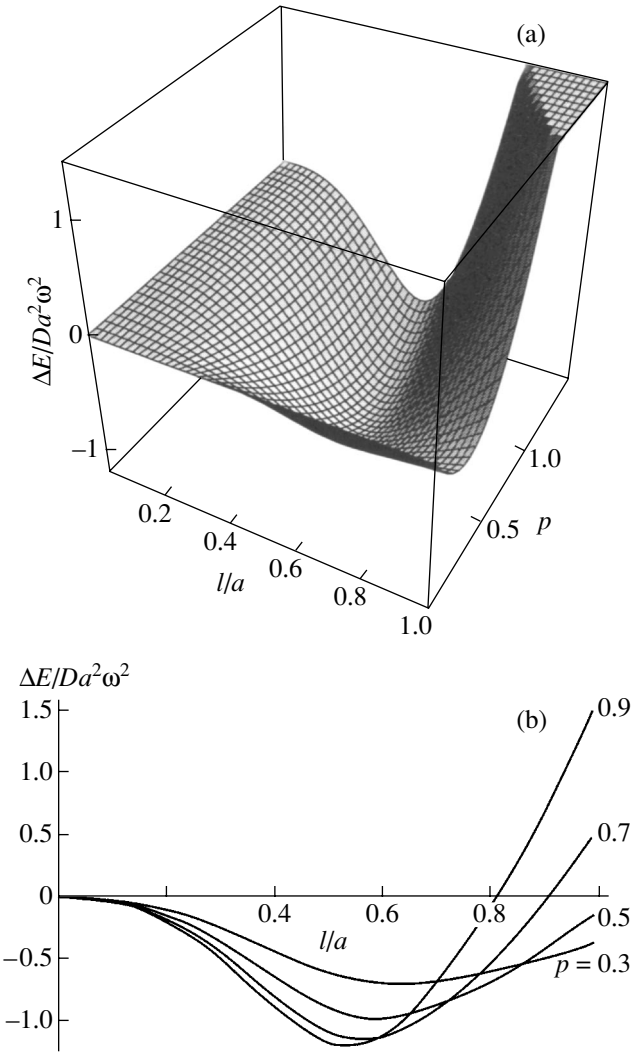

Fig. 2. A change in the energy of the initial grain as a result of the formation of a new grain at one of the initial grain boundaries ($D = G/[2\pi(1 - \nu)]$), G is the shear modulus, ν is the Poisson ratio for a model system with the parameters $b = a = 1$ μm, $d/l = 2$, $q = 0.1$, $g = k = 1$: (a) the general dependence of the energy gain ΔE on the relative size l/a and misorientation $p = \omega_x/\omega$ of the nucleus; (b) the partial dependences of ΔE on l/a for various values of $p = \omega_x/\omega$.

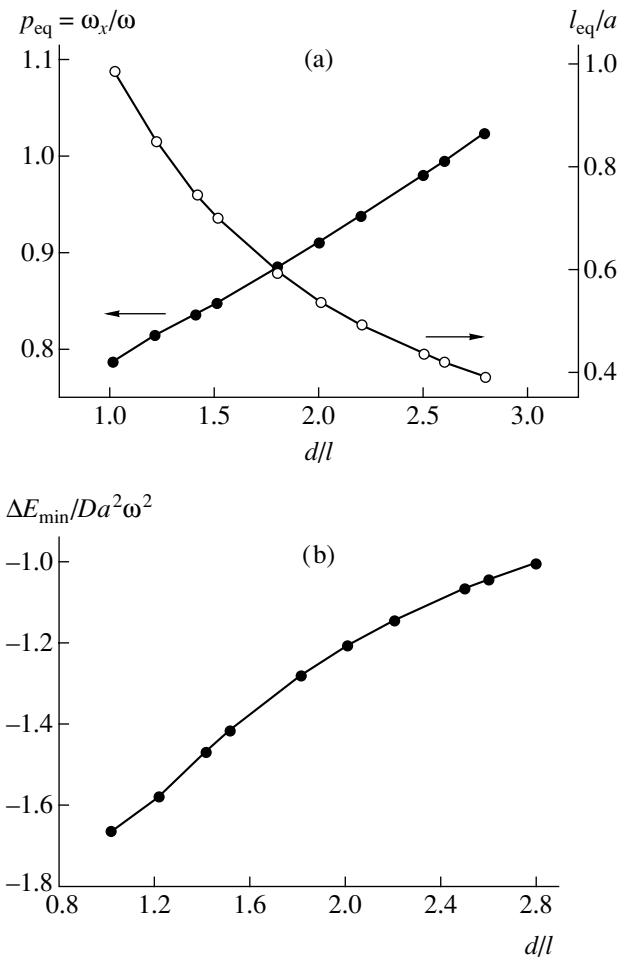

Fig. 3. Dependences of the (a) equilibrium relative size l_{eq}/a and equilibrium misorientation p_{eq} of a new grain and (b) energy gain ΔE_{min} due to the formation of a nucleus with equilibrium size and misorientation on the shape (aspect ratio d/l) of the nucleus for $b = a = 1$ μm, $g = k = 1$, $q = 0.1$.

framework of the model of development of reorientation bands [11].

In conclusion, we have proposed a model describing the formation of the nucleus of a new grain at one of the boundaries of an existing grain as a result of relaxation of the stored energy of plastic straining. It was demonstrated that the nucleation of a new grain inside the initial one is energetically favorable irrespective of the initial grain size, although the energy gain decreases with increasing fragmentation of the polycrystalline structure. The energy gain depends on the initial configuration of disclinations formed at the junctions of the initial grain in the course of plastic straining. It was found that the energy gain is maximum in the case of a symmetric initial disclination quadruple configuration. The formation of a nucleus possessing both equilibrium size and equilibrium misorientation is possible only at the long boundary of the initial grain (i.e., for $a \geq b$). In this case, the energy gain due to the new grain formation is maximum when its shape is similar to that of the initial grain, that is, for $d/l \approx b/a$.

REFERENCES

1. V. V. Rybin, *Heavy Plastic Deformation and Fracture of Metals* (Metallurgiya, Moscow, 1986) [in Russian].
2. R. Z. Valiev and I. V. Alexandrov, *Nanostructural Materials Obtained by Heavy Plastic Straining* (Logos, Moscow, 2000), p. 272 [in Russian].

3. V. M. Segal, V. I. Reznikov, V. I. Kopylov, and D. A. Pavlik, *Processes of Plastic Structuration in Metals* (Navuka i Tekhnika, Minsk, 1994) [in Russian].
4. R. Z. Valiev, Metally, No. 1, 15 (2004).
5. R. Z. Valiev, R. K. Islamgaliev, and I. V. Alexandrov, Prog. Mater. Sci. **45**, 103 (2000).
6. V. V. Rybin, A. A. Zisman, and N. Yu. Zolotarevsky, Fiz. Tverd. Tela (Leningrad) **27**, 181 (1985) [Sov. Phys. Solid State **27**, 105 (1985)].
7. V. V. Rybin, A. A. Zisman, and N. Yu. Zolotarevsky, Acta Metall. Mater. **41**, 2211 (1993).
8. A. E. Romanov, T. S. Orlova, N. A. Enikeev, *et al.*, in *Ultrafine Grained Materials III*, Ed. by Y. T. Zhu, T. G. Langdon, R. Z. Valiev, *et al.* (The Minerals, Metals & Materials Society, Warrendale, 2004), pp. 211–216.
9. T. S. Orlova, A. A. Nazarov, N. A. Enikeev, *et al.*, Fiz. Tverd. Tela (St. Petersburg) **47**, 820 (2005) [Phys. Solid State **47**, 845 (2005)].
10. V. V. Rybin, Vopr. Materialoved. **29**, 11 (2002).
11. M. Yu. Gutkin, K. N. Mikaelyan, A. E. Romanov, and P. Klimanek, Phys. Status Solidi A **193**, 35 (2002).

Translated by P. Pozdeev

Technical Physics Letters, Vol. 31, No. 12, 2005, pp. 1019–1021. Translated from Pis'ma v Zhurnal Tekhnicheskoĭ Fiziki, Vol. 31, No. 23, 2005, pp. 55–60.

Optical Transmission of Hollow Glass Photonic-Crystal Fibers

V. I. Beloglazov[a], Yu. S. Skibina[b,*], V. V. Tuchin[b], and M. V. Chaĭnikov[a]

[a] *Nanostructural Glass Technology, Research and Production Corporation, Saratov, Russia*

[b] *Institute of Optics and Biophotonics, Saratov State University, Saratov, Russia*

* *e-mail: julia@mail.saratov.ru*

Received July 6, 2005

Abstract—A photonic-crystal fiber (PCF) with a forbidden photon band (FPB) in the visible spectral range has been created for the first time. The PCF shell comprises concentric layers of hollow circular air-filled channels with variable diameters. The optical transmission of the proposed PCF and the influence of the geometric parameters on the FPB width and position in the visible spectral range have been studied. By varying the PCF structure and geometry, it is possible to change the FPB characteristics, which offers broad possibilities of output light control. © *2005 Pleiades Publishing, Inc.*

There are photonic-crystal fibers (PCFs) of two main types [1–3]. Fibers of the first type comprise a high-index glass core and a surrounding two-dimensional (2D) photonic crystal shell with a relatively low effective refractive index. In such PCFs, the light is guided via the core by means of total internal reflection (TIR). In fibers of the second type, the hollow (air-filled) central channel has a relatively low index compared to that of the surrounding 2D photonic crystal shell and, hence, TIR does not take place. In this case, a certain optical mode is guided via the hollow channel due to the localizing and guiding properties of forbidden photon bands (FPBs) formed in the photonic crystal.

The PCFs were manufactured using the classical optical fiber technology [4]. The cross section of the proposed PCF structure is depicted in the inset to Fig. 1. This PCF has a central hollow channel with a diameter of 518 μm (in other samples, this channel had a diameter of 61.3, 64.4, 71.5, 80.5, 90, or 107 μm) and a shell consisting of concentric layers of hollow circular air-filled channels (capillaries) with increasing diameters. The optical transmission of the PCF was studied in the visible and near-IR (NIR) spectral regions using an automated spectroscopic complex based on a DMR-4 monochromator.

Figure 1 shows the typical transmission spectrum of the PCF with a 518-μm central channel and 14-μm channels in the first concentric layer of the photonic crystal shell (same as depicted in the inset). This PCF is essentially a blank from which the fibers with smaller diameters of the central and peripheral channel are made. As can be seen, the transmission spectrum of the hollow PCF is characterized by the presence of sharp maxima. These peaks appear due to the high reflectance of a periodically structured 2D photonic crystal shell at wavelengths corresponding to the FPBs [5].

The spectral properties of hollow PCFs were studied as dependent on the geometry of the structured shell and the hollow central channel. It was experimentally demonstrated that the optical transmission spectrum can be modified by changing the PCF shell structure and geometry. In particular, the effect of the central channel diameter can be detected by naked eye: in the presence of a forbidden photon band in the red spectral range, the central channel transmits only the violet-blue

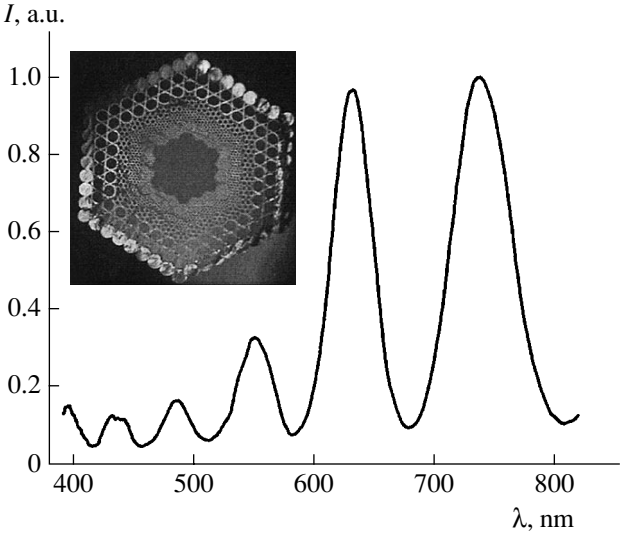

Fig. 1. The typical transmission spectrum of a PCF with a 518-μm central channel and 14-μm channels in the first concentric layer of the photonic crystal shell. The inset shows the cross section of this PCF.

1063-7850/05/3112-1019$26.00 © 2005 Pleiades Publishing, Inc.

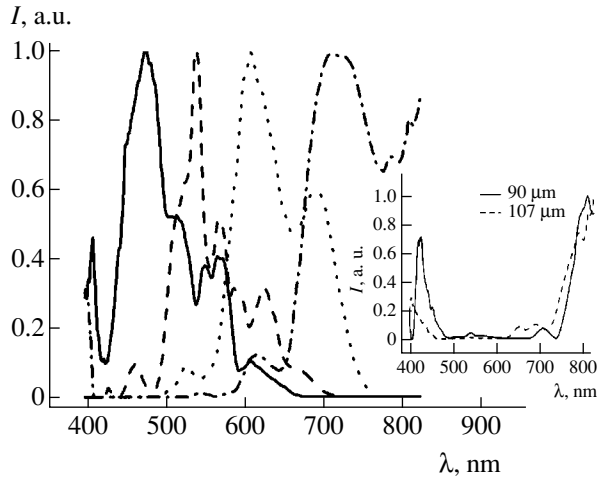

Fig. 2. The optical transmission spectra of microstructural PCFs with various diameters of the central hollow channel and the capillaries of concentric shells (see the text for the values of PCF parameters).

component and acquires the corresponding color. Thus, it is possible to determine visually, with high precision, the spectral regions corresponding to the maximum transmission and the FPBs.

Figure 2 shows the evolution of the transmission spectrum of PCFs with a constant length of 950 mm and various diameters of the hollow central channel and the capillaries. The solid curve represents the spectrum of the PCF with a central channel diameter of D = 61.3 μm, the diameter of capillaries in the first concentric layer of the photonic crystal shell d = 1.33 μm, a numerical aperture of NA = 0.105, and an output beam divergence of $\delta = 12.1°$. In this case, the maximum transmission is observed in the blue region at λ = 467 nm, while the FPB extends over the red and NIR range above 658 nm. The dashed curve in Fig. 2 represents the spectrum of the PCF with D = 64.4 μm, d = 1.4 μm, NA = 0.122, and $\delta = 14.1°$, in which the transmission peak occurs in the green region at λ = 531 nm, while the FPB occurs in the red and NIR region above 700 nm. The next spectrum (depicted by the dotted curve in Fig. 2) corresponds to the structure with D = 71.5 μm, d = 1.55 μm, NA = 0.124, and $\delta = 14.2°$. Here, the transmission peak occurs in the red region at λ = 604 nm and the transmission is completely absent in the spectral regions within 400–492 nm (violet, dark blue and, partly, bright blue regions) and above 763 nm (NIR range). Finally, the dash–dot curve in Fig. 2 refers to the structure with D = 80.5 μm, d = 1.75 μm, NA = 0.073, and $\delta = 8.4°$, for which the transmission peak occurs in the NIR region at λ = 715 nm and the FPB occupies the spectral range from 402 to 572 nm with a width of about 170 nm. The inset to Fig. 2 shows the transmission spectra of the PCFs with D = 90 and 107 μm, d = 2 and 2.33 μm, NA = 0.079 and 0.083, and $\delta = 9.1°$ and 9.5°, for which the FPB widths amount to 190 nm (480–670 nm) and 167 nm (450–617 nm) (solid and dashed curves, respectively). Note that the FPB for these samples falls entirely into the visible spectral range.

The experimental data presented above indicate that the FPB parameters can be controlled within the visible spectral range by changing the geometry of the structured photonic crystal shell consisting of air-filled channels with the diameters increasing according to a certain law. By increasing the diameter of the hollow central channel, it is possible to shift the peak of maximum transmission toward the NIR spectral range. Using small changes in the PCF geometry, the FPB position can be adjusted to within several nanometers so as to obtain "spectrally pure" radiation. This possibility of the output light control makes PCFs of the proposed type promising spectral elements with a preset attenuation and/or transmission band. It should be emphasized that the character of light propagation in such PCF structures is substantially different from that in the standard optical fibers.

The results of our experiments showed that light propagates in the PCFs under consideration along the capillary walls, which form the surface of the hollow central channel. This is confirmed by a small numerical aperture of the fibers and by low optical losses. The fact of the near-wall light propagation in PCFs indicates that the role of the fiber material is not very large and that the main factor is the PCF shell structure, including the step, diameter, and distribution of channels (i.e., the refractive index gradient) and the size and geometry of the defect. In PCFs with a capillary wall thickness comparable with the depth of light penetration into this material, the optical losses will tend to zero. The shorter the wavelength, the more critical is the state of the channel surface. In the presence of an index gradient, the light is guided within a very thin layer (with the thickness not exceeding 10 nm) in the capillary walls (for the given PCF design and geometry, this factor is competitive with the diffraction effects). Subsequent investigations have to reveal physical factors determining the limiting efficiency of nonlinear optical processes. Based on such data, it will be possible to establish the optimal architecture of the nanodimensional structure controlling the conditions of light propagation in PCFs.

The proposed PCFs can provide a high efficiency of many nonlinear optical processes, which can be used immediately in various fields, for example, in biomedical applications for the creation of high-efficiency light sources used in coherent optical tomography and high-precision sensors. The introduction of liquids or cells (water, alcohol, glucose, hemoglobin, erythrocytes, etc.) into the hollow central channel must provide for effective control over the PCF transmission spectrum, whereby the transmission band is shifted over the visible spectral range. The further research in this field will also provide high-sensitivity lab-on-chip sensors capa-

ble of determining extremely small variations in the concentrations and/or refractive indices of biological media, which is necessary for medical diagnostics. PCFs can find applications in cytometry (in particular, for determining the vitality, apoptosis, and necrosis of cells), biological tissue engineering (nerve fiber growth monitoring), and the development of highly efficient and bright light sources, predominantly for the blue, red, and IR spectral regions corresponding to the optimum absorption by plants. In the field of optical metrology, the proposed PCFs can be useful for the creation of ultrawideband light sources for optical frequency synthesizers. The development of PCF structures with controlled FPBs will provide nanostructured materials for official documents (requiring protection against falsification), special fabrics, protective coatings, etc., where a certain reflection spectrum is necessary.

Acknowledgments. This study was supported in part by the US Civilian Research and Development Foundation for the Independent States of the Former Soviet Union, CRDF award No. REC-006.

REFERENCES

1. N. Slepov, Elektronika, No. 5, 80 (2004).
2. J. Broeng, T. Sondergaard, S. E. Barkou, *et al.*, J. Opt. A: Pure Appl. Opt. **1**, 477 (1999).
3. J. C. Knight, T. A. Birks, R. F. Cregan, *et al.*, Opt. Mater. **11**, 143 (1999).
4. A. B. Fedotov, A. M. Zheltikov, A. A. Ivanov, *et al.*, Laser Phys. **10**, 723 (2000).
5. A. M. Zheltikov, Usp. Fiz. Nauk **174**, 73 (2004).

Translated by P. Pozdeev

Technical Physics Letters, Vol. 31, No. 12, 2005, pp. 1022–1025. Translated from Pis'ma v Zhurnal Tekhnicheskoĭ Fiziki, Vol. 31, No. 23, 2005, pp. 61–67.

Thin Fullerene-Containing Films Synthesized by Ion Beam Sputtering of Fullerene Mixtures with Doping Additives in Vacuum

A. P. Semenov[a,*], I. A. Semenova[a], N. V. Bulina[b], V. A. Lopatin[b], N. S. Karmanov[c], and G. N. Churilov[b]

[a] *Department for Physical Problems, Presidium of the Buryatian Scientific Center, Siberian Division, Russian Academy of Sciences, Ulan-Ude, Buryatia, Russia*

[b] *Kirensky Institute of Physics, Siberian Division, Russian Academy of Sciences, Krasnoyarsk, Russia*

[c] *Institute of Geology, Siberian Division, Russian Academy of Sciences, Ulan-Ude, Buryatia, Russia*

** e-mail: semenov@pres.bsc.buryatia.ru*

Received February 21, 2005

Abstract—A new approach to the synthesis of films containing fullerenes and doping elements is described. It is suggested that a cluster mechanism of the target sputtering by accelerated ions makes possible the deposition of fullerenes on a substrate with a certain probability for dopant atoms being introduced into the cavities of fullerene molecules and a higher probability of their occurrence between fullerene molecules. The proposed method has been experimentally implemented by using an Ar^+ ion beam to sputter C_{60}/C_{70} fullerene mixtures (synthesized in a plasmachemical reactor at a pressure of 10^5 Pa) pressed into disk targets with a doping element (Fe, Na, B, Gd, or Se). The ion beam sputtering of dopant-containing fullerene mixtures in a vacuum of ~10^{-2} Pa allowed micron-thick films containing C_{60} and C_{70} fullerenes and the corresponding dopant element (Fe, Na, B, Gd, or Se) to be grown on quartz substrates. © *2005 Pleiades Publishing, Inc.*

Methods for the introduction of impurity elements into the cavity of a fullerene molecule are virtually the same as those used for the synthesis of fullerenes. The formation of fullerenes in the course of deposition of a carbon vapor occurring in a partly ionized state was described in [1, 2], The dominating factors in the synthesis of C_x carbon clusters can be the electron temperature and density in the plasma [3], since these parameters influence the cross section of the collisions of charged carbon clusters. The rate of formation of C_{k+m} clusters increases when the components C_k and C_m bear charges of the opposite signs. Qualitative analysis of the process of fullerene synthesis in plasma shows that the conditions facilitating the synthesis and increasing the yield of fullerenes and their derivatives can be created in the course of thin film deposition by ion beam sputtering of a fullerene target. An especially important task is to obtain the fullerene films containing doping elements.

The growth of thin films by ion beam deposition techniques [4] involves physical sputtering of the target material, transfer of the sputtered particles to the growth surface (substrate), and deposition (growth) of a film with required composition and structure. Taking into account the temporal and spatial factors, we may consider the elementary event of this growth process as beginning with sputtering of the target and ending with the internal physical and chemical transformations in the deposited film. From the standpoint of obtaining fullerene-containing films, the ion beam sputtering of fullerene mixtures has certain advantages. First, the flux of particles sputtered by accelerated ions from the target contains a considerable proportion of clusters of various dimensions [5]. Second, the reaction of compound formation in the case of reactive ion beam sputtering proceeds on a substrate [4, 6]. Third, a significant fraction of sputtered particles leave the target in the ionized state [7]. Fourth, the sputtering of clusters is accompanied by thermionic emission with the formation of a certain electron density in the plasma, whereby γ electrons can influence processes in the growing film. Fifth, this process makes possible simple and controlled filling of the growing film with doping elements. Finally, it is also very important that the sputtered clusters possess a relatively high temperature (~10–50 eV), which positively influences the course of the synthesis and the internal structure of the growing film even at a relatively low (~300 K) temperature of the substrate surface. Thus, the combined action and the forms of manifestation of all factors of the physical sputtering process are quite acceptable and even favorable for realization of the process of fullerene film synthesis in vacuum by means of the sputtering of fullerene mixtures containing doping elements with a beam of accelerated ions.

1063-7850/05/3112-1022$26.00 © 2005 Pleiades Publishing, Inc.

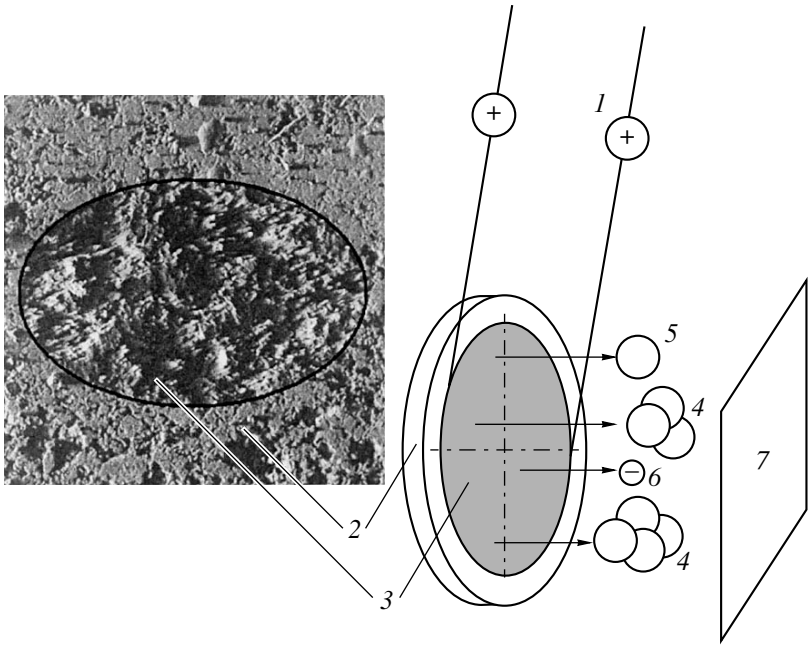

Fig. 1. Schematic diagram of the experimental arrangement: (*1*) Ar^+ ion beam; (*2*) target; (*3*) ion beam spot on the target surface; (*4*) molecular clusters (fullerene fragments); (*5*) doping atoms (Fe, Na, B, Gd, or Se); (*6*) γ electrons; (*7*) substrate. The inset shows a SEM micrograph of the target surface with a sputtered area.

The ability to contain atoms of foreign elements inside a carbon framework is the basic property of fullerene molecules. The introduction of such impurities into fullerene molecules substantially modifies their properties and significantly expands the spectrum of their possible practical applications.

Obviously, the large number of factors influencing the process of ion beam sputter deposition makes theoretical description of the process conditions and growth regimes an extremely difficult task. Below, we present the results of an experimental investigation into the synthesis of films containing fullerenes and an impurity element (Fe, Na, B, Gd, or Se) by means of sputtering of a pressed mixture containing C_{60}/C_{70} fullerenes and a doping element (Fe, Na, B, Gd, or Se) with a beam of Ar^+ ions in a vacuum of 10^{-2} Pa.

The initial fullerene mixture was synthesized in a plasmachemical reactor operating at an arc discharge frequency of 44 kHz and a pressure of 10^5 Pa [8]. The fullerene fraction was isolated from the obtained products by extraction with benzene. The initial fullerene mixture composition was as follows (weight fraction): C_{60}, 0.8; C_{70}, 0.15; higher fullerenes, 0.04; $C_{60}O$ and $C_{70}O$ oxides, 0.01. The targets were prepared by adding a powdered doping element (Fe, Na, B, Gd, or Se) in a preset amount (see table) to the fullerene mixture and pressing disks with a diameter of 20 mm and a thickness of 3 mm under a pressure of ~30 kgf/cm^2.

The sample films were grown in a vacuum of 2×10^{-2} Pa in the course of sputtering of a target with a beam of accelerated Ar^+ ions. The experiments were performed in a setup described elsewhere [4, 9], using the scheme depicted in Fig. 1. According to this scheme, ions *1* with a total beam current of 5–10 mA were formed in the plasma of magnetron discharge with cold hollow cathode [10] and accelerated to an energy of 5–10 keV, which corresponded to an ion velocity of $\sim 1.5 \times 10^5$ m/s. The ion beam was continuously incident onto the surface of target *2* at an angle of 45°–60° over a time period of 8 h, which corresponded to a total ion fluence of $\sim 5 \times 10^{16}$ cm^{-2}. As a result, a flux of particles was sputtered from spot *3* of the ion beam projection onto the target surface. According to [5, 7], the sputtered flux was expected to consist of molecular clusters *4* (fullerene fragments), atoms *5* of doping elements (Fe, Na, B, Gd, or Se), and electrons *6*. The sputtered particles were deposited onto the surface of a fused quartz substrate *7*, where a film was synthesized and grown to a total thickness of ~1 μm under nonequilibrium conditions at a substrate temperature of 300 K. The film thickness was measured using a microinterferometer (MII-4) of the Linnik type.

Despite the aforementioned advantages of the ion beam deposition process, manifested by the relative

The content of doping elements in fullerene mixtures

Element	Fe	Na	B	Gd	Se
Mass fraction in fullerene mixture	0.02	0.01	0.01	0.003	0.01

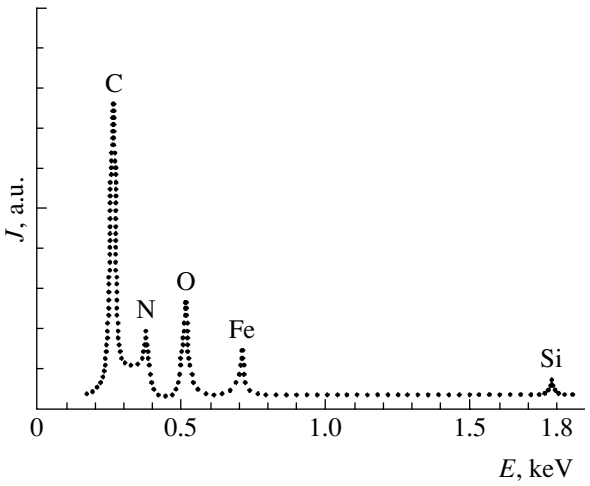

Fig. 2. X-ray emission spectrum of a thin film obtained by ion sputtering of a target containing fullerenes and iron as the doping element.

simplicity of maintaining the required regime of synthesis, the complex interrelation of separate parameters and their uncertainty lead to difficulties in the optimization of the process. The surface morphology of the grown films was studied using a LEO 1430VP scanning electron microscope (SEM). The observed SEM micrographs showed smooth and even growth surface, reproducing the roughness of a fused quartz substrate. The average roughness height was ~6.5 nm. The film structure and phase composition were studied by X-ray diffraction on a Rigaku diffractometer using CuK_α radiation. These measurements showed the obtained films to be X-ray amorphous. The films were insoluble in nonpolar solvents and contained a large proportion of various carbon-based molecules and fragments. The Raman spectra of the deposited films (measured using a Bruker RFS 100/S Fourier transform spectrometer) displayed no bands characteristic of the C_{60} and C_{70} molecules. However, the mass spectra (obtained using a Bruker Biflex III time-of-flight spectrometer with laser ionization) showed that C_{60} and C_{70} molecules are present in the films. These data confirmed the formation of fullerenes due to the merging of clusters (fullerene fragments) under the conditions of their stopping and deposition on the growth (substrate) surface. The films exhibited lower volatility as compared to that of the initial fullerene mixture. Based on these data, we may suggest that fullerene molecules in the films occur in a polymerized state. The polymerization process can be stimulated by γ electrons, which are knocked out from the film and continuously irradiate the growing film.

The X-ray spectral analysis of the films (performed using an Oxford Instruments INCA Energy 300 energy-dispersive analyzer) showed the X-ray emission peaks due to doping elements (Fe, Na, B, Gd, or Se) introduced into the fullerene mixture. These data confirmed the stable transport of doping elements from sputtered targets and filling of the deposited films. In addition to the peaks of C and doping elements (Fe, Na, B, Gd, or Se), the spectra contained the peaks of N, O, and Si. For example, Fig. 2 presents the typical X-ray emission spectrum of a film obtained using the ion beam sputtering of an iron-containing fullerene target. The appearance of Si and O peaks in this spectrum is probably related to the presence of a substrate. In addition, O and N can appear as a result of adsorption from the gas phase on a highly reactive surface of the deposit [11].

By changing the parameters of the ion beam sputtering process and the deposition conditions, it is possible to control both the growth of a fullerene film and the content of doping elements in the deposit. The results of investigation of the surface morphology (Fig. 1) of the initial target *2* and the sputtered area *3* showed that, within a relatively short sputtering time (8 h), the beam of accelerated ions produced a significant change in the surface microrelief, which showed evidence for a nonuniform etching of the fullerene powder in the direction of incidence of the ion beam. The surface relief with a characteristic columnar structure observed in the ion beam spot *3* (Fig. 1) is indicative of a nonthermal ("cold") decomposition of the surface of a pressed fullerene mixture.

Thus, the ion beam bombardment leads to breakage of the carbon framework of fullerene molecules in the target mixture containing a doping element, as well as to the sputtering and transfer of clusters (molecular fragments) and doping elements to the growth surface. At the same time, the obtained results show evidence of the possible "assembly" of the carbon framework of fullerene molecules on the substrate surface, which results in the formation of films containing fullerene molecules and doping elements. This mechanism of the process of ion beam sputter deposition of fullerenes (under the conditions of uncertainty [5] in the sputtering and transfer of the carbon framework of C_{60} and C_{70} molecules with diameters of ~0.71 nm) is consistent with the detection of both molecular fragments and C_{60} and C_{70} molecules in the obtained films. It is highly probable that doping elements can enter into the matrix of the carbon framework, with the formation of endohedral fullerenes, whereas the dopant atoms not entering into the carbon framework can participate in the formation of exohedral fullerenes. Thus, it is probable that dopant atoms can occur inside the C_{60} and C_{70} molecules synthesized via the assembly of molecular fragments on the substrate, or that dopant atoms are more likely involved in the intermolecular bonds outside these molecules. However, estimation of these probabilities require additional experiments, with investigation of the process of ion beam sputter deposition *in situ* using high-resolution mass spectrometry.

Acknowledgments. This study was supported by INTAS within the framework of the project no. 2001-2399.

REFERENCES

1. A. V. Eletskiĭ, Usp. Fiz. Nauk **164**, 1007 (1994) [Phys. Usp. **37**, 927 (1994)].
2. N. I. Alekseev and G. A. Dyuzhev, Zh. Tekh. Fiz. **69** (12), 42 (1999) [Tech. Phys. **44**, 1093 (1999)].
3. G. N. Churilov, A. S. Fedorov, and P. V. Novikov, Pis'ma Zh. Éksp. Teor. Fiz. **76**, 604 (2002) [JETP Lett. **76**, 522 (2002)].
4. A. P. Semenov, *Beams of Scattering Ions: Production and Application* (Izd. BNTs SO RAN, Ulan-Ude, 1999) [in Russian].
5. *Sputtering by Particle Bombardment*, Ed. by R. Behrisch (Springer-Verlag, New York, 1991), Vol. 3.
6. S. G. Galanin, Candidate's Dissertation (Moscow, 1995).
7. *Sputtering of Solids: Principles and Applications*, Ed. by E. S. Mashkova (Mir, Moscow, 1989) [in Russian].
8. G. N. Churilov, Prib. Tekh. Éksp., No. 1, 5 (2000).
9. A. P. Semenov and I. A. Semenova, Zh. Tekh. Fiz. **74** (4), 102 (2004) [Tech. Phys. **49**, 479 (2004)].
10. A. P. Semenov and I. A. Semenova, Zh. Tekh. Fiz. **75** (4), 48 (2005) [Tech. Phys. **50**, 434 (2005)].
11. T. L. Makarova, I. B. Zakharova, T. I. Zubkova, and A. Ya. Vul', Fiz. Tverd. Tela (St. Petersburg) **41**, 354 (1999) [Phys. Solid State **41**, 319 (1999)].

Translated by P. Pozdeev

Technical Physics Letters, Vol. 31, No. 12, 2005, pp. 1026–1028. Translated from Pis'ma v Zhurnal Tekhnicheskoĭ Fiziki, Vol. 31, No. 23, 2005, pp. 68–74.

Composite Fluoroplastic Fibrous Filtration Membranes

A. A. Shutov

Obninsk State Technical University of Nuclear Power Engineering, Obninsk, Russia
e-mail: shutov@iate.obninsk.ru

Received July 20, 2005

Abstract—New fibrous materials and related composite membranes have been obtained using fluoroplastic copolymer fibers produced by means of electrospinning. The composite membranes comprise alternating layers of fine and coarse fibers performing different functions: thin fibers determine the filtration properties, while thick fibers provide the necessary mechanical strength. © *2005 Pleiades Publishing, Inc.*

Introduction. Electrospinning is a method of obtaining fibers from polymeric liquids under the action of an applied electrostatic field. The electrospinning technology is as follows. A high voltage is applied to a polymeric liquid that outflows from a capillary, so that the liquid becomes electrified. The electric charges induced in the liquid exhibit acceleration in the applied electric field and entrain the surrounding liquid. The uniformly accelerated liquid stretches into a thin jet, thus forming a thread. Using this method, it is possible to obtain fibers with diameters ranging from 10 nm to 10 μm [1].

The jet radius r at a distance of $z \gg r_0$ from the capillary edge (r_0 is the capillary radius) is given by the formula [2, 3]

$$r = \left(\frac{\rho Q^3}{2\pi^2 IU}\right)^{1/4}, \quad (1)$$

where ρ is the density of the liquid, Q is the flow rate in the capillary, $U = U(z)$ is the potential at a point with the coordinate z, and I is the electric current carried by the jet. Formula (1) gives an asymptotic value of the jet radius in a strong electric field, that is, under the conditions where electric forces predominate over the capillary forces and gravity. In this case, the kinetic energy of the jet far from the capillary edge is much greater than the initial value, which explains why the capillary radius does not enter explicitly into expression (1).

The jet (and the resulting fiber) carries an electric charge of certain sign. In a homogeneous electric field with the potential $U = Ez$, the electric current transported by the jet can be expressed as [4]

$$I = kE\sqrt{\pi\lambda\varepsilon_0 r_0 Q}, \quad (2)$$

where $k \approx 2$–6 is a dimensionless constant, E is the electric field strength, λ is the conductivity of the liquid, and ε_0 is the permittivity. Using Eqs. (1) and (2), we obtain the following relation:

$$r \sim \frac{Q^{5/8}}{E^{1/2}\lambda^{1/8}}. \quad (3)$$

Under real conditions, the electric field strength is restricted to a level of 10^6–10^7 V/m, which corresponds to the onset of discharge phenomena violating the steady flow. This limitation of the electric field strength and a weak dependence on the conductivity imply that the task of obtaining thin jets (and fibers) reduces essentially to the problem of providing low steady flow rates.

Formulas (1)–(3) were obtained for a Newtonian liquid. From the standpoint of physics, the independence of these relations on the liquid viscosity has a simple explanation: under the conditions of one-dimensional pumping, the supplied electric energy encounters no viscous dissipation and is converted virtually without losses into the kinetic energy of the liquid [3, 5].

In the case of electrospinning of polymer solutions, one has to take into account at least two additional factors. First, it is necessary to take into account evaporation of the solvent, which results in the fiber radius r_f at the deposition site (collector electrode) being smaller than the value given by formula (1):

$$r_f = \sqrt{\frac{c}{\delta + c(1-\delta)}}\left(\frac{\rho Q^3}{2\pi^2 IU_0}\right)^{1/4}. \quad (4)$$

Here, U_0 is the potential difference between the capillary and collector, c is the polymer concentration in solution, $\delta = \rho_p/\rho_s$, and ρ_p and ρ_s are the polymer and solvent densities, respectively.

Second, the electric field energy in a polymeric liquid can be partly spent for structurization related to the orientation of polymer chains. The structurization leads

to an increase in the jet radius as compared to that given be formula (1); this process is strongly dependent on the polymer properties (chain length and flexibility) and on the solvent quality [6–8].

In the case of low-concentration solution of a low-molecular-weight polymer, the non-Newtonian character of the liquid medium weakly affects the jet (fiber) radius. At the same time, the intensity of evaporation of the solvent can be used as a parameter controlling the process of material formation. A polymer composition solution prepared using highly volatile solvents allows dry fibers to be obtained on the collector electrode, which results in the formation of highly loose fibrous materials because of the mutual repulsion of charged fibers. In the other limiting case, whereby a polymer is dissolved in a low-volatility solvent, the jet does not acquire the shape of a fiber and a material deposited on the collector appears as a monolithic film. By combining high- and low-boiling solvents, it is possible to obtain materials with a desired packing density of deposited fibers.

In accordance with the general laws of the theory of filtration, a fine level of filtration through a fibrous material is achieved by decreasing the diameter of fibers [1]. In order to decrease the level of hydrodynamic drag, it is also necessary to reduce the material layer thickness. However, it is necessary to take into account that both these factors lead to a decrease in mechanical strength of the filter material. Advantageous combination of good mechanical strength and fine filtration ability can be achieved using inhomogeneous membranes having layered structures. According to this approach, the main filtration layer composed of fine fibers is deposited onto a sublayer of relatively thick fibers, which ensures the necessary mechanical strength of the composite material. In addition, the layer of coarse fibers plays the role of a preliminary filter, thus increasing the working life of the main filtration layer. By controlling the parameters of the electrospinning process, it is possible to deposit sequential layers of preset thickness, composed of fibers with diameters in a selected range.

This study was aimed at selecting polymeric liquid compositions (polymer + solvent) so as to obtain electrospun fibers containing residual solvents, which would be capable of mutual sticking without losing the fiber shape. Then, evaporation of the residual solvent leads to the formation of a fibrous material with mechanical properties close to those of a monolithic polymer film, which is due to the "glued" joints between fibers at the numerous points of their mutual contact. On the other hand, the fibrous structure provides for porosity of the material. Loose fibrous structures applicable to the filtration of gaseous media can be obtained from 10–20% polymer solutions based on low-boiling solvents with boiling temperatures $T_b <$ 100°C. Fibers capable of mutual sticking can be obtained from less concentrated solutions involving high-boiling solvents.

Experimental results. All parameters of the electrospinning process must be mutually consistent. The choice of parameters is based on the following qualitative considerations. The most important control parameter is the flow rate of a polymeric liquid via the capillary. The degree of jet (fiber) drying depends on the interelectrode distance. The potential difference should be maximal but not violate the steady flow and stable deposition process. Materials with a total thickness on the order of 50–150 μm should be deposited onto a substrate (we used polymeric and metallic grids). Preliminary preparation of polymer solutions must include the stage of filtration, in which undissolved polymer and mechanical impurities are removed.

We have used the electrospinning technology to obtain composite fibrous membranes made of fluoroplastic compositions based on (i) a copolymer of tetrafluoroethylene with vinylidene fluoride (F-42) and (ii) a copolymer of vinylidene fluoride with hexafluoropropylene (F-26). The initial polymer solutions were prepared using acetone–dimethylformamide (AC–DMF) mixtures. The optimum solution concentrations were 9–10% of F-42 in 1 : 1 AC–DMF mixture and 8% F-26 in 1:0.1 AC–DMF mixture.

The interelectrode distance was 20 cm, the potential difference U_0 was varied in the interval from 20 to 40 keV, and the liquid flow rate could be smoothly controlled in the range from 3×10^{-3} to 4×10^{-5} cm^3/s. The best filtration and mechanical characteristics were observed for deposited materials with a layered structure, consisting of a sublayer of wet, relatively thick fibers capable of sticking to a substrate grid, and an upper layer of thin fibers.

The composite membranes formed on a polymer (nylon) or metal grid exhibited high elasticity. We have manufactured membranes with a sandwich structure, comprising a layer of fine fibers with a diameter of ~0.05 μm confined between layers of relatively thick fibers with a diameter of ~1 μm.

Figures 1 and 2 present electron micrographs of the transverse section of a membrane based on F-42 copolymer, which show the material structure on various levels. The obtained membranes had a pore size of 0.6–1 μm and a porosity of about 70% and were characterized by the filtration capacity with respect to air on a level of ~10^4 m^3/(m^2 h bar) at a total thickness of 100–150 μm.

Discussion. Membranes made of thin electrospun polymer fibers exhibit certain distinctive features in comparison to the filtration materials based on monolithic films and sintered powders of micron-sized particles. First, the permeability of polymeric fibrous membranes is controlled by changing the fiber diameter, which can be varied within a rather broad range (0.01–10 μm). Second, the fibrous membranes have a relatively high porosity (~70%). Third, these membranes

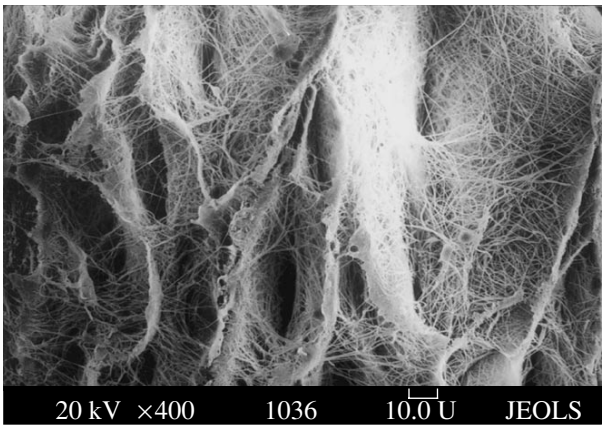

Fig. 1. Electron micrograph of the transverse section of a material based on F-42 copolymer fibers obtained by means of electrospinning (magnification, ×400).

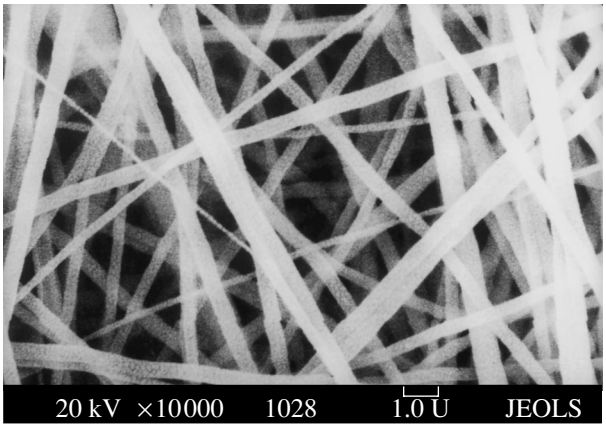

Fig. 2. Electron micrograph of the transverse section of a fibrous membrane made of F-42 copolymer fibers obtained by means of electrospinning (magnification, ×10000).

possess a relatively small total thickness (~50–100 μm) at a high filtration capacity. On the other hand, such thin materials possess low mechanical strength and have to be formed on and used with substrates. A substrate must be of a homogeneous thickness and possess good adhesion to polymer in order to ensure reliable gluing of the polymeric membrane.

A filter material with inhomogeneous structure implies the need for optimization of the mechanical and filtration properties. The fluoroplastic membranes manufactures by means of electrospinning are composite materials consisting of several layers, which perform different functions. A layer of thick fibers provides the necessary mechanical strength, while thin fibers determine the filtration properties. By selecting a proper polymer solution composition, it is possible to develop a technology based on a single-capillary electrospinning process.

Acknowledgments. This study was supported jointly by the Russian Foundation for Basic Research and the Kaluga Oblast Administration (project no. 04-01-97225).

REFERENCES

1. I. V. Petryanov, V. I. Kozlov, P. I. Basmanov, and B. I. Ogorodnikov, *Fibrous Filtering Materials* (Znanie, Moscow, 1968) [in Russian].
2. V. N. Kirichenko, I. V. Petryanov, A. A. Shutov, *et al.*, Dokl. Akad. Nauk SSSR **289**, 817 (1986) [Sov. Phys. Dokl. **31**, 611 (1986)].
3. A. A. Shutov, Prikl. Mekh. Tekh. Fiz., No. 2, 20 (1991) [J. Appl. Mech. Tech. Phys. **32**, 162 (1991)].
4. N. M. Alontseva, V. M. Berezhnoi, and A. A. Shutov, Kolloidn. Zh. **57**, 629 (1995) [Colloid. J. **57**, 591 (1995)].
5. A. A. Shutov and A. A. Zakhar'yan, Prikl. Mekh. Tekh. Fiz., No. 4, 12 (1998) [J. Appl. Mech. Tech. Phys. **39** (4), (1998)].
6. J. J. Feng, Phys. Fluids **14**, 3912 (2002).
7. J. J. Feng, J. Non-Newtonian Fluid Mech. **116**, 55 (2003).
8. A. F. Spivak and Y. A. Dzenis, Appl. Phys. Lett. **73**, 3067 (1998).

Translated by P. Pozdeev

Technical Physics Letters, Vol. 31, No. 12, 2005, pp. 1029–1031. Translated from Pis'ma v Zhurnal Tekhnicheskoĭ Fiziki, Vol. 31, No. 23, 2005, pp. 75–80.

Stress-Induced Domain Structure Formation in Nanodimensional Barium Strontium Titanate Films

V. M. Mukhortov*, Yu. I. Golovko, V. V. Kolesnikov, and S. V. Biryukov

Southern Research Center, Russian Academy of Sciences, Rostov-on-Don, Russia

** e-mail: muhortov@ip.rsu.ru*

Received June 16, 2005

Abstract—Thin heteroepitaxial films of $Ba_xSr_{1-x}TiO_3$ (BST) with $x = 0.80$ possessing high structural perfection have been grown by RF magnetron sputtering on MgO(001) substrates. The microstructure and crystallographic characteristics of the BST films of various thicknesses have been studied using electron microscopy and X-ray diffraction. It is established that there is a threshold thickness at which the BST crystal lattice parameter in the direction perpendicular to the substrate exhibits a sharp change. © *2005 Pleiades Publishing, Inc.*

It has been repeatedly demonstrated [1–3] that the properties of thin ferroelectric films substantially differ from those of the corresponding bulk materials, which is related to a different mechanism of phase transitions in nanodimensional heteroepitaxial structures. The most important factor is a strong influence of mechanical stresses developed at the film–substrate interface. According to the existing theory, this factor leads to qualitative changes in the phase diagram [4] of the given ferroelectric material. These changes are manifested by anomalies in the thickness dependence of the physical properties (permittivity, crystal lattice parameters, etc.) of ferroelectric films, which are important for applications such as microwave control devices and ultrahigh-speed optical modulators. However, the experimental investigations of evolution of the properties of thin ferroelectric films are very restricted and are insufficient for judging the adequacy of existing theoretical notions.

This Letter presents the results of experimental investigation into the properties of heteroepitaxial $Ba_xSr_{1-x}TiO_3$ (BST) films with $x = 0.8$, highly perfect structure, and thicknesses varied in a broad range. It is demonstrated that variation of the film thickness is accompanied by anomalous changes in the BAST crystal lattice parameter, which is indicative of the development of instability and the phase transition in the system studied.

The heteroepitaxial BST films were grown using RF magnetron sputtering. The experimental setup and the methods of optical monitoring of the growth process have been described elsewhere [5–7]. It was established [5–7] that the main mechanism of excitation of the optical emission from oxygen (working gas) is the direct electron impact in a beam of electrons, which are formed in the near-electrode region of discharge and have an energy of eU_0 (U_0 is the voltage drop in a stationary electric field at the electrode). In the negative glow region, the exponential decay of the emission intensity ($J = A\exp(-h/b)$) with increasing distance h from the dark cathode space is related to the dissipation of energy as a result of the inelastic collisions of electrons with oxygen atoms (the coefficient b characterizes the energy of electrons arriving from the cathode space to the negative glow region of the RF discharge, where the substrate is located. The growth of heteroepitaxial films takes place for $b > b_{ts}$ and $p > p_{ts}$, where b_{ts} and p_{ts} are the threshold values of the parameter b and the working gas pressure p (Fig. 1). Investigations of the morphology of the film surface by means of the electron microscopy and atomic force microscopy showed that films grown in the interval between b_{ts} and a certain critical value b_c in the range of oxygen pressures above

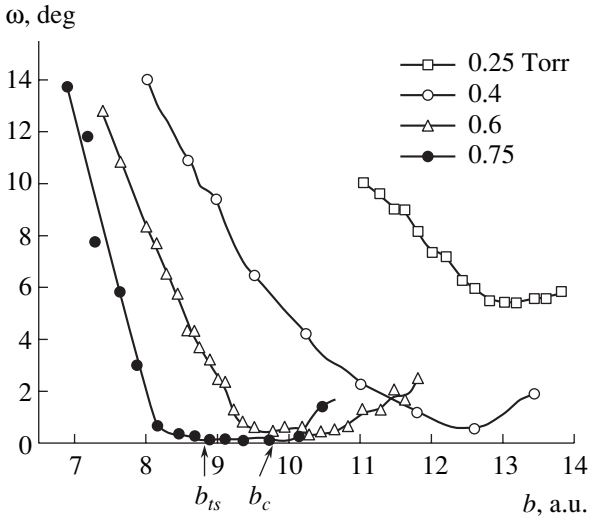

Fig. 1. Plots of the normal misorientation angle ω versus energy parameter b for BST films grown on MgO(001) substrates by RF magnetron sputtering at various oxygen pressures.

1063-7850/05/3112-1029$26.00 © 2005 Pleiades Publishing, Inc.

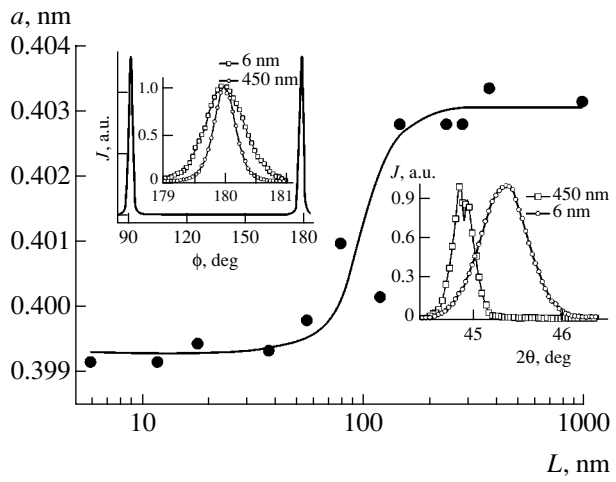

Fig. 2. A plot of the lattice parameter a versus thickness L of BST films grown on MgO(001) substrates. The insets show the X-ray diffraction reflections (002) (right) and (113) (left) for 6- and 450-nm-thick films.

0.6 Torr possessed atomically smooth surfaces. Under these conditions, the growth proceeds via a layer mechanism (i.e., without the formation of three-dimensional nuclei with a density of screw dislocations ~10^7 cm^{-2}), which allows continuous films to be obtained with a thickness of several monolayers. All films had a heteroepitaxial structure and were oriented parallel to the substrate.

The structural perfection of the films, their heteroepitaxial character, and the mutual orientation of film and substrate were determined using X-ray diffraction measurements performed on a DRON-4-07 diffractometer. The intensities of diffraction reflections in the films with thicknesses above 6 nm were sufficient for a complete structural analysis. The typical halfwidth of (002) reflections for films with thicknesses above 450 nm (Fig. 2, right-hand inset) was below 0.1°. This value is significantly lower than the published data for BST films on MgO substrates [8, 9]. Figure 2 (left-hand inset) also demonstrates the (113) reflection measured for the sample rotated in the base plane (ϕ scan), which shows that the azimuthal misorientation is below 1°. In such thin films with homogeneous compositions, the internal stresses are determined by the lattice mismatch between the film and substrate, the difference of their thermal expansion coefficients, the deformation related to the first phase transition, the deformation as a result of cooling from the growth temperature (680°C) to room temperature, and the presence of defects of the vacancy and dislocation types.

Figure 2 shows a plot of the lattice parameter a versus film thickness L (measured along the normal to the substrate surface). As can be seen, the lattice parameter exhibits a sharp change in the region of film thicknesses between 35 and 200 nm and stabilizes again for $L >$ 200 nm. This behavior qualitatively agrees with the physical notions about sharp changes in the lattice parameter as a result of the phase transitions in the film–substrate system, which are related to the development of ferroelastic instability and the generation of misfit dislocations leading to partial mechanical unloading of the strained film [10]. However, the shape of the a versus L curve presented in Fig. 2 significantly differs from that reported recently by Alpay *et al.* [11]. In particular, the critical film thickness according to our data differs from the value (~5 nm for a growth temperature of 700°C) calculated in [11] assuming the generation of misfit dislocations.

We believe that the main limitation of the thermodynamic modeling of the influence of misfit dislocations is related to the fact that the true critical film thickness for the formation of dislocations and the equilibrium linear density of dislocations may differ from the observed values because of kinetic factors [12], which are determined to a significant extent by the quality of heteroepitaxial structures and by the growth mechanisms. A difference between the crystal lattice parameters in a heterostructure leads to the development of internal stresses (misfit stresses), which significantly influence the evolution of the structure and properties of epitaxial films. As the film thickness exceeds a certain critical value, the misfit stresses are partly accumulated at the film–substrate interface due to the formation of misfit dislocations. In recent years, it was suggested to use buffer layers with preset structure in order to increase the critical film thickness [13, 14]. In this study, we have realized the conditions of film growth involving the formation of screw dislocations at a low density, which leads to a decrease in the number of edge dislocations (small-angle grain boundaries) [15] and the related increase in the critical film thickness.

According to our results, spontaneous polarization in BST films with thicknesses below ~35 nm occurs in the substrate plane (*a*-domain state). In this range of film thicknesses, tensile stresses are predominating because the lattice parameter of MgO is greater than that of the BST film. When the critical thickness (~35 nm) is reached, a new phase consisting of both *a*- and *c*-domains is formed within a narrow interval of L values, which leads to a decrease in the level of tensile stresses. Thicker films ($L >$ 200 nm) are characterized by the development of compressive stresses determined by a difference between the thermal expansion coefficients of the film and substrate. These compressive stresses set spontaneous polarization in the direction perpendicular to the substrate plane (*c*-domain state).

Acknowledgments. This study was supported by the Russian Foundation for Basic Research, project no. 05-02-17191.

REFERENCES

1. Z.-G. Ban and S. P. Alpay, J. Appl. Phys. **91**, 9288 (2002).

2. J. S. Horwitz, W. Chang, W. Kim, *et al.*, J. Electroceram. **4**, 357 (2000).
3. Y. Kim, D. Lee, and B. Park, Appl. Phys. Lett. **85**, 2328 (2004).
4. A. Sharma, Z.-G. Ban, S. P. Alpay, *et al.*, Appl. Phys. Lett. **84**, 4959 (2004).
5. V. M. Mukhortov, Y. I. Golovko, G. N. Tolmachev, *et al.*, Ferroelectrics **247**, 75 (2000).
6. V. M. Mukhortov, Y. I. Golovko, G. N. Tolmachev, *et al.*, Zh. Tekh. Fiz. **69** (12), 87 (1999) [Tech. Phys. **44**, 1477 (1999)].
7. V. M. Mukhortov, Y. I. Golovko, G. N. Tolmachev, *et al.*, Zh. Tekh. Fiz. **68** (9), 99 (1998) [Tech. Phys. **43**, 1097 (1998)].
8. C. Li, Z. Chen, D. Cui, *et al.*, J. Appl. Phys. **86**, 4555 (1999).
9. H. Terauchi, Y. Watanabe, H. Kasatani, *et al.*, J. Phys. Soc. Jpn. **61**, 2194 (1992).
10. H. Lia, A. L. Roytburd, and S. P. Alpay, Appl. Phys. Lett. **78**, 2354 (2001).
11. S. P. Alpay, I. B. Misirlioglu, A. Sharma, *et al.*, J. Appl. Phys. **95**, 8118 (2004).
12. W. D. Nix, Metall. Trans. **20**, 2217 (1989).
13. L. Zepeda-Ruiz, W. H. Weinberg, and D. Maroudas, J. Appl. Phys. **85**, 3677 (1999).
14. Y. Obayashi and K. Shintani, J. Appl. Phys. **88**, 105 (2000).
15. V. I. Vladimirov and A. E. Romanov, *Dislocations in Crystals* (Nauka, Leningrad, 1986), p. 224 [in Russian].

Translated by P. Pozdeev

Technical Physics Letters, Vol. 31, No. 12, 2005, pp. 1032–1035. Translated from Pis'ma v Zhurnal Tekhnicheskoĭ Fiziki, Vol. 31, No. 23, 2005, pp. 81–88.

Electric Resistance and Magnetoresistance of a Two-Layer Epitaxial Heterostructure (30 nm)$La_{0.67}Ca_{0.33}MnO_3$/(30 nm)$La_{0.67}Ba_{0.33}MnO_3$

Yu. A. Boikov* and V. A. Danilov

Ioffe Physicotechnical Institute, Russian Academy of Sciences, St. Petersburg, 194021 Russia

** e-mail: yu.boikov@mail.ioffe.ru*

Received July 7, 2005

Abstract—Two-layer epitaxial heterostructures (30 nm)$La_{0.67}Ca_{0.33}MnO_3$/(30 nm)$La_{0.67}Ba_{0.33}MnO_3$ (LCMO/LBMO) have been grown by laser deposition on single crystal (001)$LaAlO_3$ (LAO) substrates. In this system, the upper (LCMO) layer occurs under the action of tensile stresses in the substrate plane, whereas the lower (LBMO) layer exhibits biaxial compression. The formation of a 30-nm-thick LCMO film on the surface of the 30-nm-thick LBMO layer leads to an increase in the level of mechanical stresses in the latter layer. The maximum electric resistivity ρ of the (30 nm)LCMO/(30 nm)LBMO/LAO structure was observed at a temperature 25–30 K below that corresponding to the maximum of the ρ(*T*) curve for a single (30 nm)LBMO film on the same LAO substrate. © *2005 Pleiades Publishing, Inc.*

In recent years, the electrical and magnetic properties of thin films of perovskitelike manganites of the $La_{1-x}A_xMnO_3$ type (A = Ba, Ca, Sr, …) have been extensively studied in view of their potential use in magnetoresistive sensors [1–3]. From the standpoint of spintronic devices, the most interesting materials are manganite films featuring the ferromagnetic phase transition at temperatures close to room temperature. For example, the Curie temperatures of $La_{0.67}Ca_{0.33}MnO_3$ (LCMO) and $La_{0.67}Ba_{0.33}MnO_3$ (LBMO) solid solutions are 270 and 330 K, respectively [4, 5]. The process of ferromagnetic ordering of spins in the volume of thin LCMO and LBMO films strongly depends on the magnitude and type of biaxial mechanical stresses in these materials.

This Letter presents the results of experimental investigation of the structure and electric resistance of two-layer epitaxial LCMO/LBMO heterostructures grown by laser deposition on single crystal (001)$LaAlO_3$ (LAO) substrates. The lattice parameter of pseudocubic LBMO crystals (a_1 = 3.910 Å [5]) is greater than the corresponding values for LAO (pseudocubic, a_2 = 3.780 Å [6]) and LCMO (pseudocubic, a_3 = 3.858 Å [7]), while the thermal expansion coefficients of LAO, LBMO, and LCMO are close [7, 8]. The differences in the crystal lattice parameters of the substrate and manganite layers in the LCMO/LBMO/LAO structure must lead to contraction of the LBMO layer in the substrate plane, while the LCMO film must exhibit a biaxial extension. A change in the electric resistance of a thin manganite film caused by the growth of a thin film with different crystal lattice parameter on its surface has not been studied until now.

The two-layer (30 nm)LCMO/(30 nm)LBMO heterostructures on (001)LAO substrates were grown by means of laser deposition (ComPex 200, KrF, λ = 248 nm, τ = 30 ns). For comparison, we also studied (30 nm)LBMO/LAO samples prepared under identical conditions. The conditions of the laser deposition of thin manganite films on (100)LAO substrates are described in detail elsewhere [9].

The phase composition and structure of the LCMO and LBMO films were determined by X-ray diffraction (Philips X'pert MRD; rocking curves; ϕ and ω/2θ scans) as described in [7]. The crystal lattice parameters in the manganite films were calculated using the 2θ values for (004) and (303) peaks in the diffractograms [9].

The resistance *R* of the heterostructures was measured in the Van der Pauw geometry using a probing current passing parallel to the substrate plane. The measurements were performed in the absence of a magnetic field and with a magnetic field ($\mu_0 H$ = 0–5 T) oriented in the substrate plane parallel to the current direction. The resistivity ρ was calculated as $\rho = d\pi R/\ln 2$ [10], where d = 30 nm is the layer thickness (both LCMO and LBMO films were 30 nm thick).

Figure 1 shows the typical X-ray diffraction pattern of an LCMO/LBMO/LAO heterostructure, which displays only (00*n*) reflections from the manganite layers and the substrate. The peaks belonging to the upper and lower manganite layers in the heterostructure were

clearly resolved (see the inset in Fig. 1). The presence of the Laue satellite peaks (indicated by the arrows) is evidence for uniform thicknesses of the LCMO and LBMO layers. The results of the X-ray diffraction measurements (ω/2θ and ϕ scans) showed that the LCMO and LBMO layers have clear predominant orientation, both azimuthal (in plane) and relative to the normal to the substrate plane. The unit cell of the LBMO layer in the LCMO/LBMO/LAO heterostructure is substantially distorted: the lattice parameter in the substrate plane (see table, $a_{\parallel} = 3.863 \pm 0.005$ Å) is significantly smaller than the value measured in the normal direction ($a_{\perp} = 3.957 \pm 0.005$ Å) (see table). In the case of a single film (30 nm)LBMO/LAO, the unit cell distortion is not as large (see table). It should be noted that the unit cell volume of this film, $V_{\text{eff}} = a_{\parallel}^2 \times a_{\perp} \approx 59.43$ Å^3, was smaller than V_{eff} for the bulk LBMO crystal (≈59.78 Å^3 [5]) but greater than that for the LBMO layer (≈59.05 Å^3) in the LCMO/LBMO/LAO heterostructure (see table).

The X-ray diffraction data indicate that both the 30-nm-thick LBMO layer in the LCMO/LBMO/LAO heterostructure and the single (30 nm)LBMO/LAO film occur under the action of biaxial compressive stresses in the substrate plane. The formation of a 30-nm-thick film of LCMO (having a lattice parameter smaller than that of LBMO) on the surface of the (30 nm)LBMO/LAO layer leads to an additional increase in the level of mechanical stresses in the latter layer caused by the contact with a relatively thick LAO substrate. Mechanisms responsible for a change in V_{eff} in manganite films grown on substrates with a significant lattice mismatch were recently considered in [11]. In contrast to the lower (LBMO) layer, the LCMO film is the LCMO/LBMO/LAO heterostructure occurring under the action of biaxial tensile stresses. For this reason, the unit cell parameter of this film in the substrate plane is greater than the value measured in the normal direction (see table). The full width at half maximum (FWHM) of the rocking curves for the (002) reflections of LCMO and LBMO layers in the LCMO/LBMO/LAO heterostructure was within 0.12°–0.18° (see table), in good agreement with our data reported in [12].

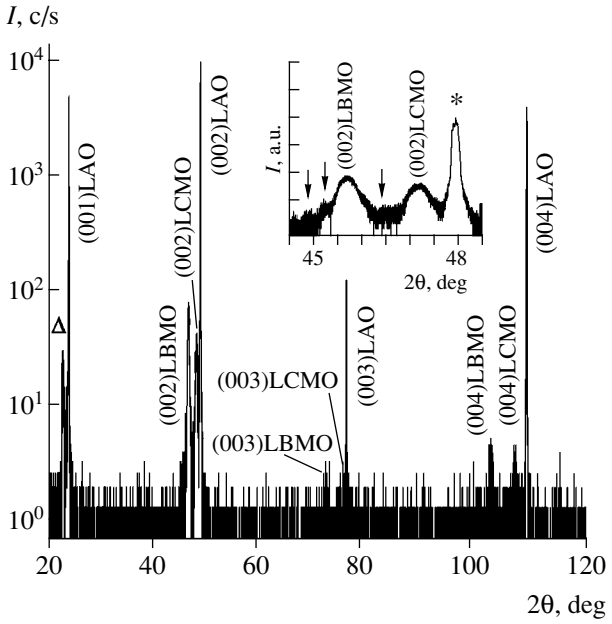

Fig. 1. The X-ray diffractogram (Cu$K_{\alpha 1}$, ω/2θ scan) of the LCMO/LBMO/LAO heterostructure measured with both incident and reflected beams lying in the plane perpendicular to the (001)LAO substrate. Symbol Δ indicates the (001) peaks of LCMO and LBMO films in the heterostructure. The inset shows a fragment of the same ω/2θ scan in the vicinity of the (002) reflections from the manganite films; the asterisk indicates the peak from the LAO substrate; arrows indicate the Laue satellite peaks.

Figure 2 (inset (a)) shows the temperature dependences of the resistivities of the LCMO/LBMO/LAO heterostructure and the single (30 nm)LBMO/LAO film measured in the absence of a magnetic field ($\mu_0 H = 0$). The maximum of the $\rho(T, \mu_0 H = 0)$ curve for the two-layer LCMO/LBMO/LAO heterostructure was observed at $T_M = 285$ K, that is, approximately 25 K below the position of maximum for the single (30 nm)LBMO/LAO film. Note also that the resistivity of the LCMO/LBMO/LAO heterostructure was greater than that of the (30 nm)LBMO/LAO film in the entire temperature range studied (Fig. 2, inset (a)). The main factor responsible for a decrease in T_M in elastically

Parameters of manganite films in laser-deposited epitaxial structures*

Heterostructure	Layer	Thickness d, nm	$a_{\perp}$, Å	$a_{\parallel}$, Å	V_{eff}, Å^3	FWHM, deg
LCMO/LBMO/LAO	LBMO	30	3.957	3.863	59.05	0.13
	LCMO	30	3.841	3865	57.38	0.18
LBMO/LAO	LBMO	30	3.948	3.880	59.43	0.12

* For the LAO substrate, the parameter of the pseudocubic unit cell determined using the X-ray diffraction data was $a_{\text{LAO}} = 3.786 \pm 0.005$ Å.

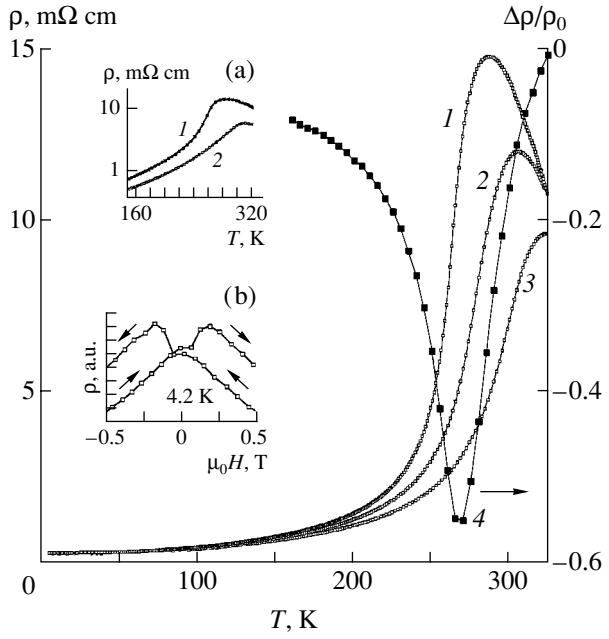

Fig. 2. Temperature dependences of the (*1–3*) resistivity ρ measured at $\mu_0 H$ = 0 (*1*), 2 (*2*) and 5 T (*3*) and (*4*) magnetoresistance $\Delta\rho/\rho_0(T, \mu_0 H = 2\ \text{T})$ of the LCMO/LBMO/LAO heterostructure. The inset (a) shows the $\rho(T, \mu_0 H = 0)$ curves for the (*1*) LCMO/LBMO/LAO heterostructure and (*2*) the (30 nm)LBMO/LAO film. The inset (b) shows fragments of the $\rho(T = 4.2\ \text{K}, \mu_0 H)$ curves measured for the LCMO/LBMO/LAO heterostructure during cyclic variation of $\mu_0 H$ in the interval from 5 T to –5 T and back.

stressed LBMO films is a relatively high (as compared to the bulk stoichiometric crystal) concentration of Mn^{4+} ions in the film volume [11].

The application of a magnetic field led to a decrease in the resistivity of the LCMO/LBMO/LAO heterostructure (Fig. 2). The position of maximum of $\rho(T, H)$ shifted toward higher temperatures with increasing $\mu_0 H$. The negative magnetoresistance $\Delta\rho/\rho_0 = [\rho(\mu_0 H = 2\ \text{T}) - \rho(H = 0)]/\rho(H = 0)$ for the two-layer LCMO/LBMO/LAO heterostructure reached a maximum (≈–0.55) at $T \approx 270$ K (Fig. 2). The analogous maximum ($\Delta\rho/\rho_0 \approx -0.42$) for the single (30 nm)LBMO/LAO film was observed at $T \approx 300$ K. At temperatures close to T_M, both manganite layers contribute to the magnetoresistance of the LCMO/LBMO/LAO heterostructure. For this reason, the peak in the temperature dependence of the magnetoresistance for the LCMO/LBMO/LAO heterostructure is wider than the analogous peaks for the separate epitaxial films of the perovskitelike manganites [13].

Figure 2 (inset (b)) shows how the resistivity of the LCMO/LBMO/LAO heterostructure varies depending on the applied magnetic field. At T = 4.2 K and $\mu_0 H$ = 5 T, the magnetization vector in both manganite layers of the LCMO/LBMO/LAO heterostructure was parallel to the magnetic field direction. When the applied field was varied over the cycle 5 T ⟶ 0 ⟶ –5 T ⟶ 0 ⟶ 5 T, the $\rho(\mu_0 H)$ curves exhibited a clear hysteresis. The maximum values of ρ were observed for $\mu_0 H \approx \pm 0.2$ T. The $\rho(\mu_0 H)$ curve measured when $\mu_0 H$ was decreased from 5 T to –5 T exhibited, in addition to the main maximum, a local maximum at a field strength close to zero (Fig. 2, inset (b)). A decrease in the resistivity of the LCMO/LBMO/LAO heterostructure with increasing magnetic field strength (for $\mu_0 H > 0.2$ T) is related to a decrease in the spatial misorientation of spins of manganese ions (primarily in the vicinity of grain boundaries) in the manganite layers. The presence of two maxima in $\rho(\mu_0 H)$ for the LCMO/LBMO/LAO heterostructure is related to the fact that the coercive field for the biaxially compressed LBMO layer is greater than the corresponding value for the biaxially extended LCMO film. According to [14], the vector of spontaneous magnetization in manganite films under the action of biaxial tensile stresses (i.e., in LCMO films in our heterostructures) is parallel to the substrate plane, whereas in the case of biaxial compressive stresses (i.e., in the LBMO layer) the spontaneous magnetization is parallel to the normal to the substrate plane. The observed behavior of $\rho(\mu_0 H)$ shows that the relative misorientation of the magnetization vectors in the upper and lower manganite layers of the LCMO/LBMO/LAO heterostructure can exhibit significant variations at $\mu_0 H < 0.2$ T.

In conclusion, it should be emphasized that a 30-nm-thick LCMO film grown on the surface of the (30 nm)LBMO/LAO layer causes an increase in the level of crystal lattice distortion and a decrease in the unit cell volume in the lower manganite layer of the LCMO/LBMO/LAO heterostructure. This influence is one of the factors responsible for a shift of the maximum on the temperature dependence of ρ for the heterostructure relative to the position of this maximum for a single (30 nm)LBMO/LAO film.

Acknowledgments. This study was supported in part by the Presidium of the Russian Academy of Sciences within the framework of the Program "Low-Dimensional Quantum Nanostructures" (project no. 9B19) and by the Russian Foundation for Basic Research (project no. 04-02-16212).

REFERENCES

1. M. Pannetier, C. Fermon, G. Le Goff, *et al.*, Science **304**, 1648 (2004).
2. S. S. P. Parkin, K. P. Roche, M. G. Samant, *et al.*, J. Appl. Phys. **85**, 5828 (1999).
3. A. Goyal, M. Rajeswari, R. Shreekala, *et al.*, Appl. Phys. Lett. **71**, 2535 (1997).

4. G. J. Snyder, R. Hiskes, S. DiCarolis, *et al.*, Phys. Rev. B **53**, 14434 (1996).
5. B. Weidenhorst, C. Höfener, Y. Lu, *et al.*, Appl. Phys. Lett. **74**, 3636 (1999).
6. R. W. G. Wyckoff, *Crystal Structure*, 2nd ed. (Interscience, New York, 1964), Vol. 2, p. 394.
7. P. Dai, J. Zhang, H. A. Mook, *et al.*, Phys. Rev. **54**, R3694 (1996).
8. C. Zuccaro, H. L. Berlincourt, N. Klein, and K. Urban, J. Appl. Phys. **82**, 5695 (1997).
9. Yu. A. Boikov and V. A. Danilov, Zh. Tekh. Fiz. **75** (7), 75 (2005) [Tech. Phys. **50**, 891 (2005)].
10. T. I. Kamins, J. Appl. Phys. **42**, 4357 (1971).
11. Yu. A. Boikov, R. Gunnarsson, and T. Claeson, J. Appl. Phys. **96**, 435 (2004).
12. Yu. A. Boikov and T. Claeson, Fiz. Tverd. Tela (St. Petersburg) **47**, 274 (2005) [Phys. Solid State **47**, 287 (2005)].
13. Yu. A. Boikov and V. A. Danilov, Pis'ma Zh. Tekh. Fiz. **31** (14), 50 (2005) [Tech. Phys. Lett. **31**, 605 (2005)].
14. H. S. Wang, Q. Li, K. Liu, and C. L. Chien, Appl. Phys. Lett. **74**, 2212 (1999).

Translated by P. Pozdeev

Technical Physics Letters, Vol. 31, No. 12, 2005, pp. 1036–1038. Translated from Pis'ma v Zhurnal Tekhnicheskoĭ Fiziki, Vol. 31, No. 23, 2005, pp. 89–94.

Fullerene Films Deposited by Evaporation in Vacuum Using Spot-Focused Annular Electron Beam

A. P. Semenov[a,*], I. A. Semenova[a], N. V. Bulina[b], A. S. Krylov[b], G. N. Churilov[b], and A. A. Semenova[b]

[a] *Department for Physical Problems, Presidium of the Buryatian Scientific Center, Siberian Division, Russian Academy of Sciences, Ulan-Ude, Buryatia, Russia*

[b] *Kirensky Institute of Physics, Siberian Division, Russian Academy of Sciences, Krasnoyarsk, Russia*

** e-mail: semenov@pres.bsc.buryatia.ru*

Received July 20, 2005

Abstract—A rapidly focused annular electron beam can provide for the effective evaporation of a fullerene mixture in a vacuum of ~10^{-2} Pa. A 1-kW beam focused into a spot within 0.1–1 s produces explosive evaporation of a fullerene target at an extremely high efficiency of heating. A comparison of the Raman and electronic absorption spectra of the initial fullerene powder and a film deposited upon its evaporation shows that C_{60} and C_{70} fullerenes are evaporated without rupture of C–C covalent bonds. The electron beam evaporation in vacuum has been successfully used to obtain fullerene films on substrates with an area of ~0.1 m^2. © *2005 Pleiades Publishing, Inc.*

Methods for the deposition of fullerene films via thermal evaporation in vacuum are well known [1–3], but the use of high-energy electron beams for the evaporation of initial fullerene powders is still insufficiently studied. It would be of interest to use a characteristic feature of the action of an intense electron beam that consists in explosive spraying of the target, whereby the covalent C–C bonds in evaporated fullerene molecules can be retained. In addition, the electron-beam evaporation simplifies the coating of large-area (>1 m^2) substrates, since this method of heating can provide for an ultimately high deposited power density (>10^9 W/m^2).

This Letter describes a new method of the electron-beam evaporation of targets in vacuum, which has been specially developed for the deposition of fullerene films.

The initial C_{60}/C_{70} fullerene mixture was synthesized in a plasmachemical reactor using arc discharge at a pressure of 10^5 Pa [4, 5]. The fullerene fraction was isolated from the obtained products by extraction with benzene. The initial mixture composition was as follows (weight fraction): C_{60}, 0.8; C_{70}, 0.15; higher fullerenes, 0.04; $C_{60}O$ and $C_{70}O$ oxides, 0.01. The targets were prepared by pressing the fullerene mixture into disks with a diameter of 20 mm and a thickness of 3 mm under a pressure of ~32–34 kgf/cm^2.

An experimental setup for the pulsed evaporation of powdered fullerene mixtures is schematically depicted in Fig. 1. The setup is based on a plasma electron gun *1* [6, 7], where electrons are generated in hollow-cathode magnetron discharge plasma. The discharge is initiated and continuously power-supplied using a current source *3*. Electrons with a total current of 50 mA are accelerated by a voltage of 20 kV applied to anode *2* from a high-voltage source *4*. Then, the beam of high-energy electrons enters an electromagnetic lens *5* con-

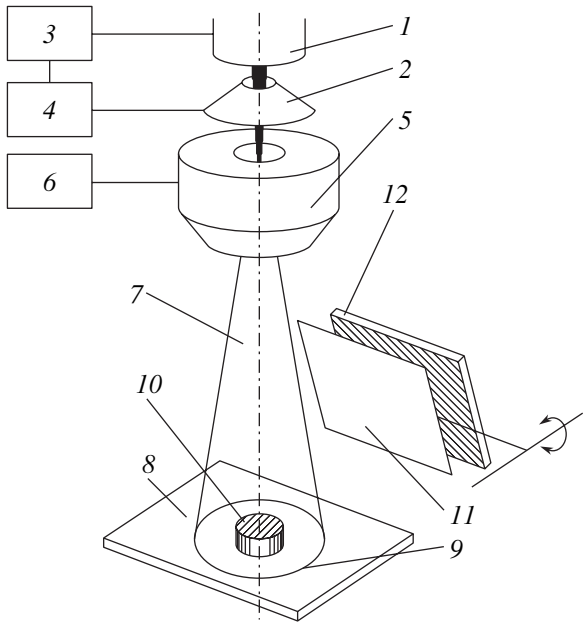

Fig. 1. Schematic diagram of the experimental arrangement: (*1*) plasma electron gun; (*2*) accelerating electrode; (*3*) discharge current source; (*4*) high-voltage source; (*5*) electromagnetic lens; (*6*) electron beam control unit; (*7*) annular electron beam; (*8*) graphite collector; (*9*) electron beam projection; (*10*) fullerene disk target; (*11*) shutter; (*12*) substrate.

1063-7850/05/3112-1036$26.00 © 2005 Pleiades Publishing, Inc.

trolled by the electron beam control unit *6* [8], which produces annular electron beam *7* at the output. The beam strikes graphite collector *8*. Initially, electrons are projected into ring *9* with an outer and inner radius of 50 and 48 mm, respectively, coaxial with disk target *10*. The lens can be controlled so as to provide for a rapid narrowing of the annular beam, whereby the ring projection of the beam on the collector surface is focused into a 3-mm spot. The electron beam power in these experiments was on the order of 10^3 W. Shutter *11* can be removed to expose substrate *12* to the flux of particles evaporated from the target. The particles are deposited onto the entire surface of substrate (amorphous glass) with dimensions 30×30 cm.

The film thickness was measured using a microinterferometer (MII-4) of the Linnik type. The films were characterized using the Raman and electronic absorption spectroscopy techniques. The Raman spectra were measured on a Bruker RFS 100/S Fourier transform spectrometer equipped with a YAG:Nd laser operating at $\lambda = 1064$ nm and a power of 10 mW. The electronic absorption spectra of fullerene solutions were recorded using an Uvicon Model 943 double-beam spectrophotometer.

The sample films were grown in a vacuum of 2×10^{-2} Pa. Initially, the electron beam *7* is focused so that its projection *9* occurs at the periphery of the disk target *10*, while shutter *11* screens substrate *12* from direct flux of evaporated carbon particles. In the zone where the electron beam strikes the graphite holder *8*, the temperature is about $\sim 1.7 \times 10^3$ K and the pressure of carbon vapor is relatively low (on the order of 10^{-8} Pa) [9]. From this initial state (Fig. 1), the annular electron beam is rapidly contracted (using lens *5* controlled by unit *6*) in the radial direction so as to approach the disk target. When the electron beam touches disk *10*, the intense evaporation of fullerenes simultaneously begins over the entire circumference of the target. At this moment, shutter *11* is removed so that particles leaving the electron-beam-heated zone can reach the surface of substrate *12* and condense to form a film (at a substrate temperature of 300 K). The annular electron beam projection is contracted to the disk center within ~1 s, which leads to instantaneous evaporation of the target material. When the beam is spot-focused at the disk center and the target is completely evaporated, shutter *11* is returned in the initial position.

The film deposited on the substrate in the course of explosive evaporation of the fullerene mixture was 1–2 μm thick and had a brown color. The film covered the entire substrate surface with an area of ~0.1 m^2. The X-ray diffraction measurements showed the films formed on the substrate at 300 K to be X-ray amorphous. However, the films obtained by deposition onto a substrate heated to 393 K, followed by annealing for 0.5 h at 373 K in vacuum, exhibited a crystalline structure.

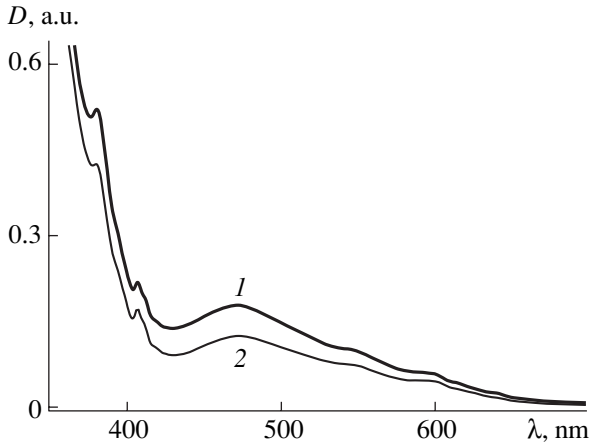

Fig. 2. Electronic absorption spectra of (*1*) an electron-beam deposited fullerene film and (*2*) the initial fullerene mixture.

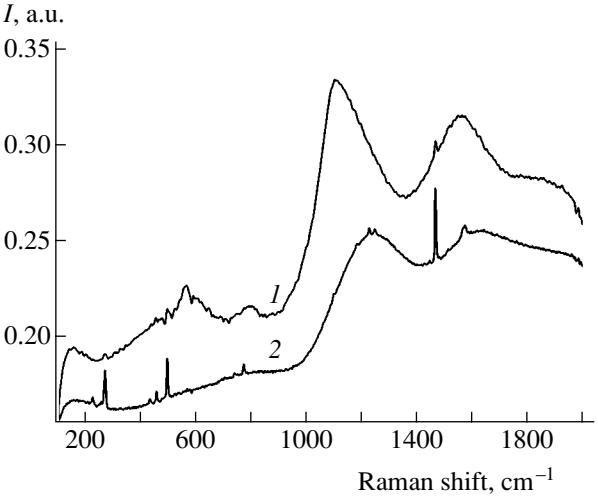

Fig. 3. Raman spectra of (*1*) an electron-beam deposited fullerene film and (*2*) the initial fullerene mixture.

The films grown as described above were soluble in nonpolar solvents. The electronic absorption spectrum of such a solution was close to that of the initial fullerene mixture (Fig. 2). This was indicative of the fact that the electron-beam evaporation of fullerenes C_{60} and C_{70} proceeds without rupture of C–C covalent bonds. However, the Raman spectrum of a deposited film displayed, besides sharp peaks corresponding to fullerenes C_{60} (495 and 1468 cm^{-1}) and C_{70} (271 cm^{-1}), some additional broad bands (Fig. 3). This result suggests that the state of fullerene molecules in the film differs from that in the initial powder. Since the film thickness is relatively small, the interaction of fullerene molecules with the substrate can be a significant factor.

In conclusion, the electron-beam-induced explosive evaporation of a fullerene mixture at temperatures above 1.7×10^3 K (significantly exceeding the sublimation temperature of fullerenes, $(7.23–7.73) \times 10^2$ K) can

be used for the deposition of fullerene films. In this study, such conditions have been provided for the first time using an annular electron beam rapidly focused into a spot. Using a plasma electron gun, electron beams with a current above 1 A and a beam power >20 kW can be generated, providing for the possibility of fullerene film deposition on the substrate surface with an area >1 m^2 due to a sufficiently large amount of evaporated material.

Acknowledgments. This study was supported by INTAS within the framework of the project no. 2001-2399.

REFERENCES

1. I. P. Soshnikov, A. V. Lunev, M. E. Gaevskii, *et al.*, Zh. Tekh. Fiz. **70** (6), 98 (2000) [Tech. Phys. **45**, 766 (2000)].
2. S. V. Kozyrev and V. V. Rotkin, Fiz. Tekh. Poluprovodn. (St. Petersburg) **27**, 1409 (1993) [Semiconductors **27**, 777 (1993)].
3. E. M. Shpilevskiĭ, L. V. Baran, and M. E. Shpilevskiĭ, Mater. Tekhnol. Instrum. **3** (2), 105 (1998).
4. G. N. Churilov, A. S. Fedorov, and P. V. Novikov, Pis'ma Zh. Éksp. Teor. Fiz. **76**, 604 (2002) [JETP Lett. **76**, 522 (2002)].
5. G. N. Churilov, Prib. Tekh. Éksp., No. 1, 5 (2000).
6. A. P. Semenov and I. A. Semenova, Izv. Vyssh. Uchebn. Zaved., Fiz., No. 9, 69 (2001).
7. A. P. Semenov and I. A. Semenova, Zh. Tekh. Fiz. **75** (4), 48 (2005) [Tech. Phys. **50**, 434 (2005)].
8. Yu. V. Grigor'ev, Yu. G. Petrov, and V. I. Pozdnov, Prib. Tekh. Éksp., No. 2, 236 (1990).
9. A. I. Pipko, V. Ya. Pliskovskiĭ, and E. A. Penchko, *Pumping Equipment for Vacuum Devices* (Énergiya, Moscow, 1965) [in Russian].

Translated by P. Pozdeev

Technical Physics Letters, Vol. 31, No. 12, 2005, pp. 1039–1042. Translated from Pis'ma v Zhurnal Tekhnicheskoĭ Fiziki, Vol. 31, No. 24, 2005, pp. 1–10.

The Surface Energy of Cryocrystals

M. N. Magomedov

Institute for Geothermal Research, Dagestan Scientific Center, Russian Academy of Sciences, Makhachkala, Dagestan, Russia

e-mail: mahmag@iwt.ru

Received May 24, 2005

Abstract—An expression for the surface energy σ_{00} of a crystal at $T = 0$ and $P = 0$ is obtained with allowance for the zero-point vibrations of atoms in the crystal. Particular calculations are performed for the cryocrystals of inert gases and hydrogen isotopes, in which the energy of zero-point vibrations is comparable with the energy of interatomic interactions. It is established that σ_{00} exhibits highly correlated dependences of the same kind on the atomic (molecular) mass m, the melting temperature T_m, and the interatomic interaction potential D/k_B (k_B is the Boltzmann constant), whereby the function $\sigma_{00}(m, T_m, D/k_B)$ exhibits nonlinear growth with each argument. The ratio $\sigma_{00}/\sigma_{liquid}$, where σ_{liquid} is the surface tension of the liquid phase at $T = T_m$, also exhibits highly correlated dependences on m, T_m, and D/k_B, which can be divided into two parts of linear growth corresponding to the quantum and classical domains. The $\sigma_{00}/\sigma_{liquid}$ ratio, being smaller in the quantum case than in the classical one, grows with m, T_m, and D/k_B much faster in the quantum than in the classical domain. © *2005 Pleiades Publishing, Inc.*

Theoretical investigation into the surface properties of cryocrystals encounters considerable problems because the energy of zero-point vibrations of atoms in such systems is comparable with the energy of atomic attraction (even with that in the liquid phase) and the characteristic frequency of lattice vibrations exhibits significant dependence on the temperature [1]. At the same time, experimental evaluation of the surface energy of crystals at temperatures close to the absolute zero is also an extremely complicated task. In this context, the present study was devoted to estimation of the surface energy of a cryocrystal with allowance for the energy of zero-point vibrations.

Let atoms in the crystal interact as described by the pair potential of the Mie–Lennard-Jones type [1–3]:

$$\varphi(r) = [D/(b-a)] \times \{a[r_0/(c+r)]^b - b[r_0/(c+r)]^a\}, \quad (1)$$

where D and r_0 are the depth and coordinate of the potential well minimum, respectively; b and a are the parameters; $c = [6k_pV/\pi N_A]^{1/3}$ is the distance between the centers of nearest-neighbor atoms in the crystal lattice; k_p is the packing factor; V is the molar volume; and N_A is the Avogadro number.

Previously, an expression for the specific energy σ (per unit surface area) of a nanocrystal comprising N atoms faceted by (100) planes at an arbitrary temperature T was obtained [4] using a description of the spectrum of the crystal lattice vibrations in terms of the Einstein model within the framework of the nearest-neighbor approximation. In the case of macroscopic crystal ($N \longrightarrow \infty$), the obtained expression acquires the following form:

$$\sigma(T, V) = -(k_3/12c^2\alpha_s)\{DU(R) + 3k_B(\Theta/k_3)E(\Theta/T)[\Theta_0/(\Theta_0 + A_w\xi)]\vartheta(T/\Theta_0)\}, \quad (2)$$

where k_3 is the first coordination number in the bulk of the crystal, k_B is the Boltzmann constant, Θ_0 is the Einstein temperature at $T = 0$, and

$$U(R) = (aR^b - bR^a)/(b-a), \quad R = r_0/c; \quad \alpha_s \cong (\pi/6k_p)^{2/3}; \quad (3)$$

$$E(\Theta/T) = 0.5 + [\exp(\Theta/T) - 1]^{-1};$$

$$\vartheta(T/\Theta_0) = 1 - (T/\Theta_0)\{\partial \ln[\lambda(T/\Theta_0)]/\partial(T/\Theta_0)\}.$$

The characteristic Einstein temperature for a macrocrystal with the interatomic interaction potential (1) can be expressed as [3, 5]

$$\Theta(T) = A_w\xi\{-1 + [1 + (6D/k_BA_w\xi^2)]^{1/2}\}\lambda(T/\Theta_0).$$
$$A_w = K_R[5k_3ab(b+1)/192(b-a)]R^{b+2}, \quad (4)$$
$$K_R = \hbar^2/k_Br_0^2m, \quad \xi = 9/k_3,$$

where m is the atomic (molecular) mass, $\hbar$ is the Planck constant, and $\lambda(T/\Theta_0)$ is a function describing the tem-

1063-7850/05/3112-1039$26.00 © 2005 Pleiades Publishing, Inc.

Parameters of cryocrystals and liquid phases of inert gases and hydrogen isotopes

Crystal	m, amu	r_0, 10^{-10} m	D/k_B, K	b	a	Θ_D, K [Eq. (4)]	γ_{00} [Eq. (8)]	L_{00}, J/mol [Eq. (8)]	V_{00}, cm^3/mol [Eq. (8)]	σ_{00}, mJ/m^2 [Eq. (7)]	σ_{liquid} [6], mJ/m^2	$\sigma_{00}/\sigma_{liquid}$
Ne	20.18	3.1563	52.59	21.39	5.83	74.6	3.30	1925.9	13.39	8.03	5.519	1.455
				17.84	6.20		2.80				(25 K)	
Ar	39.95	3.7555	173.60	16.69	6.62	93.3	2.95	7787.4	22.56	20.39	13.39	1.523
				15.42	6.70		2.75				(84 K)	
Kr	83.8	3.9922	238.37	15.92	6.56	71.7	2.90	11220.6	27.095	25.33	16.29	1.555
				16.04	6.55		2.92				(116 K)	
Xe	131.29	4.3358	330.92	15.42	6.73	64.0	2.85	15909.8	34.71	30.11	18.71	1.609
				14.81	6.75		2.75				(162 K)	
p-H_2	2.016	3.791	37.53	23.57	5.21	118.5	2.47	763.6	23.207	3.24	2.95	1.098
				18.71	5.77		2.00				(14 K)	
o-D_2	4.028	3.604	44.56	19.91	6.04	114.0	2.50	1156.58	19.95	4.59	3.751	1.224
				15.53	6.43		2.00				(19 K)	
HD	3.022	3.682	41.64	21.13	5.70	116.20	2.49	990.0	21.25	4.00	3.377	1.184
				16.59	6.16		2.00				(17 K)	
HT	4.024	3.604	44.55	19.91	6.04	114.00	2.50	1156.0	19.94	4.59	3.637	1.262
				15.53	6.43		2.00				(18 K)	
DT	5.030	3.544	46.82	19.18	6.31	112.00	2.51	1287.5	18.96	5.09	4.025	1.265
				14.90	6.64		2.00				(20 K)	
T_2	6.032	3.495	48.66	18.69	6.52	110.20	2.52	1395.0	18.18	5.52	4.181	1.320
				14.47	6.82		2.00				(21 K)	

Note: Parameters of the Mie–Lennard-Jones potential (1) given in the thick solid frame were determined for the fcc crystals of inert gases and hcp crystals of hydrogen isotopes as described in [2, 3]; these parameters were used to calculate the values of the Debye temperature Θ_D, Grüneisen parameter γ_{00}, sublimation energy L_{00}, molar volume V_{00}, and specific surface energy of the (100) crystal face at $T = 0$ and $P = 0$ using formulas indicated in square brackets; for all cryocrystals $k_3 = 12$, $k_p = 0.7405$, $\xi = 0/75$, and $\alpha_s = 0.7937$; σ_{liquid} is the surface tension of the liquid phase estimated at $T = T_m$ (indicated in parentheses) and $P = 0$ [6].

perature dependence of the characteristic vibration frequency. Previously, it was established [3] that $\lambda(T/\Theta_0) = 1$ for $T = 0$ and at high temperatures ($T \gg \Theta_0$), so that significant variations of this function take place only in the interval $0 < T \ll \Theta_0$.

In the range of high temperatures, the functions E and Θ in Eqs. (3) can be approximated as $E \cong T/\Theta_0$ (for $\Theta/T < 1$) and $\vartheta \cong 1$ (for $T/\Theta_0 \gg 1$). If the energy of zero-point vibrations is smaller than the chemical binding energy, that is, when $6D \gg k_B A_w \xi^2$ (this condition is not valid for the "quantum" crystals such as He, H_2, and Ne), expression (4) yields the formula $\Theta_0 \cong (6DA_w/k_B)^{1/2}$. Then Eq. (2) gives an expression for the specific surface energy $\sigma(N = \infty)$ of a macrocrystal at zero pressure ($R = 1$) and $T = T_m$:

$$\sigma(T_m, R = 1) = (k_B/4r_0^2\alpha_s)[(k_3 D 3k_B/) - T_m]. \quad (5)$$

Previously [4] this expression was used to calculate the surface energy of the elemental macrocrystals of metals and semiconductors with various crystal structures. The results of calculations obtained for 25 macrocrystals at $T = T_m$ showed good agreement with experimental data.

It is necessary to note that relation (5) should not mislead one into concluding that the function σ at $T = 0$ is determined only by the crystal structure and the D value, while the quantum properties (including the energy of zero-point vibrations) are insignificant. This

conclusion is obviously wrong, since Eq. (2) yields for $T = 0$ the following relation:

$$\sigma(T = 0, V) = -(k_3/12c^2\alpha_s)\{DU(R) + (3/2)k_B(\Theta_0/k_3)[\Theta_0/\Theta_0 + A_w\xi]\}, \quad (6)$$

which implies that $\sigma(m)$ at $T = 0$ is determined by the contribution due to zero-point vibrations and, hence, is very weak for non-quantum substances (such as, e.g., metals).

For a cryocrystal, in which the energy of zero-point vibrations at $T = 0$ and $P = 0$ (i.e., at $c = r_0$) is comparable with the interatomic interaction energy D, Eq. (6) gives the following formula for the specific surface energy of the (100) crystal face:

$$\sigma_{00} = (1/c^2\alpha_s) \times \{k_3D/12) - [3k_B\Theta_D^2/32(\Theta_D + (3/4)A_w\xi)]\}, \quad (7)$$

where $\Theta_D = (4/3)\Theta_0(R = 1)$ is the Debye temperature of the macrocrystal at $T = 0$ and $P = 0$.

The values of the Debye temperature Θ_D, Grüneisen parameter γ_{00}, sublimation energy L_{00}, molar volume V_{00}, and specific surface energy σ_{00} of the (100) crystal face at $T = 0$ and $P = 0$ calculated for the crystals of inert gases and hydrogen isotopes are presented in the table. These calculations were performed using Eqs. (3), (7), and the expressions obtained previously [2, 3, 5]:

$$\gamma_{00} = [(b + 2)/6][1 + (4A_w\xi/3\Theta_D)]^{-1}, \quad L_{00}/N_A = (k_3/2)D - (9/8)k_B\Theta_D, \quad V_{00} = \pi N_A r_0^3/6k_p. \quad (8)$$

The results of calculations for the cryocrystals, in which the energy of zero-point vibrations is comparable with the energy of interatomic interactions, are in good agreement with the experimental estimates available for Θ_D, γ_{00}, L_{00}, and V_{00} [1]. Unfortunately, no experimental data on σ_{00} for the cryocrystals under consideration have been reported thus far. For this reason, the calculated values of σ_{00} are compared to experimental values of the surface tension σ_{liquid} of the corresponding liquid phases at $T = T_m$ and $P = 0$ [6]. As can be seen from the table, the $\sigma_{00}/\sigma_{liquid}$ ratio exhibits monotonic growth both for hydrogen isotopes (from 1.098 in p-H_2 to 1.32 in T_2) and for inert gases (from 1.455 in Ne to 1.609 in Xe). This behavior is consistent with that observed for the macrocrystals of elemental metals and semiconductors [7], where the $\sigma_{solid}/\sigma_{liquid}$ ratio was found to grow with an increase in the melting temperature T_m. For the metals and semiconductors, the $\sigma_{solid}/\sigma_{liquid}$ ratio varies from 1.1 to 1.7 [7], in agreement with the interval of variation of the $\sigma_{00}/\sigma_{liquid}$ ratio in the table.

An analysis of data presented in the table leads to the following conclusions:

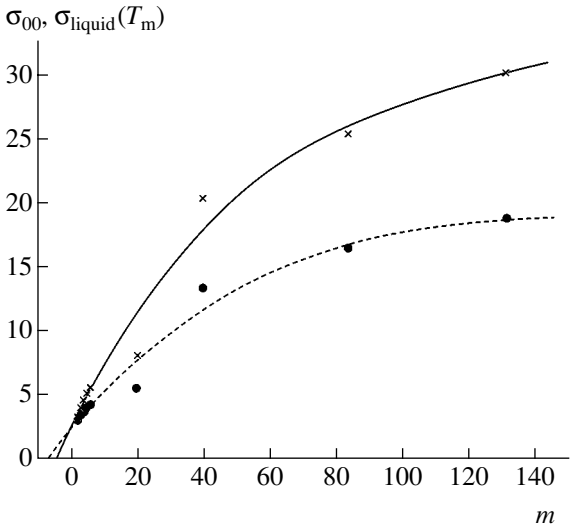

Fig. 1. Plots of σ_{00} (crosses) and σ_{liquid} (circles) versus atomic (molecular) mass for substances presented in the table. Solid curve shows the approximation of data for cryocrystals by the cubic polynomial $\sigma_{00} = 2.26497 + 0.51855m - 0.00363m^2 + 9.78294 \times 10^{-6}m^3$ (correlation coefficient $R_{corr} = 0.98011$); dashed curve shows the approximation of data for liquid phases [6] by the cubic polynomial $\sigma_{liquid} = 2.32118 + 0.30425m - 0.00194m^2 + 4.2996 \times 10^{-6}m^3$ ($R_{corr} = 0.97529$). The two curves intersect at $m \cong 0.335$ amu, $\sigma \cong 2.4$ mJ/m^2.

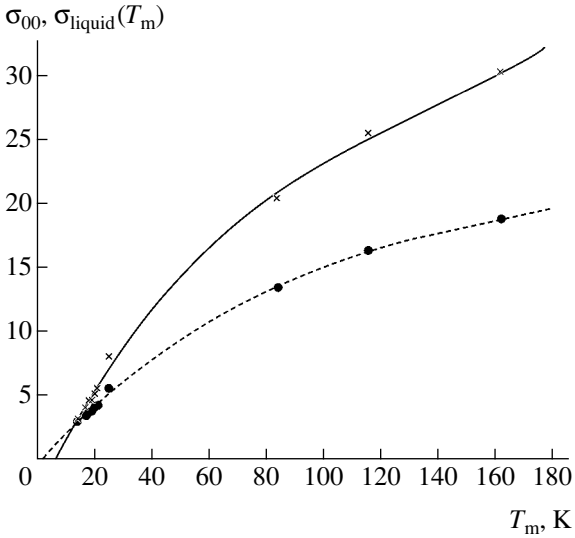

Fig. 2. Plots of σ_{00} (crosses) and σ_{liquid} (circles) versus melting temperature for substances presented in the table. Solid curve shows the approximation of data for cryocrystals by the cubic polynomial $\sigma_{00} = -2.64663 + 0.44535T_m - 0.0025T_m^2 + 6.16023 \times 10^{-6}T_m^3$ ($R_{corr} = 0.99833$); dashed curve shows the approximation of data for liquid phases [6] by the cubic polynomial $\sigma_{liquid} = -0.401 + 0.247T_m - 0.00115T_m^2 + 2.18598 \times 10^{-6}T_m^3$ ($R_{corr} = 0.99918$). The two curves intersect at $T_m \cong 12$ K, $\sigma \cong 2.4$ mJ/m^2.

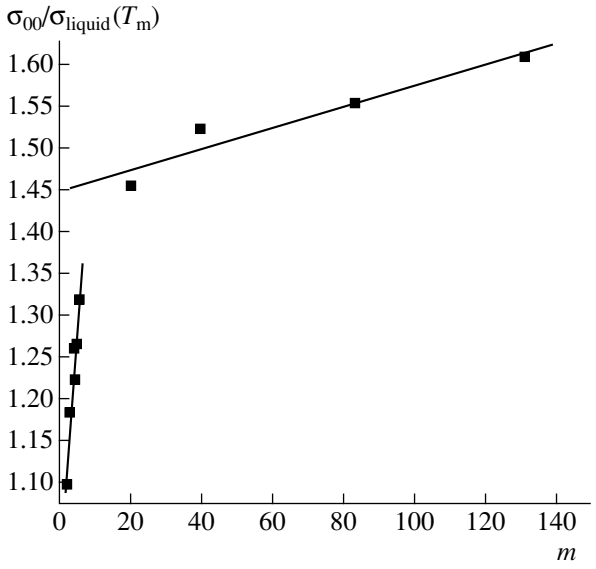

Fig. 3. Plot of $\sigma_{00}/\sigma_{liquid}$ versus atomic (molecular) mass for substances presented in the table. Solid lines show the approximation of data by the linear functions $\sigma_{00}/\sigma_{liquid} = 1.01502 + 0.05229m$ for $m \le m_{T_2} = 6.032$ amu ($R_{corr} = 0.96165$) and $\sigma_{00}/\sigma_{liquid} = 1.44947 + 0.00125m$ for $m \ge m_{Ne} = 20.18$ amu ($R_{corr} = 0.96165$).

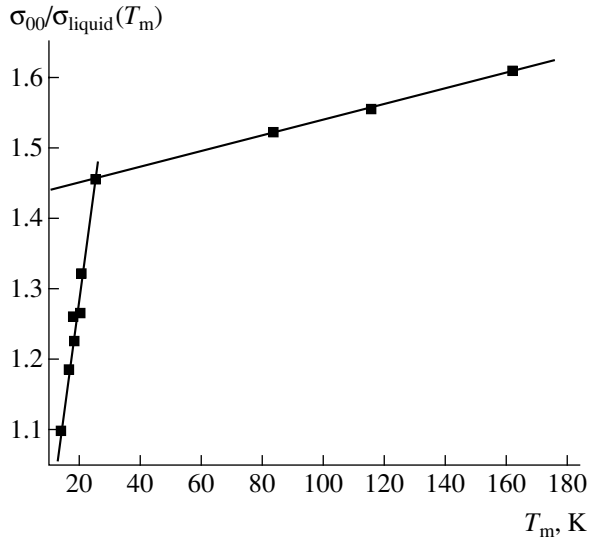

Fig. 4. Plot of $\sigma_{00}/\sigma_{liquid}$ versus melting temperature for substances presented in the table. Solid lines show the approximation of data by the linear functions $\sigma_{00}/\sigma_{liquid} = 0.64861 + 0.03185T_m$ for $T_m \le T_m(Ne) = 25$ K ($R_{corr} = 0.97927$) and $\sigma_{00}/\sigma_{liquid} = 1.42738 + 0.00112T_m$ for $T_m \ge T_m(Ne) = 25$ K ($R_{corr} = 0.9997$).

(i) The values of σ_{00} calculated for cryocrystals as described above, as well as the corresponding σ_{liquid} values reported in [6], exhibit strongly correlated dependences on m (Fig. 1), T_m (Fig. 2), and D/k_B. Plotted as functions of m, T_m, and D/k_B, both σ_{00} and σ_{liquid} values show nonlinear increase with these arguments.

(ii) All three plots of σ_{00} and σ_{liquid} versus m, T_m, and D/k_B for cryocrystals exhibit an intersection of the approximating cubic curves at the same value of the specific surface energy: $\sigma \cong 2.4$ mJ/m^2 at $m \cong 0.335$ amu (Fig. 1), $T_m \cong 12$ K (Fig. 2), and $D/k_B \cong 33$ K. This behavior indicates that the difference between the corresponding solid and liquid phases decreases with an increasing "quantum character" of the substance and disappears at a certain value of the atomic mass (in this case, at $m \le 0.335$ amu).

(iii) The value of $\sigma_{00}/\sigma_{liquid}$, which is the ratio of the calculated surface energy at $T = 0$ and $P = 0$ to the surface tension of the corresponding liquid phase at $T = T_m$ and $P = 0$, also exhibits strongly correlated dependences on m (Fig. 3), T_m (Fig. 4), and D/k_B.

(iv) The dependence of the $\sigma_{00}/\sigma_{liquid}$ ratio on m, T_m, and D/k_B for cryocrystals can be divided into two parts of linear growth corresponding to the quantum ($m \le m_{T_2} = 6.032$ amu) and classical ($m \ge m_{Ne} = 20.18$ amu) domains (Figs. 3 and 4). The $\sigma_{00}/\sigma_{liquid}$ ratio is smaller in the quantum case than in the classical one, but this value grows with m, T_m, and D/k_B much faster in the quantum than in the classical domain.

(v) The values of σ_{00} and σ_{liquid}, as well as the $\sigma_{00}/\sigma_{liquid}$ ratio, monotonically increase with the isotope mass (see table). This dependence of $\sigma(m)$ is inherent in both quantum and classical crystals. The reasons for such behavior have recently been considered in detail for carbon (diamond) and lithium crystals [8].

Acknowledgments. The author is grateful to A.D. Filenko, K.N. Magomedov, and Z.M. Surkhaeva for their help in this work.

This study was supported by the Russian Academy of Sciences (OEMMPU project no. 7/067-095/05.05.04-229).

REFERENCES

1. *Cryocrystals*, Ed. by B. I. Verkin and A. F. Prikhod'ko (Naukova Dumka, Kiev, 1983) [in Russian].
2. M. N. Magomedov, Zh. Fiz. Khim. **62**, 2103 (1988).
3. M. N. Magomedov, Fiz. Tverd. Tela (St. Petersburg) **45**, 33 (2003) [Phys. Solid State **45**, 32 (2003)].
4. M. N. Magomedov, Fiz. Tverd. Tela (St. Petersburg) **46**, 924 (2004) [Phys. Solid State **46**, 954 (2004)].
5. M. N. Magomedov, Zh. Fiz. Khim. **61**, 1003 (1987).
6. V. G. Baĭdakov, "Surface Tension of Liquefied Gases," in *Reviews of Thermophysical Properties of Materials* (IVTAN, Moscow, 1988), No. 1(69), pp. 3–112 [in Russian].
7. U. M. Kulish, *Physical Chemistry of Surface Phenomena in Melts* (Naukova Dumka, Kiev, 1971), pp. 46–51 [in Russian].
8. M. N. Magomedov, Pis'ma Zh. Tekh. Fiz. **31** (9), 50 (2005) [Tech. Phys. Lett. **31**, 381 (2005)].

Translated by P. Pozdeev

Technical Physics Letters, Vol. 31, No. 12, 2005, pp. 1043–1046. Translated from Pis'ma v Zhurnal Tekhnicheskoĭ Fiziki, Vol. 31, No. 24, 2005, pp. 11–19.

Mechanism of *p–n* Junction Breakdown at High Reverse Voltage Ramps

A. S. Kyuregyan

All-Russia Electrical Engineering Institute, Moscow, Russia

e-mail: ask@vei.ru

Received July 12, 2005

Abstract—It is shown that flat tunneling-assisted impact ionization fronts in *p–n* junctions operating at a high buildup rate (ramp) u of the reverse voltage can be obtained provided that the rate g_f of the tunneling generation of electron–hole pairs is much greater than the impact ionization rate g_i in the initial stage of breakdown. Usually (e.g., in silicon) $g_f \ll g_i$ and, therefore, the multiplication of the first hundreds of electron–hole pairs due to the impact ionization leads to the avalanche–streamer transition much before the overlap of avalanches. In this case, the diode transition to the conducting state may be caused by the interelectrode gap shortage by a large number of streamers, the total resistance of which can be much smaller than the load resistance. A simple model of such a "multistreamer" breakdown is proposed according to which the switching time is virtually independent of the streamer parameters and is inversely proportional to u. The diode resistance in the conducting state significantly drops with increasing ramp u and grows with increasing velocity of streamers. © *2005 Pleiades Publishing, Inc.*

Recently, Rodin *et al.* [1] described a mechanism of the *p–n* junction breakdown at a high buildup rate (ramp) u of the reverse voltage, which was based on the notion of a flat tunneling-assisted impact ionization front that forms and propagates in the space charge region (SCR). The proposed mechanism was used to interpret the results of experiments with silicon diode triggering at $u \simeq 10^{13}$ V/s [2]. According to [1], this mechanism can be operative (e.g., in p^+–n–n^+ diodes) provided that

(i) a diode is preliminarily biased in the reverse direction with a voltage U_0, which is lower than the static breakdown voltage U_b but higher than the voltage $qNd^2/2\varepsilon$ corresponding to the contact between the SCR and n^+ layer (here, q is the elementary charge, N is the donor concentration in the n layer, d is the n layer thickness, and ε is the permittivity of the semiconductor);

(ii) the leakage current density j_T is so small that the average charge carrier number in the SCR is $N_T = j_T Sd/qv_s \le 1$ (S is the diode area and v_s is the saturated drift velocity);

(iii) a reverse voltage pulse with a front width below d/v_s and an amplitude of ~(3–4)U_b is applied to the diode in addition to the constant bias.

Under such conditions, free charge carriers are either absent from the SCR or form on the average a single low-conducting channel that is incapable of preventing the rapid voltage buildup on the diode. As a result, the maximum field strength E_M significantly exceeds the static breakdown value $E_b \approx 0.2$ MV/cm, and the tunneling generation of electron–hole pairs begins in the region of the maximum field. These pairs exhibit intense multiplication that generates the dense electron-hole plasma, which drives the field toward the n^+ layer. According to [1], this mechanism gives rise to a rapidly propagating front that separates the dense plasma from a depleted region occupied by the strong field. This process was simulated [1, 2] within the framework of a one-dimensional continuous approximation, which is justified provided that the electron and hole densities in the dense plasma regions are n, $p \gg \lambda^{-3}$, where λ is the characteristic size of such regions. Otherwise, it is necessary to take into account the discrete nature of charges and the stochastic character of electron–hole pair generation. It has been pointed out [1] that, in the problem under consideration, this factor is especially important in the initial stage of front generation, whereby the number of pairs formed in the SCR within a finite time is already large, but still n, $p \ll \lambda^{-3}$, the continuous approximation is inapplicable, and the corresponding solutions have no physical meaning. In order to eliminate such solutions, it has been proposed [1] to "switch off" the impact ionization during simulation of the process, unless the tunneling generation of electron–hole pairs would provide for the condition $n, p \gg d^{-3} \sim 10^9$ cm^{-3}. However, the author believes that this approach cannot be justified (without additional assumptions) for two reasons. First, the problem under consideration has at least two other characteristic dimensions—namely, the wave front width and the electron avalanche radius—which are much smaller than d. Second, the artificial "switch-off"

1063-7850/05/3112-1043$26.00

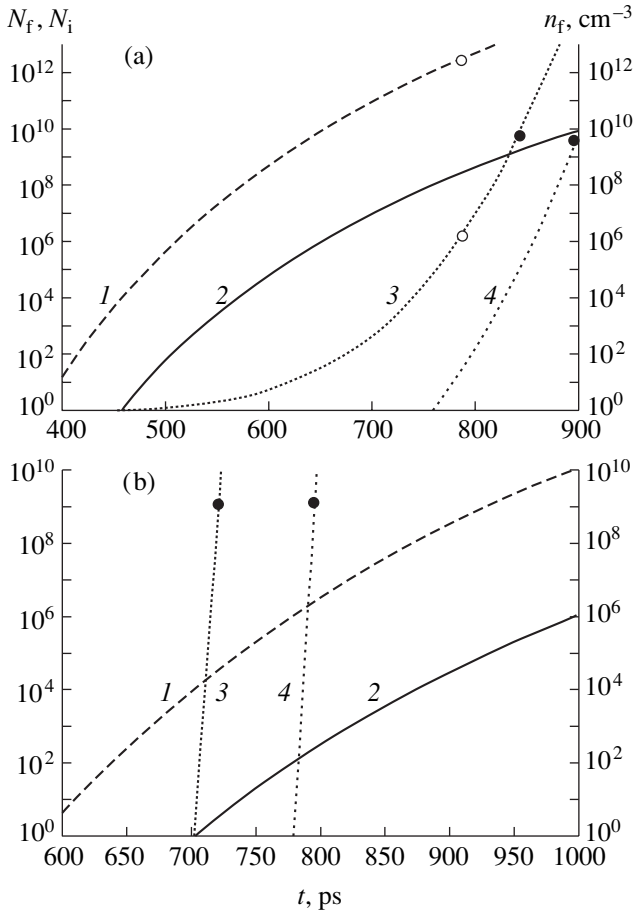

Fig 1. Time variation of (*1*) the total number N_f and (*2*) the density n_f of electron–hole pairs generated due to tunneling in the SCR and (*3*, *4*) the total number N_i of electrons in avalanches that started at the moments when the average N_f values reached (*3*) 1 and (*4*) 10^8 (a) or 10^2 (b). The black circles indicate the moments of time and the N_i values at which the space-charge field of isolated avalanches becomes equal to the external field; the open circles indicate the moments of time and the n_f and N_f values at which the avalanche volume becomes equal to the SCR volume.

of the impact ionization in the numerical solution by no means implies that this factor would not be significant in the electric fields ~1 MV/cm for which the tunneling generation of pairs becomes significant.

In order to elucidate this question, let us consider, for simplicity, a p^+–i–n^+ diode meeting the conditions formulated above. As soon as the reverse bias exceeds the level of ~(3–4)U_b, the tunneling generation of electron–hole pairs will begin in the SCR at a rate of

$$g_f = \tilde{g}_f \exp[-E_f/E(t)], \quad (1)$$

where $E(t) = (U_0 + ut)/d$ is the field strength and $\tilde{g}_f$ and E_f are the material parameters. Integrating $g_f(t)$ with respect to time t, we determine the total number of electron–hole pairs $N_f(t)$ generated in the SCR as a result of tunneling. Electrons and holes generated in this way begin to drift with the velocities $v_{e,h}$ and exhibit multiplication due to the impact ionization at a rate of $g_i = (v_e\alpha_e n + v_h\alpha_h p)$, where $\alpha_{e,h} = \tilde{\alpha}_{e,h} \exp[-E_{e,h}/E(t)]$ are the coefficients of impact ionization and $\tilde{\alpha}_{e,h}$ and $E_{e,h}$ are the material parameters.

For an avalanche arising at the time $t = t_0$, the total number of electrons and holes is

$$N_i(t_0, t) = \exp\left\{\int_{t_0}^{t} [v_e\alpha_e(t') + v_h\alpha_h(t')]dt'\right\}. \quad (2)$$

In the course of evolution, the electron avalanches exhibit "spreading" (in particular, because of diffusion), so that the characteristic avalanche radius is not smaller than $r_{av} \sim \sqrt{D(t-t_0)}$ and the intrinsic space charge field is $E_{av} \sim qN_i/4\pi\varepsilon r_{av}^2$. Now it will be demonstrated that the breakdown can develop according to one of the two possible scenarios, depending on the ratio of the tunneling rate to the impact ionization rate. Let us consider two p^+–i–n^+ diodes, referred to as variants A and B, which have the same values of $\varepsilon = 1.06 \times 10^{-12}$ F/cm, $v_e = 10^7$ cm/s, $D = 20$ cm^2/s, $S = 0.01$ cm^2, and $d = 100$ μm and different parameters of the electron–hole pair generation (see table). Figures 1a and 1b show the results of calculations performed for variants A and B, respectively, at a reverse voltage ramp of $u = 10^{13}$ V/s.

Parameters of p^+–n–n^+ diodes

Variant	$\tilde{\alpha}_e$, cm^{-1}	$\tilde{\alpha}_h$, cm^{-1}	E_e, MV/cm	E_h, MV/cm	$\tilde{g}_f$, 1/(cm^3 s)	E_f, MV/cm
A	5×10^5		4.0		10^{34}	20.0
B	6.3×10^5	1.74×10^6	1.23	2.18	10^{34}	31.0

As can be seen for variant A, the rate v_f of the tunneling generation of electron–hole pairs significantly exceeds the ionization rate g_i in the initial stage of breakdown. For this reason, the avalanche density in the SCR reaches 3×10^{12} cm^{-3} and their total volume $\pi D(t - t_0)^2(v_e + v_h)N_f$ exceeds Sd before the moment the avalanche field E_{av} becomes equal to the external field $E(t)$. In this case, the avalanches completely overlap and the continuous approximation is justified. This conclusion is confirmed by the results of numerical simulation of the breakdown development in variant A performed using a program described in [3]: the p^+–i–n^+ diode with a 50-Ω serial load was triggered in the same manner both without and with "switch-off" of the impact ionization for $n < 10^9$ cm^{-3}.

A substantially different scenario of breakdown development is realized in the case of a more realistic variant B with the parameters (see table) corresponding to experimental data for silicon [4, 5]. Here, the impact ionization rate g_i always exceeds g_f and is so large that $E_{av} \sim E(t)$ already at $t_{av} = 15$–20 ps. For this reason, the multiplication of even the 100th pair generated by tunneling (Fig. 1b, curve *4*) must lead to the avalanche–streamer transition, whereby the average distance between avalanches is still greater than or comparable with d, and the continuous approximation is by no means applicable to the simulation of the whole device. According to the available experimental results [6, 7] and theoretical estimates [8, 9], the streamer is a channel filled by electron–hole plasma, which has a linear resistance of $\rho_{st} \sim 10^4$–10^6 Ω/cm and propagates (elongates) at a velocity of $v_{st} \sim 3 \times 10^7$–$3 \times 10^9$ cm/s. If the number of streamers in the SCR is large, they can interact with each other in two ways. First, via direct distortion of the SCR field; this interaction exponentially decays with a characteristic distance on the order of d and is manifested when the density of streamers is greater than or comparable with d^{-2}. Second, via an external circuit: an increase in the diode current in the course of streamer propagation (displacement current) and, mainly, upon the interelectrode gap shortage by the streamer leads to a decrease in the diode voltage U and the field strength in the SCR. This leads to a decrease in the velocity of other streamers, which is proportional (at small lengths) to the external field strength (or the applied voltage) [8, 9]. However, this decrease in U even more significantly influences the rate of streamer generation. Indeed, both g_f and g_i strongly (exponentially) depend on the applied field and, hence, the generation of new avalanches and streamers is completely suppressed even at a relatively small decrease in U. For this reason, in describing the breakdown dynamics to the first approximation, it is sufficient to take into account only this main effect. Then, for the average diode voltage U and the diode resistance R_{st}, we obtain a simple integrodifferential equation,

$$RC\frac{dU(t)}{dt} + \left[1 + \frac{R}{R_{st}(t)}\right]U(t) = ut, \qquad (3)$$

where R is the serial load resistance,

$$R_{st}^{-1}(t) \simeq \frac{N_f(t-\tau)}{\rho_{st} d} = \frac{\tilde{g}_f S}{\rho_{st}} \int_0^{t-\tau} \exp[-E_f d/U(t')]dt', \quad (4)$$

and $\tau \approx (t_{av} + d/v_{st})$ is the delay time between the electron–hole pair production and the moment of interelectrode gap shortage by the streamer. In accordance with the above considerations, we assume the ρ_{st} and τ values in formula (4) to be constant. In addition, we neglect small displacement currents caused by the streamer elongation, and we admit that the avalanche-streamer transition unavoidably takes place in the fields featuring significant tunneling generation of pairs.

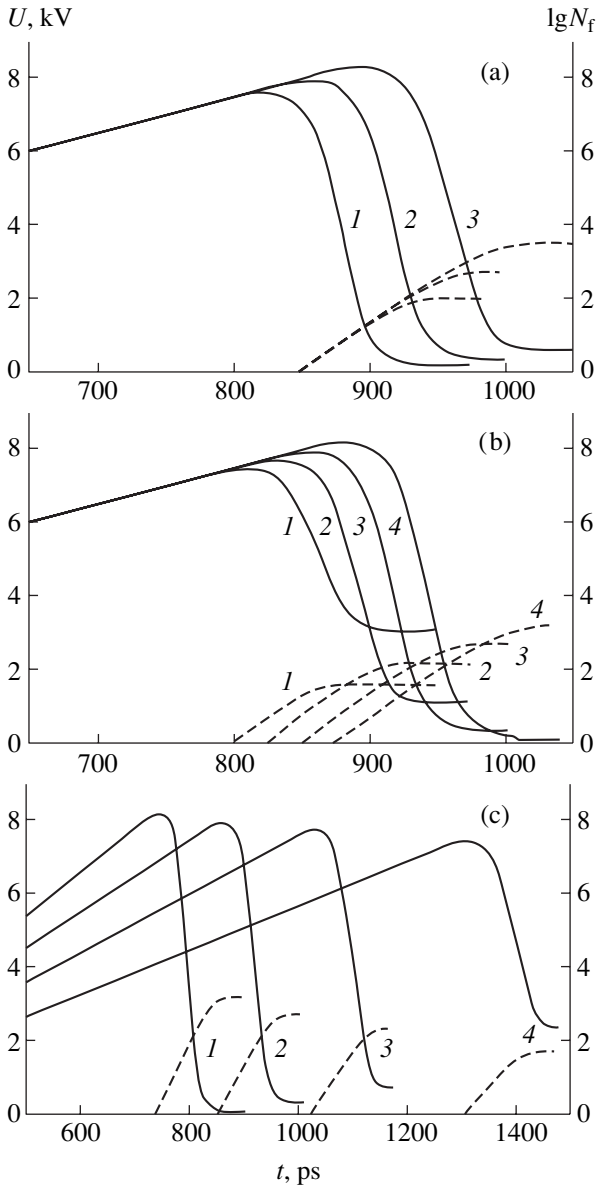

Fig. 2. Time variation of the diode voltage U (solid curves) and the number of streamers N_f (dashed curves) during multistreamer breakdown in a p^+–n–n^+ diode with the parameters of variant B and a serial load resistance of $R = 50$ Ω: (a) $u = 10^{13}$ V/s, $\tau = 100$ ps, $\rho_{st} = 10^4$ (*1*), 10^5 (*2*), and 10^6 Ω/cm (*3*); (b) $u = 10^{13}$ V/s, $\rho_{st} = 10^5$ Ω/cm, $\tau = 50$ (*1*), 75 (*2*), 100 (*3*), and 125 ps (*4*); (c) $\rho_{st} = 10^5$ Ω/cm, $\tau = 100$ ps, $u = 12$ (*1*), 10 (*2*), 8 (*3*), and 6 kV/ns (*4*).

Figure 2 shows the results of the numerical solution of Eq. (3) for a diode with the parameters corresponding to variant B with $R = 50$ Ω and various values of ρ_{st}, τ, and u. As can be seen, the appearance of a large num-

ber of streamers in the SCR of an overbiased diode can result in a fast switching to the conducting stage. This "multistreamer" breakdown has two specific features. First, the switching time t_{on} and the maximum diode voltage U_M are very weakly dependent on the streamer parameters τ (and, hence, v_{st}) and ρ_{st}. The main factor determining t_{on} and U_M is the rate of the tunneling generation of new electron–hole pairs in the SCR. In particular, t_{on} in the first approximation is equal to the time for which N_f changes from $0.1\rho_{st}d/R$ to $10\rho_{st}d/R$ (or to a maximum value N_f^M, if $N_f^M < 10\rho_{st}d/R$). Therefore, t_{on} must exhibit a slow (logarithmic) decrease with decreasing τ and ρ_{st}. At the same time, for the pair generation rate $g_f(E)$ described by Eq. (1), the switching time must obey (with a logarithmic accuracy) the relation $t_{on} \simeq 4U_M^2/uE_fd$ that is consistent with the data presented in Fig. 2c. The second specific feature is that the diode voltage U_{min} in the conducting state strongly depends both on the regime (i.e., on u) and on the streamer parameters (τ, ρ_{st}). This behavior is quite evident, since the diode resistance upon breakdown is $R_{on}^{-1} = N_f^M/\rho_{st}d$, where N_f^M rapidly grows with increasing u and τ.

It should be noted that the very idea of the possible "multistreamer" breakdown in *p–n* junctions at high voltage ramps u is by no means a new one. To the author's knowledge, this idea was formulated by Vainshtein *et al.* [10] in interpretation of the results of experiments involving the breakdown in GaAs diodes at u/d up to 2.4×10^{15} V/(cm s), which showed evidence of a strong localization of the breakdown current in several tens of channels formed in the peripheral region of diodes. However, no quantitative analysis of this possible mechanism was undertaken in [10], while qualitative considerations led the authors to conclusions substantially different from those obtained above.[1]

Acknowledgments. The author is grateful to A.V. Gorbatyuk for numerous fruitful discussions of the problems related to this study.

REFERENCES

1. P. Rodin, U. Ebert, W. Hundsdorfer, and I. Grekhov, J. Appl. Phys. **92**, 958 (2002).
2. S. K. Lyubutin, S. N. Rukin, B. G. Slovikovsky, and S. N. Tsyranov, Pis'ma Zh. Tekh. Fiz. **31** (5), 36 (2005) [Tech. Phys. Lett. **31**, 196 (2005)].
3. T. T. Mnatsakanov, I. L. Rostovtsev, and N. I. Philatov, Solid-State Electron. **30**, 579 (1987).
4. A. S. Kyuregyan and S. N. Yurkov, Fiz. Tekh. Poluprovodn. (Leningrad) **23**, 1819 (1989) [Sov. Phys. Semicond. **23**, 1126 (1989)].
5. M. S. Tyagi, Solid-State Electron. **11**, 99 (1968).
6. N. G. Basov, A. G. Molchanov, A. S. Nasibov, *et al.*, Zh. Éksp. Teor. Fiz. **70**, 1751 (1976) [Sov. Phys. JETP **43**, 912 (1976)].
7. V. P. Gribkovskiĭ, Zh. Prikl. Spektrosk. **15**, 709 (1984).
8. M. I. D'yakonov and V. Yu. Kachorovskiĭ, Zh. Éksp. Teor. Fiz. **94**, 321 (1988) [Sov. Phys. JETP **67**, 1049 (1988)].
9. M. I. D'yakonov and V. Yu. Kachorovskiĭ, Zh. Éksp. Teor. Fiz. **95**, 1850 (1989) [Sov. Phys. JETP **68**, 1070 (1989)].
10. S. N. Vaĭnshteĭn, Yu. V. Zhilyaev, and M. E. Levinshteĭn, Pis'ma Zh. Tekh. Fiz. **14** (16), 1527 (1988) [Sov. Tech. Phys. Lett. **14**, 664 (1988)].

Translated by P. Pozdeev

[1] In particular, it was believed in [10] that $t_{on} \sim d/v_{st}$ and the "nucleation of filaments" was assumed to be determined by impact ionization, rather than by tunneling.

Technical Physics Letters, Vol. 31, No. 12, 2005, pp. 1047–1048. Translated from Pis'ma v Zhurnal Tekhnicheskoĭ Fiziki, Vol. 31, No. 24, 2005, pp. 20–23.

Generation of Femtosecond Current Pulses Using the Inverse Magneto-Optical Faraday Effect

V. V. Kruglyak and M. E. Portnoi

School of Physics, University of Exeter, Exeter EX4 4QL, United Kingdom

e-mail: V.V.Kruglyak@exeter.ac.uk; M.E.Portnoi@exeter.ac.uk

Received July 27, 2005

Abstract—A new method of generating ultrashort current pulses is proposed that is based on the optical pumping of a mesoscopic structure comprising a metal ring with a core made of a material possessing giant magneto-optical susceptibility. The main dynamic characteristics of the proposed device are calculated. © *2005 Pleiades Publishing, Inc.*

Further progress in the field of information storage media with increased density of recording requires the creation of devices capable of ultrafast data manipulation. The operation speed of such devices is determined by the duration of pulses of the applied magnetic and electric fields (i.e., of the current and voltage) inducing, for example, the magnetization reversal in magnetic nanoelements. A promising basis is provided by ultrafast lasers producing pulses with widths on the order of several tens of femtoseconds [1], but this approach is limited by the response of elements converting optical energy into electricity.

This Letter describes the design and estimates the dynamic characteristics of an ultrafast photodetector capable of converting short light pulses into electric current pulses of practically the same width.

Recently, Kimel *et al.* [2] studied the optical orientation of spins by means of the inverse Faraday effect and showed that a circularly polarized light pulse with a width of 200 fs induced magnetic field pulses of the same width and an amplitude on the order of several teslas in a dysprosium orthoferrite ($DyFeO_3$) crystal. Our idea consists in that, according to the law of electromagnetic induction, such short magnetic field pulses must generate an intense vortex electric field and, hence, induce an emf in a conductor occurring in this field.

Indeed, let us perform a simple calculation. Assume that the magnetic field B is optically induced in a dysprosium orthoferrite crystal and varies in time, following the light pulse intensity as described by the Gauss function:

$$B(t) = B_0 \exp\left(-\frac{t^2}{2\sigma^2}\right), \tag{1}$$

where t is the time, B_0 is the magnetic field amplitude, and $2\sigma\sqrt{\ln 2}$ is the pulse full width at half maximum (FWHM). Owing to the continuity of the magnetic induction component normal to the crystal surface, and due to a negligibly small spontaneous magnetization of the crystal (about 8 G for $DyFeO_3$), the field intensity in a conducting ring on the crystal surface will be virtually the same as that inside the ring. The resulting emf $\varepsilon(t)$ induced in the ring is equal to the time derivative of a magnetic flux through the ring surface:

$$\varepsilon(t) = \frac{\varepsilon_0 t}{\sigma}\exp\left(-\frac{t^2}{2\sigma^2}\right), \tag{2}$$

where $\varepsilon_0 = B_0 S/\sigma$ and S is the surface area.

Considering the ring as a serial circuit with resistance R, inductance L, and emf given by Eq. (2), we readily obtain an expression for the current pulse in this circuit:

$$I(t) = -\frac{B_0 S}{L}\left\{\exp\left(-\frac{t^2}{2\sigma^2}\right) - \frac{\sigma\sqrt{\pi}}{\tau}\left[1 + \mathrm{erf}\left(\frac{t}{\sigma\sqrt{2}} - \frac{\sigma}{\tau\sqrt{2}}\right)\right]\exp\left(\frac{\sigma^2}{2\tau^2} - \frac{t}{\tau}\right)\right\}, \tag{3}$$

where $\tau = L/R$ is the relaxation time. For the ring representing a toroid with the median radius r_1 and the cross section radius r_2, the resistance and inductance can be determined as [3]

$$R = \frac{2\rho r_1}{r_2^2}, \qquad L = \mu_0 r_1\left(\ln\frac{8r_1}{r_2} - \frac{7}{4}\right), \tag{4}$$

where μ_0 is the permeability of vacuum and ρ is the resistivity of the conductor. The current profiles calcu-

1063-7850/05/3112-1047$26.00

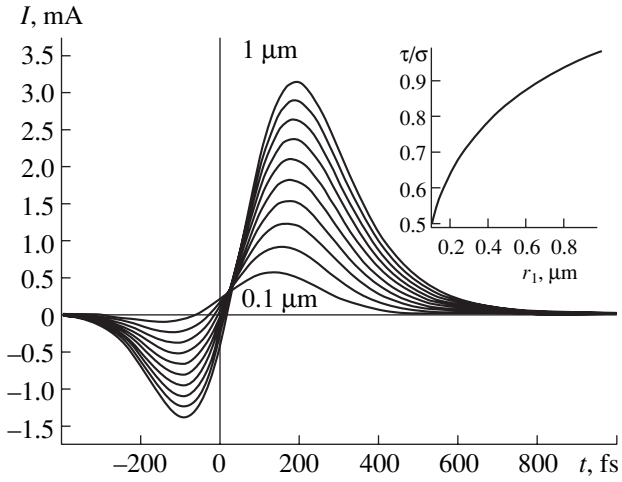

Time variation of the optically induced current I in a gold ring on the surface of a $DyFeO_3$ crystal. The calculations have been performed for a toroidal ring with variable radius r_1 = 0.1–1 μm and a cross section radius of r_2 = 30 nm, in which the magnetic field pulse with an amplitude of 0.01 T is induced by a 200-fs light pulse. The inset shows the plot of τ/σ versus r_1.

lated using Eq. (3) are presented in the figure. As can be seen, the current pulse amplitude increases with the radius of the ring, while the pulse duration remains virtually unchanged.

An important feature of the proposed device is a high sensitivity to the sign of the circular polarization of light. By analogy with the spintronics, where an additional quantum degree of freedom (spin) of charge carriers is employed, the proposed device makes use of an additional optical degree of freedom: the polarization of light. Therefore, this device may be classified as belonging to the new field of so-called spin-optronics.

In conclusion, it should be noted that the proposed device, in addition to performing the direct function of an ultrafast photodetector, can be applied in many other fields of physics. For example, it can be used for generating pulsed spin currents [4, 5] and for obtaining pulsed magnetic fields in investigations into the magnetization dynamics in nanomagnets [6]. Taking into account the femtosecond duration of the generated current pulses, the proposed device can also be used a source of radiation in the terahertz range, the development of which is among the urgent tasks in modern technical physics [7, 8].

Acknowledgments. The authors are grateful to Dr. R.J. Hicken for fruitful discussions and useful critical remarks.

REFERENCES

1. E. A. Avrutin, J. H. Marsh, and E. L. Portnoi, IEE Proc.-J: Optoelectron. **147**, 251 (2000).
2. A. V. Kimel, A. Kirilyuk, P. A. Usachev, *et al.*, Nature **435**, 655 (2005).
3. L. D. Landau and E. M. Lifshits, *Course of Theoretical Physics*, Vol. 8: *Electrodynamics of Continuous Media* (Nauka, Moscow, 1982; Pergamon, New York, 1984).
4. L. Berger, Phys. Rev. B **54**, 9353 (1996).
5. J. C. Slonczewski, J. Magn. Magn. Mater. **159**, L1 (1996).
6. V. V. Kruglyak, A. Barman, R. J. Hicken, *et al.*, Phys. Rev. B **71**, 220409 (2005).
7. V. L. Malevich, Pis'ma Zh. Tekh. Fiz. **29** (3), 48 (2003) [Tech. Phys. Lett. **29**, 240 (2003)].
8. O. V. Kibis and M. E. Portnoi, Pis'ma Zh. Tekh. Fiz. **31** (8), 85 (2005) [Tech. Phys. Lett. **31**, 671 (2005)].

Translated by P. Pozdeev

Technical Physics Letters, Vol. 31, No. 12, 2005, pp. 1049–1051. Translated from Pis'ma v Zhurnal Tekhnicheskoĭ Fiziki, Vol. 31, No. 24, 2005, pp. 24–30.

Nuclear Magnetic Resonance and Photomagnetic Phenomena in Oxygen-Deficient Ferric Borate

I. V. Pleshakov[a,*], A. A. Nechitaĭlov[a], A. P. Paugurt[a], and V. V. Matveev[b]

[a] *Ioffe Physicotechnical Institute, Russian Academy of Sciences, St. Petersburg, 194021 Russia*

[b] *Institute of Physics, St. Petersburg State University, St. Petersburg, 199164 Russia*

* *e-mail: ivanple@yandex.ru*

Received August 8, 2005

Abstract—Single crystals of ferric borate ($FeBO_3$), annealed in vacuum so as to provide for the oxygen deficiency and the corresponding excess Fe^{2+} ion concentration, have been studied by ^{57}Fe NMR. The NMR signal intensity and the transverse nuclear relaxation rate in oxygen-deficient ferric borate are significantly increased compared to those in the initial state. The annealed samples also exhibit a giant shift of the resonance frequency under the action of light, which is several times as large as the analogous shift in samples with the equilibrium concentration of Fe^{2+} ions. The obtained experimental data confirm the model of photomagnetic phenomena in antiferromagnetic materials that is based on the notion of Fe^{2+}-containing complexes playing the role of photosensitive centers. © *2005 Pleiades Publishing, Inc.*

Ferric borate ($FeBO_3$) is a canted two-sublattice antiferromagnet with a high temperature of magnetic ordering (T_N = 348 K) and a unique combination of various magnetic properties. The special interest in this material is related to the photomagnetic phenomena [1–3], which have been observed, in particular, by NMR [4, 5]. Investigations into the mechanisms of light action upon this material [6, 7] showed that a change in the magnetic parameters could be related to a light-induced redistribution of the population of photosensitive centers, which were suggested to contain divalent iron ions (Fe^{2+}). However, the existence of such centers has not been confirmed by direct experiments. This study was aimed at obtaining such experimental evidence.

As is known, the thermal annealing of oxide compounds containing polyvalent iron (in $FeBO_3$, Fe^{2+} ions account for 0.5% of the total content of magnetic ions) can lead to the formation of oxygen vacancies and, hence, to an increase in the content of Fe^{2+} ions. In order to provide conditions favoring the oxygen yield, we have carried out the annealing in vacuum. The photomagnetic effect in $FeBO_3$ samples was studied by detecting light-induced changes in the NMR signal amplitude and frequency. It should be noted that such experiments provide, in addition to answering the main question, a qualitative verification of the existence of a relationship between the transverse nuclear relaxation rate and the concentration of a relaxant impurity (proposed to be Fe^{2+} ions).

We have studied a $FeBO_3$ single crystal with a natural content of the ^{57}Fe isotope and dimensions approximately $4 \times 3 \times 2$ mm. The sample was placed inside an excitation coil and oriented relative to the external constant magnetic field B_0 so that the coil axis was perpendicular to the field and coincided with the easy plane of the crystal. The NMR (monitored as the nuclear spin echo and induction signals) was excited by RF pulses with a duration of about 2 μs and a power not exceeding 10 μW. The measurements were performed at liquid nitrogen temperature (77 K). The nonperturbed NMR frequency ν_n was about 75.4 MHz. Since the NMR frequency is a linear function of the magnetizations of sublattices, the shift of the ν_n value observed upon illumination of the sample in fact measures the relative change in the sublattice magnetization under the action of light.

The light source was a KGM-300 halogen lamp with a total power of 300 W. The light beam extracted from the optical system output was focused on the one edge of an optical fiber bundle with a 5-mm aperture, the opposite edge being in contact with the sample surface. A two-section coil design allowed the entire crystal surface to be illuminated, with a radiation power density estimated at 1 W/cm^2. In all experiments involving illumination, the sample was initially cooled in the dark and then exposed for 20 min prior to NMR measurements. In the investigation of aftereffect, the sample after the exposure was kept in the dark for no less than 15 min.

The sample holder design allowed the sample to be always fixed in the same position, but virtually without mechanical stresses. The NMR measurements were initially performed for the unannealed crystal. Then, the sample was extracted from the holder and annealed for 1 h at 500°C in a quartz ampule evacuated to a residual pressure of about 10^{-2} mbar. Upon cooling, the sample

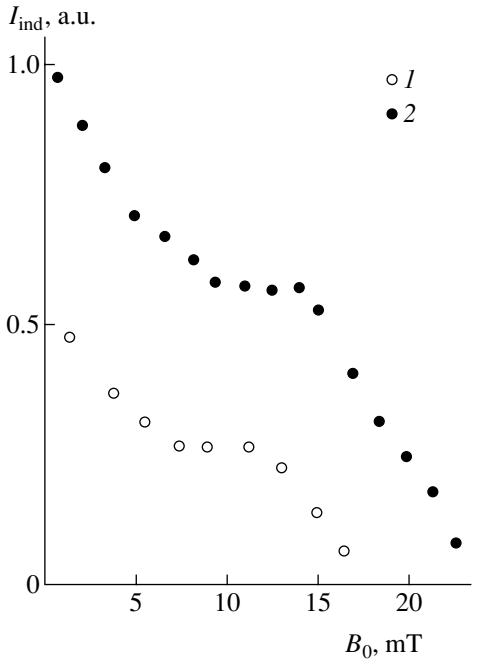

Fig. 1. Plots of the nuclear induction signal amplitude I_{ind} versus constant magnetic field strength B_0 for a $FeBO_3$ single crystal (*1*) before and (*2*) after heat treatment.

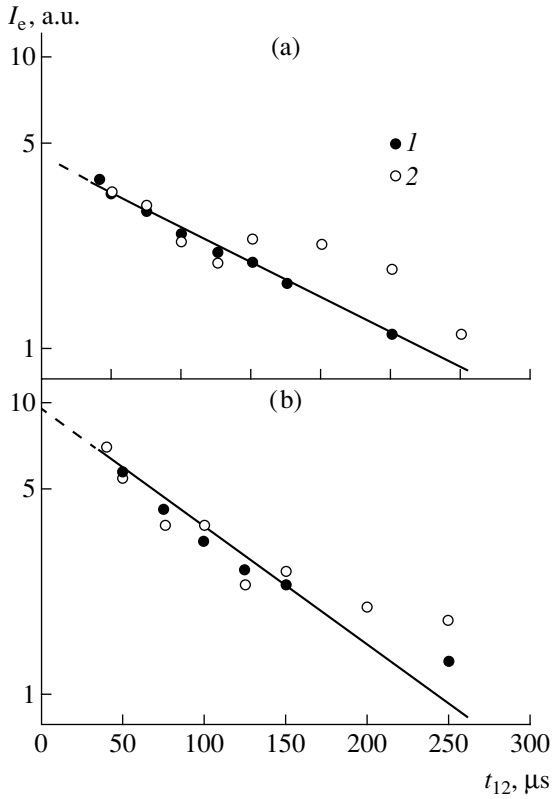

Fig. 2. Plots of the spin echo signal amplitude I_e versus delay time t_{12} between excitation pulses for a $FeBO_3$ single crystal (a) before and (b) after heat treatment, measured (*1*) prior to and (*2*) upon illumination. Solid lines show the results of the exponential fitting to experimental points *1*.

was again fixed in the excitation coil so as to exactly reproduce the previously set experimental conditions.

In this study, the response signal was received from nuclei occurring in the domain walls, rather than inside the $FeBO_3$ domains, since excitation of the latter would require a pulse power several orders of magnitude higher than that used in our NMR measurements [8]. This is confirmed by the data presented in Fig. 1, which shows the field dependences of the nuclear induction amplitude I_{ind} observed in the crystal before and after annealing. As can be seen, I_{ind} in both cases quite rapidly drops in the course of magnetization and vanishes in the region of B_0 values comparable with the saturation field. The annealing did not affect the NMR frequency, which implied that the magnetization of sublattices after this treatment remained unchanged. The annealed crystal exhibited a significant increase in the NMR signal amplitude. We believe that the heat treatment leads to a decrease in the number of extended defects (that serve as the centers of domain wall pinning), which leads to an increase in the susceptibility and, hence, the NMR gain. It is also clear that point defects (such as oxygen vacancies) do not play a significant role in the pinning of domain walls.

The transverse nuclear relaxation rate exhibited the expected sharp increase (Fig. 2). This result confirms the assumption that Fe^{2+} ions participate in the nuclear relaxation process.

The NMR parameters of the $FeBO_3$ crystal before and after the heat treatment are presented in the table. As can be seen from these data, the illumination leads to a significant increase in the NMR signal intensity, the effect having the character of a long-term memory. This result is consistent with the data [9] on the light-induced decrease in the magnetic anisotropy in the basal plane, which influences the NMR gain. In contrast, the illumination produced virtually no signal increase in the annealed sample. The exposure also rather weakly influenced the relaxation, although the exponential character of decay in the spin echo amplitude at a large delay time t_{12} between probing pulses was somewhat violated (Fig. 2). Thus, the results of our experiments show that the light-induced changes in the NMR signal amplitude and relaxation parameters are less pronounced in the sample crystal upon annealing than in the initial state, despite an increase in the concentration of photosensitive centers.

The effect of light on the NMR frequency has a substantially different character. Illumination of the crystal both in the initial state and upon annealing leads to a decrease in the frequency, but the change in the annealed sample is several times that in the unannealed one. This change is not retained and the signal frequency is restored on the initial level (ν_n = 75.4 MHz) upon switching off the light. The experiments with light attenuated using neutral filers showed that the NMR frequency shift $\Delta\nu_n$ is a linear function of the radiation

Parameters of NMR in $FeBO_3$ single crystals before and after heat treatment in vacuum

Illumination conditions	I_{ind}, a.u.		I_{e0}^{**}, a.u.		T_2, μs	
	before annealing	after annealing	before annealing	after annealing	before annealing	after annealing
Prior to exposure	1.0	1.9	1.0	2.1	370	220
15 min after exposure	1.15	1.95	1.0*	2.1*	370*	220*

* Measured for the delay time between pulses below 150 μs (Fig. 2).

** Spin echo signal extrapolated to zero delay time.

power. At a maximum illumination intensity, $\Delta\nu_n = 150$ and 900 kHz in the crystal before and after annealing, respectively, which allows us to classify the observed effect as a "giant" one. It should be noted that this significant difference in $\Delta\nu_n$ observed for the two samples at the same intensity of illumination is additional evidence in favor of the nonthermal nature of this phenomenon as previously discussed in [4–7]. The giant frequency shift decreases with time, and the $\Delta\nu_n$ value drops to ~200 kHz within about ten days after annealing.

The mechanism of the light-induced change in the NMR frequency (in fact, in the magnetization of the crystal) is still not completely clear. According to the theoretical description [6] of the contribution due to Fe^{2+} ions, the change in the total magnetization is due to a modification of the canting angle between the sublattices. However, the results of our experiments show that this effect has to be at least supplemented by a change in the magnetization of each sublattice, since this very magnetization is linearly related to the variable NMR frequency. In any case, the role of the photosensitive complexes containing Fe^{2+} ions is now evident because a change in their concentration substantially alters the observed effect.

In conclusion, the annealing of ferric borate single crystals leads to an increase in the NMR signal intensity, which is probably related to the modification of centers responsible for the pinning of domain walls and leads to the corresponding increase in the NMR gain. An increase in the content of Fe^{2+} ions leads to acceleration of the transverse nuclear relaxation. This behavior is qualitatively consistent with the existing theoretical notions about the relaxation processes in magnetically ordered materials. The obtained results confirm the existence of a photoinduced change in the magnetocrystalline anisotropy in the basal plane. The most significant manifestation of the photomagnetic phenomena is the giant shift of the NMR frequency under the action of light in a material with increased concentration of photosensitive centers, this change showing a tendency to decrease with the time after illumination.

REFERENCES

1. D. E. Lacklison, J. Chadwick, and J. L. Page, J. Appl. Phys. **42**, 1445 (1971).
2. D. E. Lacklison, J. Chadwick, and J. L. Page, J. Phys. D **5**, 810 (1972).
3. M. Borovets, A. A. Garmonov, S. G. Rudov, and Yu. M. Fedorov, Pis'ma Zh. Éksp. Teor. Fiz. **50**, 431 (1989) [JETP Lett. **50**, 466 (1989)].
4. I. V. Pleshakov, Pis'ma Zh. Tekh. Fiz. **29** (11), 65 (2003) [Tech. Phys. Lett. **29**, 471 (2003)].
5. I. V. Pleshakov and V. V. Matveev, J. Phys.: Condens. Matter **16**, 1725 (2004).
6. G. S. Patrin, D. A. Velikanov, and G. A. Petrakovskiĭ, Zh. Éksp. Teor. Fiz. **103**, 234 (1993) [JETP **76**, 128 (1993)].
7. G. S. Patrin, D. A. Velikanov, and G. A. Petrakovskiĭ, Fiz. Tverd. Tela (St. Petersburg) **37**, 1214 (1995) [Phys. Solid State **37**, 659 (1995)].
8. Kh. G. Bogdanova, A. R. Bulatov, V. E. Leont'ev, *et al.*, Fiz. Met. Metalloved. **91**, 28 (2001).
9. M. H. Seavey, Solid State Commun. **12**, 49 (1973).

Translated by P. Pozdeev

Technical Physics Letters, Vol. 31, No. 12, 2005, pp. 1052–1054. Translated from Pis'ma v Zhurnal Tekhnicheskoĭ Fiziki, Vol. 31, No. 24, 2005, pp. 31–38.

Experimental Study of Chaotic Oscillations Generated by an Ensemble of Cascade-Coupled Phase Systems

K. G. Mishagin*, V. V. Matrosov, V. D. Shalfeev, and V. V. Shokhnin

Nizhni Novgorod State University, Nizhni Novgorod, Russia

** e-mail: mishagin@rf.unn.ru*

Received June 3, 2005

Abstract—Chaotic dynamics in the ensemble of two cascade-coupled phase systems has been experimentally studied. Various chaotic regimes observed in this ensemble are classified. The experiments showed that the ensemble acts as a generator of chaotic oscillations within a broad domain in the space of system parameters.

In recent years, the problem of using dynamical chaos for data transmission has been given much attention [1–3]. In such applications, it is desired that the chaotic signal possess a broad spectrum and that the generation of chaos be possible in a broad range of parameters.

Phase locked loops (PLLs), referred to below as phase systems [4], are widely used in the traditional communication systems employing regular signals. The PLLs are capable of operating in a range from low to superhigh (microwave) frequencies and possess a high noise immunity. Previously, we suggested [2, 3] using phase systems for solving problems related to data transmission by means of dynamical chaos, including the generation of chaotic oscillations. As is known, phase systems with complex (e.g., second-order) filters can feature both regular and chaotic self-modulation regimes [5]. However, the domains of system parameters admitting chaotic regimes are very small, which hinders the use of such systems as chaos generators. It has been demonstrated [3, 6, 7] that, by connecting phase systems into small ensembles, it is possible to provide for the generation of chaotic oscillations in a broad and homogeneous domain of parameters. In particular, we performed a qualitative numerical analysis [2] of a model ensemble comprising two cascade-coupled phase systems with second-order filters in the control loops. This Letter presents the results of the experiments, which confirm the possibility of generating chaotic oscillations in such ensembles in a broad domain in the space of system parameters.

The experiments were performed with an ensemble of two cascade-coupled phase systems (subsystems I and II) based on the well-known 74HC4046A integrated circuit (IC), which represents a phase lock for the synchronization of signals of the meander type. Using this IC, it is possible to design a PLL control system and set the frequency and bandwidth of phase locked oscillators. Figure 1 shows a schematic diagram of the experimental setup, in which *1* is the master oscillator, *2* are the phase comparators (realizing the exclusive-OR operation of Boolean algebra), and (*3*, *4*) are the voltage-controlled generators of discontinuous oscillations. In this scheme, k is the coupling coefficient and $K_i(p)$ (i = 1–5) are the transfer constants of low-frequency first-order filters ($p = d/dt$) defined as

$$K_i(p) = \frac{1}{1 + T_i p}, \qquad (1)$$

where $T_i = R_i C_i$ (i = 1–5) is the time constant of the ith filter ($T_1 = T_2 = 14.9$ μs, $T_4 = T_5 = 165$ μs, $T_2 = 0$–330 μs (variable parameter)), $R_1 = R_3 = 2.2$ kΩ, $R_4 = R_5 = 5$ kΩ, $R_2 = 0$–10 kΩ, $C_1 = C_3 = 6.8$ nF, and $C_2 = C_4 = C_5 = 33$ nF. The frequencies of voltage-controlled oscillators *3* and *4* in the absence of external signals and noise at the input are $f_1 = f_2 = 71$ kHz (central frequency). In the course of experiments, the frequencies of oscillators *3* and *4* remained unchanged. Signals entering the phase systems, as well as those generated at their outputs, are unipolar meanders with an amplitude of 5 V. The maximum frequency detuning of the

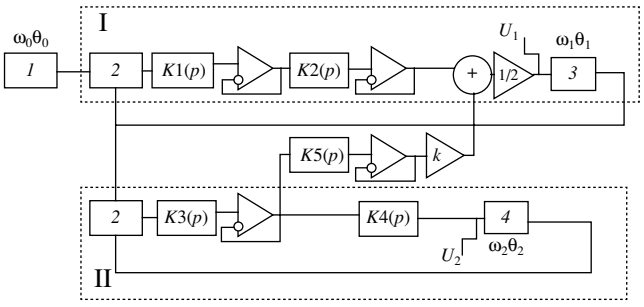

Fig. 1. Schematic diagram of the experimental setup comprising an ensemble of cascade-coupled phase systems I and II (see the text for explanations).

1063-7850/05/3112-1052$26.00 © 2005 Pleiades Publishing, Inc.

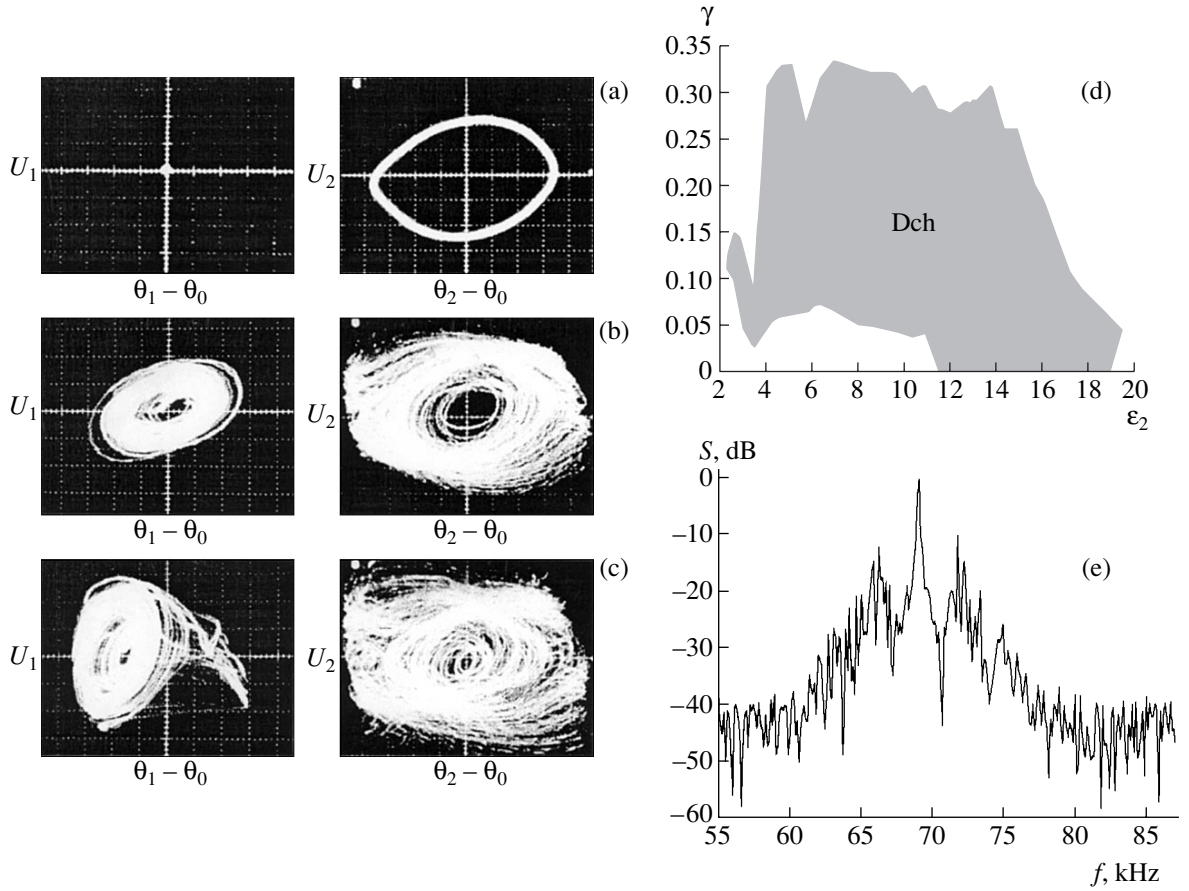

Fig. 2. Oscillations in the experimental ensemble of two cascade-coupled phase systems: (a–c) projections of phase portraits for $k = 0$, 0.3, and 0.6, respectively; (d) domain of chaotic-modulated oscillations (Dch) in the (γ, ε_2) plane for subsystem I; (e) the typical power spectrum of chaotic-modulated oscillations in subsystem I.

input signal (relative to the central frequency) for subsystems I and II at which the synchronization of oscillators *3* and *4* is possible (i.e., the phase lock bandwidths $\Delta F_{1,2}$) were as follows: $\Delta F_1 = 13.85$ kHz; $\Delta F_2 = 27.7$ kHz. In the course of measurements, we have varied the feedback gain $k = 0$–1 (the coupling parameter, which determines the signal fed from the control loop of subsystem II to that of subsystem I), the master oscillator frequency f_0, and the time constant T_2 of the second filter in the control loop of subsystem I.

Phase systems may feature various regimes in which the phase difference between response and master signals is either limited (synchronous and quasi-synchronous regimes) or exhibits unlimited growth or decay (beats). In order to identify various dynamical regimes and obtain the corresponding phase portraits, we have designed and constructed two digital detectors capable of determining the phase differences between the master and response signals for systems I and II. The phase differences $\theta_1 - \theta_0$ and $\theta_2 - \theta_0$ could be determined in the entire range from 0 to 2π (Fig. 2).

In the experimental scheme under investigation, the phase systems involve second-order filters in the control loops. The dynamics of an isolated phase system with second-order filter was described previously [5] and it was demonstrated that such systems exhibit chaotic dynamics within small domains in the space of parameters. These domains are outside the range of parameter variation in the given experimental scheme. Therefore, the coupled systems exhibit only regular intrinsic dynamics in the accessible domain of parameters. Subsystem I features either a synchronous regime or beats, so that its dynamics is analogous to that of a phase system with first-order filter. Subsystem II can occur, in addition to in the regimes of synchronization and beats, in a regular quasi-synchronous regime. In this regime, the response oscillator frequency exhibits periodic variations around a mean value equal to the master signal frequency and the phase difference $\theta_2 - \theta_0$ is limited ($|\theta_2 - \theta_0| < 2\pi$).

Figures 2a–2c show projections of the phase portraits of both response systems observed for various values of the coupling parameter k (feedback gain) for a master frequency of f_0 69.9 kHz and $R_2 = 5$ kΩ. In these patterns, the ordinate measures the input voltages $U_{1,2}$ of the corresponding response oscillators (see Fig. 1),

which are proportional to the instantaneous frequency detunings between response and master signals, while the abscissa corresponds to the phase difference $\theta_1 - \theta_0$ or $\theta_2 - \theta_0$ (left- and right-hand columns show projections of the phase portraits for systems I and II, respectively).

Let us consider in more detail the process of chaos excitation in the experimental system as illustrated in Figs. 2a–2c. When the feedback between the two coupled phase systems is absent, subsystem I occurs in a synchronous regime and subsystem II, in a regular quasi-synchronous regime (Fig. 2a). The introduction of a feedback gives rise to oscillations in the control loop of subsystem I, which are chaotic at a relatively small value of the coupling coefficient: $k \approx 0.04$ (the chaotic regime was visually detected by monitoring the projections of phase portraits). Since the transition to chaos takes place in an extremely narrow interval of k values, the scenario of this transition is not revealed in experiment. It can only be noticed that the transition is soft, whereby a chaotic attractor appears in the vicinity of a regular limit cycle that loses stability. Figure 2b shows the projections of phase portraits for $k = 0.3$. In this case, subsystem I exhibits chaotic oscillations and the phase difference $\theta_1 - \theta_0$ is limited. This regime corresponds to the generation of quasi-synchronous oscillations at the output of the first response system, with a frequency exhibiting chaotic variations around a certain average value stabilized relative to the master frequency. Such oscillations, belonging to the type of chaotic-modulated, are most interesting from the standpoint of their use as a chaotic carrier signal for data transmission [3]. In subsystem II, the phase difference $\theta_1 - \theta_0$ is not restricted and oscillations correspond to the regime of chaotic beats. As the coupling parameter is increased to $k \geq 0.6$, subsystem I also passes to the regime of chaotic beats (Fig. 2c, $k = 0.6$). For limitations imposed on the variable parameters in the experimental system under consideration ($f_1 = f_2$, $k = 0$–1, $R_2 = 1$–10 kΩ) and the other fixed parameters, the ensemble of two coupled systems exhibited the following states: (i) chaotic-modulated oscillations in subsystem I and chaotic beats in subsystem II and (ii) chaotic beats in both systems I and II.

The results of experiments showed that the scheme under consideration is capable of generating chaotic-modulated oscillations at the output of subsystem I in a broad domain of parameters. Figure 2d shows a region of the existence of such regimes in the (γ, ε_2) plane for subsystem I at $k = 0$, where $\gamma = (f_1 - f_0)/\Delta F_1$ and $\varepsilon_2 = R_2 C_2 \Delta F_1$ (there is an analogous region for the negative values of γ). The domain of parameters corresponding to the generation of chaotic-modulated oscillations well agrees with the results of qualitative numerical analysis reported previously [2].

Figure 2e presents the typical experimental power spectrum of chaotic-modulated oscillations measured at the output of subsystem I in the region of the first harmonic of the master frequency for $f_0 = 69$ kHz, $k = 0.3$, and $R_2 = 5$ kΩ (it should be recalled that the experimental scheme employs voltage-controlled generators of discontinuous oscillations, which produce output signals of the meander type). The reduced width of this spectrum, which is one of the most substantial characteristics, can be estimated as

$$\eta = \frac{\Delta f}{f_0} \approx 0.25, \qquad (2)$$

where Δf is the width on a level of -40 dB. This estimate shows that the chaotic-modulated oscillations generated using the scheme under consideration can be considered as broadband.

To summarize, we have experimentally observed for the first time chaos generation in an ensemble of coupled phase systems in various chaotic regimes (quasi-synchronous chaotic oscillations, chaotic beats). The ensemble of two cascade-coupled phase systems is capable of generating chaotic-modulated oscillations within a broad domain in the space of system parameters. The obtained chaotic oscillations are characterized by a broad frequency spectrum.

Acknowledgments. This study was supported by the Russian Foundation for Basic Research (project no. 05-02-17409), the "Universities of Russia" program (UR.03.01.179), the "Development of Research Potential of High School" program, and the academic research program of the Intel Corporation.

REFERENCES

1. A. S. Dmitriev and A. I. Panas, *Dynamical Chaos: New Information Carriers for Communication Systems* (Fizmatlit, Moscow, 2002) [in Russian].
2. M. V. Korsinova, V. V. Matrosov, and V. D. Shalfeev, Int. J. Bifurcation Chaos Appl. Sci. Eng. **9**, 963 (1998).
3. V. D. Shalfeev, V. V. Matrosov, and M. V. Korzinova, Zarubezh. Radioélektron. Usp. Sovrem. Radioélektron., No. 11, 44 (1998).
4. *Systems for Phase Synchronization*, Ed. by V. V. Shakhgil'dyan and L. N. Belyustina (Radio i Svyaz', Moscow, 1982) [in Russian].
5. V. V. Matrosov, Pis'ma Zh. Tekh. Fiz. **22** (23), 4 (1996) [Tech. Phys. Lett. **22**, 952 (1996)].
6. V. D. Shalfeev and V. V. Matrosov, in *Chaos in Circuits and Systems*, Ed. by G. Chen and T. Ueta (World Scientific, Singapore, 2002), pp. 111–129.
7. V. V. Matrosov and D. V. Kasatkin, Radiotekh. Élektron. (Moscow) **48**, 637 (2003).

Translated by P. Pozdeev

Technical Physics Letters, Vol. 31, No. 12, 2005, pp. 1055–1057. Translated from Pis'ma v Zhurnal Tekhnicheskoĭ Fiziki, Vol. 31, No. 24, 2005, pp. 39–44.

Fragmentation of Multiply Ionized Fullerene Molecules

V. V. Afrosimov, A. A. Basalaev, M. N. Panov*, and O. V. Smirnov

Ioffe Physicotechnical Institute, Russian Academy of Sciences, St. Petersburg, 194021 Russia

** e-mail: m.panov@mail.ioffe.ru*

Received July 22, 2005

Abstract—The dissociation of C_{60} fullerene molecules has been studied by means of an analysis of the kinetic energies of charged fragments formed upon the capture of several electrons from C_{60} by multiply charged Ar^{6+} ions. The kinetic energies of fragment ions of a multiply ionized C_{60} molecule are distributed in accordance with the Coulomb explosion mechanism of dissociation. © *2005 Pleiades Publishing, Inc.*

The properties of individual fullerene molecules can be determined, in particular, by studying their collisions with ion projectiles in the gas phase. This interaction leads to the ionization and fragmentation of fullerene molecules. An analysis of the characteristics of projectile scattering shows that these events take place when the distance between colliding particles exceeds the radius of a fullerene molecule [1]. This result implies that the fragmentation of fullerene is not related to the transfer of the kinetic energy of an impinging particle directly to carbon atoms of the target molecule. It has been reported [2, 3] that stable C_{60}^{q+} ions with charges of up to $q = 8$ can be observed upon the impact ionization of C_{60} fullerene molecules. Therefore, the Coulomb repulsion energy alone cannot account for the rupture of interatomic bonds in the C_{60}^{5+} ions studied in our experiments. At the same time, the experimental data indicate that the fragmentation can be highly probable and this probability is substantially dependent on the number of electrons lost by a fullerene molecule. This behavior is clearly manifested when electrons are captured by multiply charged projectile ions, which is the main process (in terms of the cross section) of the fullerene ion formation upon collisions in the kiloelectronvolt energy range. An increase in the number of captured electrons leads to the dissociation of fullerene molecules into smaller fragments. In particular, the capture of four to five electrons from a C_{60} molecule leads to its disintegration into fragments with the number of carbon atoms below ten.

In order to elucidate the mechanism of the dissociation of C_{60} molecules, it is important to obtain data on the kinematics of fragments and on the correlations between the charge and mass of fragment ions formed in the same collision of a fullerene molecule with a projectile ion:

$$A^{z+} + C_{60} \longrightarrow A^{(z-s)+} + \sum_{m,k} C_m^{k+}.$$

The experiments have been performed using an experimental arrangement that is schematically depicted in Fig. 1. A time-of-flight (TOF) mass spectrometer measured the mass spectrum of positive fragment ions C_m^{k+} formed upon the decay of a C_{60} molecule, which was caused its multiple ionization as a result of the electron capture by an Ar^{z+} projectile. The start signal in the TOF mass spectrometer was generated by a pulse arriving from the fast argon ion detector (D_i). The final charge $(z - s)$ of argon ions upon their collisions with fullerene molecules was determined with the aid of an electrostatic analyzer (EA). The difference s between the initial and final ion charges determined the minimum charge of C_{60}^{k+} fragment ions.

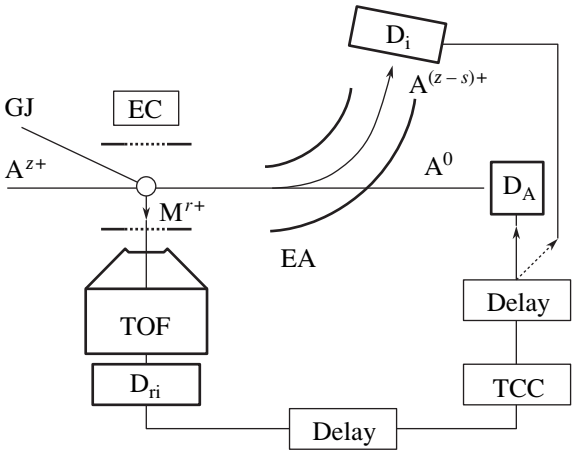

Fig. 1. Schematic diagram of the experimental arrangement: (GJ) gas jet of C_{60} fullerene molecules; (A^{z+}) beam of multiply charged argon ions ($z = 6$); (EC) extraction capacitor creating electric field with a strength of 50 V/cm; (TOF) time-of-flight mass spectrometer; (EA) electrostatic ion mass analyzer; (D_i, D_{ri}, D_A) detectors of fast ions, fullerene fragment ions, and fast neutrals, respectively; (TCC) time code converter; (Delay) pulse delay circuits.

1063-7850/05/3112-1055$26.00 © 2005 Pleiades Publishing, Inc.

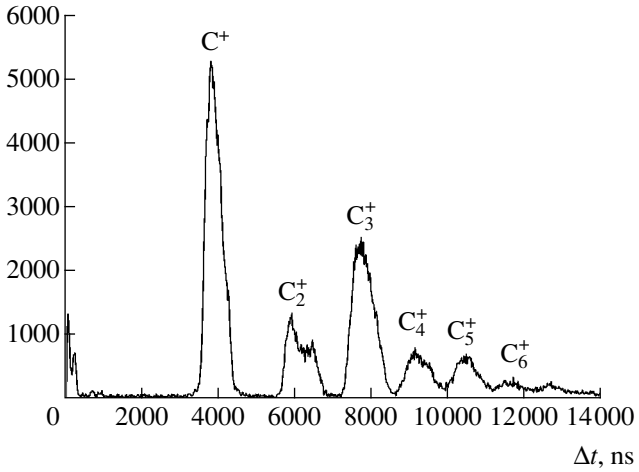

Fig. 2. The typical TOF mass spectrum of fragment ions observed upon the dissociation of C_{60} fullerene caused by the capture of five electrons by Ar^{6+} projectile ion.

Figure 2 shows an example of the complete spectrum of charged fullerene fragments formed upon the capture of five electrons from a C_{60} molecule by an Ar^{6+} ion with a kinetic energy of 60 keV. As can be seen, all the detected fragments are singly charged ions with the number of carbon atoms from one to seven. The shape and magnitude of each peak in this spectrum are determined by the probability of ion formation and the analyzer transmission function, the latter being significantly dependent on the initial ion energy. For ions bearing the same charge, the maximum TOF difference is observed between the ions whose initial velocity vectors are directed along the analyzer axis and in the opposite direction. Therefore, by measuring the width Δt of the peak base in the experimental mass spectrum, it is possible to determine the maximum kinetic energies E_{max} of ions with various masses m, since $\Delta t = (kmE_{max})^{0.5}$, where k is a coefficient dependent on the electric field strength and on the geometry of a system of ion extraction from the interaction region.

When five electrons captured from a fullerene molecule occupy the vacant levels of an Ar^{6+} ion, an energy is liberated that is equal to the difference between the total binding energies of these electrons in C_{60} and in the final Ar^+ ion. The energy spent for the sequential n-fold ionization of a fullerene is $\sum I_n = \sum(3.5 + 4n)_n = 77.5$ eV, where I_n is the ionization potential of the $C_{60}^{(n-1)+}$ ion [4, 5]. The energy liberated upon the population of five vacant electron levels in Ar^{6+} is 276–303 eV, depending on the final state of the Ar^+ ion [6]. The potential energy spent for increasing the kinetic energy of Ar^+ due to its Coulomb repulsion from the C_{60}^{5+} ion is about 20 eV for a distance of maximum approach on the order of the radius of the neutral C_{60} molecule [7]. Thus, about 178–205 eV is spent for the rupture of interatomic bonds in the C_{60}^{5+*} ion and for the excitation of fragments.

Since the capture of five electrons from C_{60} leads to the formation of only light singly charted fragment ions (see Fig. 2), their number has to be not less than five. We have studied correlations in the formation of these light ions. It was established that the dissociation of an individual molecular ion of fullerene might lead to the appearance of any combination of singly charged fragments with various masses.

In order to evaluate the maximum kinetic energy E_{max} for each fragment using data on the peak widths in the experimental mass spectrum, it is necessary to take into account the transmission function of the mass analyzer. It was assumed that the form of this function coincides with the peak shape of Ar^+ ions and nondissociated C_{60}^+ ions. Under this assumption, the E_{max} values for C^+, C_2^+, C_3^+, C_4^+, and C_5^+ ions were estimated at 19.8, 19.7, 14, 10.7, and 8.4 eV, respectively.

When the fragment ions formed upon C_{60} fullerene dissociation flying asunder as a result of their Coulomb repulsion, the total momentum of the system remains unchanged. From this we infer that the velocities of fragment ions and their energies must be proportional to their masses. The sum of the maximum energies of ions from C_2^+ to C_5^+ is 52.8 eV, which approximately corresponds to the electrostatic energy of five elementary charges arranged over a sphere with the radius equal to that of C_{60}, while the ratios of E_{max} for various fragments correspond to their expansion under the action of only the Coulomb forces. Therefore, the observed picture is consistent with the C_{60}^{5+} dissociation according to the Coulomb explosion mechanism. In the experimental distribution of the energies of fragment ions with various masses presented above, the energy of monoatomic C^+ species is unexpectedly low. This result probably indicates that these ions are not formed at the moment of fragmentation onset. The fact that the peak of C^+ in the mass spectra of fullerenes is much narrower than the other signals has also been pointed out by other researchers [8].

We may suggest that only a certain fraction of fragment ions retain their masses in the course of expansion. This very component determines the maximum broadening of peaks in the mass spectra of fragment ions. Coarse excited polyatomic ions may exhibit decay in the course of expansion with the detachment of light ions, in particular, C^+ species. This results in the formation of low-energy fragment ions contributing to the corresponding lines in the observed mass spectrum. In this decay, a considerable part of the potential energy is converted into the kinetic energy of newly formed neutral fragments.

Conclusions. The multiple ionization of a fullerene molecule caused by the capture of several electrons by a multiply charged projectile ion leads to fragmentation as a result of electron excitation of the target molecule. The capture of four or more electrons results in the formation of light singly charged fragment ions. Fragment ions formed as a result of the dissociation of a multiply ionized fullerene molecule can possess kinetic energies in excess of 10 eV. The ratios of the maximum kinetic energies of fragment ions with various masses correspond to the Coulomb explosion of a multiply charged fullerene ion, whereby the resulting fragment ions exhibit expansion due their Coulomb repulsion.

REFERENCES

1. V. V. Afrosimov, A. A. Basalaev, K. V. Kashnikov, and M. N. Panov, Fiz. Tverd. Tela (St. Petersburg) **44**, 486 (2002) [Phys. Solid State **44**, 509 (2002)].
2. J. Jin, H. Khemliche, M. H. Prior, and Z. Xie, Phys. Rev. A **53**, 615 (1996).
3. G. Seifert, R. Gutierrez, and R. Smidt, Phys. Lett. A **211**, 357 (1996).
4. G. Javahery, H. Vincel, S. Petrie, *et al.*, Chem. Phys. Lett. **204**, 467 (1993).
5. V. V. Afrosimov, A. A. Basalaev, and M. N. Panov, Zh. Tekh. Fiz. **66** (5), 10 (1996) [Tech. Phys. **41**, 412 (1996)].
6. C. E. Moore, *Atomic Energy Levels: NSRDS–NBS No. 35* (US Government Printing Office, Washington DC, 1971).
7. J. Opitz, H. Lebius, B. Saint, *et al.*, Phys. Rev. A **59**, 3562 (1999).
8. S. Tomito, H. Lebius, A. Brenac, *et al.*, Phys. Rev. A **65**, 053201 (2002).

Translated by P. Pozdeev

Technical Physics Letters, Vol. 31, No. 12, 2005, pp. 1058–1060. Translated from Pis'ma v Zhurnal Tekhnicheskoĭ Fiziki, Vol. 31, No. 24, 2005, pp. 45–50.

Information Enciphering Based on Chaotic Solutions of Deterministic Equations

G. N. Kal'yanov and Er. V. Kal'yanov

Institute of Radio Engineering and Electronics (Fryazino Branch), Russian Academy of Sciences, Fryazino, Moscow oblast, Russia

e-mail: erast@ms.ire.rssi.ru

Received July 14, 2005

Abstract—A new method of enciphering graphic information is proposed that is based upon chaotic alteration of the color of each element of a given image. The results of investigation of an original chaotic system are presented. A pseudo-random sequence of numbers formed using the obtained solutions of the corresponding system of equations is used for the enciphering and deciphering of a color graphic image. © *2005 Pleiades Publishing, Inc.*

The task of enciphering information is most frequently solved by means of telecommunication technologies employing various methods of matrix coding. In addition to using complex regular laws for matrix coding, it has been proposed to employ nonregular processes [1], whereby matrix elements are rearranged using the standard pseudo-random number generator.

In the case of a matrix model application, the lost data can be restored using a "holographic" technique; moreover, by rearranging matrix elements it is also possible, in principle, to disclose the cipher (although, in some cases, this might represent an extremely complicated task). However, using pseudo-random number generators, it is possible to develop quite stable cryptosystems based on the principle of alteration of the color of elements forming the image, rather than on the rearrangement of matrix elements. We believe that the function of a pseudo-random number generator can be effectively performed by oscillators with chaotic dynamics, especially by some artificial dynamical systems [2–7]. Such systems are preferred because chaos described by the corresponding equations can be more developed (even in a relatively simple form).

This Letter describes a new method of enciphering graphic information that is based upon chaotic alteration of the colors (symbols) forming a given image. A pseudo-random sequence of numbers is formed using an original system of equations:

$$dx/dt = \alpha(y - x), \quad dy/dt = x(z - \beta), \quad dz/dt = \gamma - xy, \tag{1}$$

where α, β, and γ are positive coefficients. Equations (1) describe an artificial autooscillatory system. One important feature of the solutions to Eqs. (1), which represents a system with chaotic dynamics, is their high sensitivity to changes in the values of parameters. It is this very circumstance that hinders any unauthorized deciphering of the information coded using deterministic chaos.

In order to illustrate the high sensitivity of the proposed system with respect to a change in the parameters, we will compare the oscillations of two autonomous systems described by Eqs. (1) with different subscripts (i = 1, 2) at the variables and coefficients:

$$dx_1/dt = \alpha_1(y_1 - x_1), \quad dx_2/dt = \alpha_2(y_2 - x_2),$$

$$dy_1/dt = x_1(z_1 - \beta_1), \quad dy_2/dt = x_2(z_2 - \beta_2), \tag{2}$$

$$dz_1/dt = \gamma_1 - x_1y_1, \quad dz_2/dt = \gamma_2 - x_2y_2.$$

Figure 1 shows the typical fragments of time series of the difference oscillations $x_1(t) - x_2(t)$ obtained for the two systems, which were identical except for small differences between the values of α_1 and α_2. The time series presented in Figs. 1a–1c correspond to $\alpha_1 = 1$, $\beta_1 = \beta_2 = 0.8$, $\gamma_1 = \gamma_2 = 1.2$, and $\alpha_2 = 1.1$ (a), 1.01 (b), and 1.000001 (c). The initial conditions in all cases and for all variables were selected identical and equal to 0.1.

The structure of oscillations observed in the two systems shows evidence for a growing difference between the two chaotic processes even at a small change in one of the parameters. Indeed, even in the case of $\alpha_1 - \alpha_2 = 0.01$, the difference oscillations appear with a significant delay. As the difference $\alpha_1 - \alpha_2$ is decreased, the delay tends to grow, extending from the interval $t \in [0–20]$ (Fig. 1b) to $t \in [0, 52]$ (Fig. 1c). The delay (which can be conditionally considered as a kind of "transient" process) is readily eliminated by rejecting the initial portion of time series (this rejection is necessary for the enciphering of information).

1063-7850/05/3112-1058$26.00

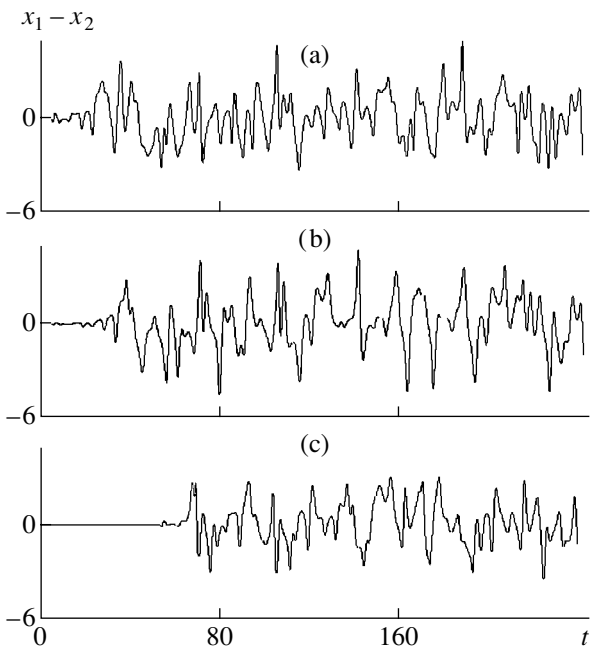

Fig. 1. Fragments of the typical time series of difference oscillations in chaotic systems described by Eqs. (1) with slightly changed parameters (see the text for explanation).

Using chaotic solutions of Eqs. (1), it is possible to create a rather complicated cipher that cannot be disclosed unless the exact initial conditions and parameters of the dynamical system (for which the solution is obtained) are exactly reconstructed. As was noted above, the admixture of a pseudo-random sequence of numbers obtained using a solution of chaotic equations is expediently performed so as to provide for a chaotic alteration of the color spectrum. This is the basic idea of specially developed software (written in C++ Builder language) that provides both enciphering and deciphering of information using a system with chaotic dynamics.

The transformation of a graphic matrix is performed so that each color (symbol) forming the given image is replaced by a new color (symbol) in accordance both with the initial color spectrum and with chaotic solutions of the differential equations describing a selected dynamical system. This is provided by a condition whereby the new index of a pixel color is equal to the initial index plus an additional index that is determined by a solution of differential equations of the chaotic system. Each symbol of the graphic matrix is sequentially transformed in the same push-down block of memory. The inverse process (deciphering) is performed using an analogous transformation algorithm, which differs from the direct one in that the color spectrum is formed by subtracting a pseudo-random number sequence that is formed using solutions of the same equations as those used in the enciphering process.

In order to illustrate the enciphering and deciphering processes, we have used a 24-bit color matrix in the form of a graphic image. Figure 2a shows the image of three words obtained using a multicolor matrix. For better illustration, the words were painted in three colors—red, green, and blue (on yellow background)—each corresponding to the word meaning (e.g., word "RED" was painted red). Although the image presented in Fig. 2a was obtained in color, this image was printed on a black-and-white printer. For this reason, the color variations are reproduced in Fig. 2a (as well as in Figs. 2b and 2c) as gray gradations. After accomplishing the transformation procedure using the enciphering matrix, the initial image of words (presented in Fig. 2a)

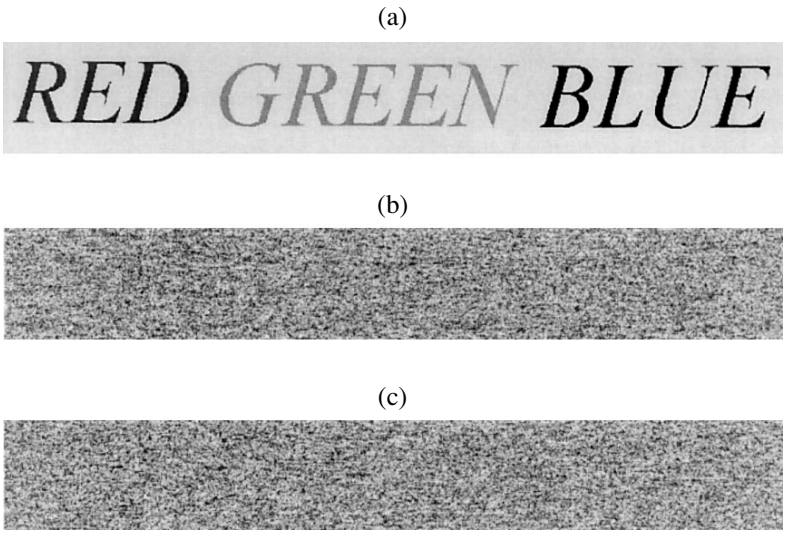

Fig. 2. A three-color image in the initial (a) and (b) enciphered form; and (c) the image obtained upon incorrect (or unauthorized) deciphering, whereby two system parameters are set correctly (α = 1.123456789123456, β = 0.8) and the third parameter γ = 1.200000000000001 is set with an error of 10^{-15} relative to the correct value (γ = 1.2).

appears as depicted in Fig. 2b. As can be seen, the enciphered image shows a good (chaotic) mixing of colors (in black-and-white form, of the gray gradations), rendering the initial information reliably hidden.

The example of an enciphered image presented in Fig. 2b was obtained using Eqs. (1) with $\alpha = 1.123456789123456$, $\beta = 0.8$, and $\gamma = 1.2$. Authorized deciphering of the image in Fig. 2b with exactly the same parameters leads to the precisely reconstructed image of Fig. 2a. In contrast, in the case of a negligible error in at least one of the parameters (e.g., in cases of unauthorized attempts), successful deciphering is practically impossible. Even an error as small as 10^{-15} in one of the parameters (see Fig. 2c) leaves the image similar to that in Fig. 2b, although with a different distribution of pixel colors.

The results of our investigations of the proposed enciphering and deciphering method showed that, in coding the symbols of colors forming the image, it is possible to use pseudo-random sequences of integers that are formed as a result of the solution of nonlinear differential equations with chaotic dynamics describing the models of artificially constructed chaotic systems.

In the case of information enciphering by means of a pseudo-random number sequence, alteration of the colors (symbols) forming a given image provides for a reliable masking of this image. Taking into account the high stability of the given cipher, information enciphered using the proposed method can be transmitted via open communication channels (e.g., via e-mail or radiation) and stored in free-access archives. The secrecy of such enciphered information transmitted via open channels is no worse than that provided by masking in the case of transmission via radiation of chaotic oscillations using methods described in [8–13].

Acknowledgments. This study was supported by the Russian Foundation for Basic Research, project no. 04-02-16536.

REFERENCES

1. V. V. Kolesov, N. N. Zalogin, and G. M. Vorontsov, Radiotekh. Élektron. (Moscow) **47**, 583 (2002).
2. O. Gurel and D. Gurel, *Types of Oscillations in Chemical Reactions* (Springer, Heidelberg, 1983; Mir, Moscow, 1986).
3. O. E. Rössler, Phys. Lett. A **57**, 397 (1976).
4. J. C. Sprott, Phys. Rev. E **50**, 647 (1994).
5. V. Ya. Kislov and V. V. Kislov, Radiotekh. Élektron. (Moscow) **42**, 962 (1997).
6. E. V. Kal'yanov, Pis'ma Zh. Tekh. Fiz. **30** (13), 45 (2004) [Tech. Phys. Lett. **30**, 550 (2004)].
7. E. V. Kal'yanov, Pis'ma Zh. Tekh. Fiz. **30** (15), 30 (2004) [Tech. Phys. Lett. **30**, 633 (2004)].
8. K. M. Cuomo and A. V. Oppenheim, Phys. Rev. Lett. **71**, 65 (1993).
9. I. I. Matrosov, Pis'ma Zh. Tekh. Fiz. **22** (23), 4 (1996) [Tech. Phys. Lett. **22**, 952 (1996)].
10. A. S. Dmitriev and L. V. Kuz'min, Pis'ma Zh. Tekh. Fiz. **25** (16), 71 (1999) [Tech. Phys. Lett. **25**, 665 (1999)].
11. E. V. Kal'yanov, Pis'ma Zh. Tekh. Fiz. **27** (16), 1 (2001) [Tech. Phys. Lett. **27**, 665 (2001)].
12. V. I. Ponomarenko and M. D. Prokhorov, Pis'ma Zh. Tekh. Fiz. **28** (16), 37 (2002) [Tech. Phys. Lett. **28**, 680 (2002)].
13. A. S. Dmitriev, B. E. Kyarginskiĭ, A. I. Panas, *et al.*, Pis'ma Zh. Tekh. Fiz. **29** (2), 70 (2003) [Tech. Phys. Lett. **29**, 72 (2003)].

Translated by P. Pozdeev

Technical Physics Letters, Vol. 31, No. 12, 2005, pp. 1061–1064. Translated from Pis'ma v Zhurnal Tekhnicheskoĭ Fiziki, Vol. 31, No. 24, 2005, pp. 51–59.

On the Nature of the Vorob'evs Effect in Pulse Breakdown of Solid Dielectrics

G. A. Mesyats

Lebedev Institute of Physics, Russian Academy of Sciences, Moscow, 117924 Russia
e-mail: isakov@sci.lebedev.ru; mesyats@nsc.gpi.ru

Received August 12, 2005

Abstract—The Vorob'evs effect consists in certain features of the discharge observed when a solid dielectric in contact with two rodlike electrodes is placed in a liquid dielectric medium and a voltage pulse with increasing front is applied to the electrodes. When the pulse front slope is small, the discharge develops in the liquid over the solid dielectric surface; whereas the discharge at a sufficiently large slope of the pulse front penetrates into the solid and produces its fracture with cleavage of the surface fragments. In order to explain this phenomenon, it is suggested that, at a sufficiently high voltage buildup rate, a displacement current that is related to the motion of the surface discharge plasma passes through a microprotrusion occurring on the electrode surface at the contact site and causes the electric explosion of this microprotrusion. The metal plasma jet generated as a result of this explosion penetrates into the solid dielectric and forms a discharge channel in depth of this material. The surface discharge plasma formed at a small slope of the voltage pulse front closes the electrode circuit, thus preventing the discharge penetration in depth of the solid. © *2005 Pleiades Publishing, Inc.*

Investigations into the electric strength of dielectrics under the action of voltage pulses with increasing leading fronts have revealed a difference in the behavior of the breakdown voltage–time characteristics of liquid and solid dielectrics. As the voltage buildup rate (pulse front slope, voltage ramp) or the duration of action was increased, the electric strength of liquid dielectrics became greater than that of solid ones [1]. Under static voltage U_s, the electric strength of solid dielectrics usually exceeds that of liquid ones. However, in the case of voltage pulses with a front duration below 10^{-6} s and an amplitude U_p on the order of 10^5 V, the electric strength of dielectric liquids (even of water) becomes higher than that of solid dielectrics, including rocks. The voltage buildup rate $A = dU/dt$ at which this phenomenon takes place is called the critical ramp and denoted A_c [2]. The effect of the critical voltage ramp in dielectrics was originally observed by A.A. Vorob'ev and G.A. Vorob'ev [1] and is named after them.

The manifestation of the Vorob'evs effect is illustrated in Fig. 1. Here, curves *1* and *2* represent the voltage–time characteristics describing a relationship between the breakdown voltage and the duration of its action for solid and liquid dielectrics, respectively, tested by voltage pulses with a certain slope of the leading front. The point of intersection of these curves determines the critical ramp A_c. Figure 1 also shows the variation of the voltage drop in a solid dielectric before and after the breakdown. Knowledge of this phenomenon has provided a basis for the development of the method of electric pulse erosion of solid dielectric media, which is used in a number of applications, such as hole drilling; crushing, grinding, and cutting of solids; separation processes, etc. However, the nature of this phenomenon is still not completely clear. The author believes that it can be rationalized based on the notions about microexplosions in the surface layers of electrodes and about ecton processes, which were developed previously within the framework of the physics of vacuum discharge [3, 4].

Let us analyze the simplest scheme of realization of the Vorob'evs effect. We consider a solid dielectric immersed into a liquid dielectric medium contained in a grounded all-metal case. The solid dielectric surface is in contact with two rodlike electrodes (cathode and anode), to which a voltage pulse with the leading front buildup $U(t)$ is applied (Fig. 2a). If the voltage buildup rate is below the critical ramp ($A < A_c$), a discharge between electrodes is developed in the liquid phase over the solid dielectric surface, whereas for $A > A_c$, the discharge penetrates into the solid. This leads to a dielectric breakdown between the cathode and anode, which develops in depth of the solid dielectric (Fig. 2b). For various combinations of solid and liquid dielectrics and the electrode materials, the critical voltage ramp A_c varies in the range from 10^{10} to 10^{11} V/s [2]. If a sufficiently large energy supplied from a pulse generator is liberated within a rather short time in the discharge channel, this will lead to an explosion in depth of the solid dielectric with the formation of a cavity on the solid surface (Fig. 2c).

What factor drives the discharge to penetrate into the solid dielectric? It is suggested that a large energy

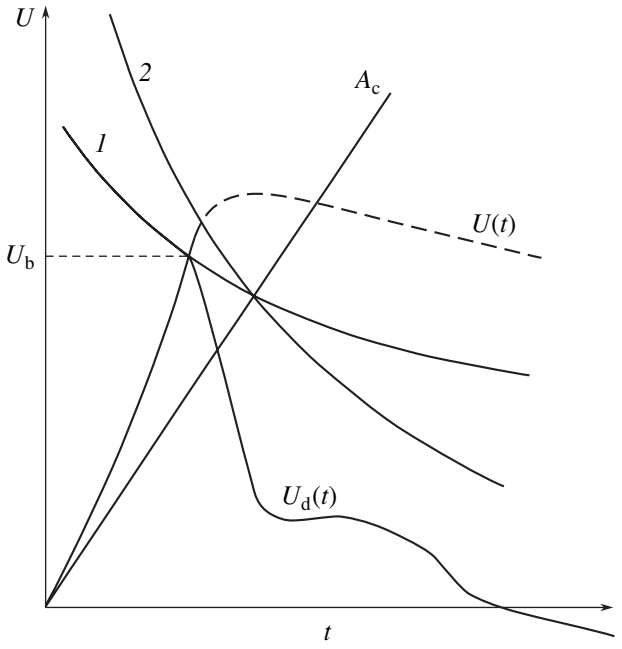

Fig. 1. Schematic diagrams illustrating the Vorob'evs effect: (*1*, *2*) voltage–time characteristics of the solid and liquid dielectrics, respectively; A_c, critical pulse front buildup rate (voltage ramp) above which the Vorob'evs effect is observed; $U(t)$, applied voltage pulse; U_b, breakdown voltage for the solid dielectric; $U_d(t)$ voltage drop in the solid dielectric.

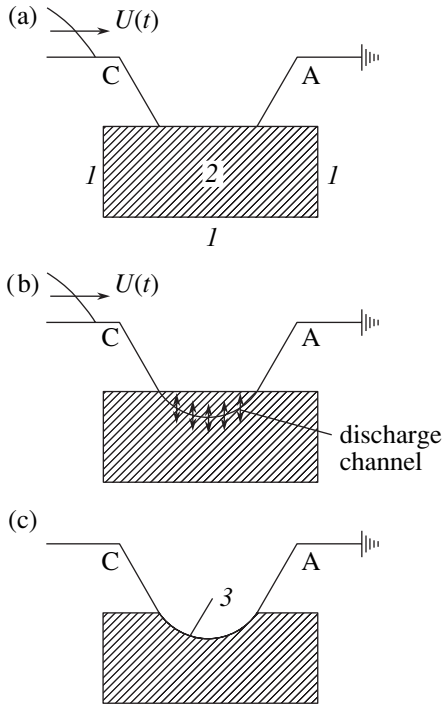

Fig. 2. Schematic diagrams illustrating the principle of electric pulse erosion of a solid dielectric by mechanism of the Vorob'evs effect: (*1*) liquid dielectric medium; (*2*) solid dielectric; (*3*) cavity formed as a result of explosive cleavage of the solid surface; (A, C) rodlike anode and cathode, respectively; $U(t)$, pulsed voltage with a supercritical ramp.

density (~10^4 J/g) in a microscopic volume of the electrode material leads to the electric explosion of this volume, which is accompanied by the ejection of a narrow plasma jet moving at a velocity on the order of 10^6 cm/s. The jet penetrates into the solid dielectric occurring in contact with the electrode and initiates a breakdown in this solid. Liberation of the large energy density in a microscopic volume can be related to the Joule heating of microprotrusions (present on the cathode surface) by the current of cold electron emission during the discharge in vacuum. In the case under consideration, the explosion is also related to the "triple point" formation on the cathode or anode [5]. Indeed, the electrode surface is always inhomogeneous and contains a large number of microprotrusions [3–5]. In fact, the metal electrode is in contact with the solid dielectric only at separate points. Such points, featuring the contact of three media (metal and the solid and liquid dielectrics), are called triple points. At the surface of a microprotrusion, the local electric field is many times stronger than the average field determined by the applied voltage. This leads to the development of electric discharge in the liquid dielectric medium at the solid surface. The discharge plasma moving over the solid surface gives rise to a displacement current. This current passes through a microprotrusion, in which the current density may exhibit a sharp increase up to 10^8–10^9 A/cm^2. This is just what accounts for the electric explosion of microprotrusions on the electrode surface.

Let us consider a mechanism of the Vorob'evs effect using a scheme depicted in Fig. 3, which shows a rodlike electrode *1* (for certainty, cathode) and a plane electrode *2* (anode) in contact with a dielectric plate *3*.

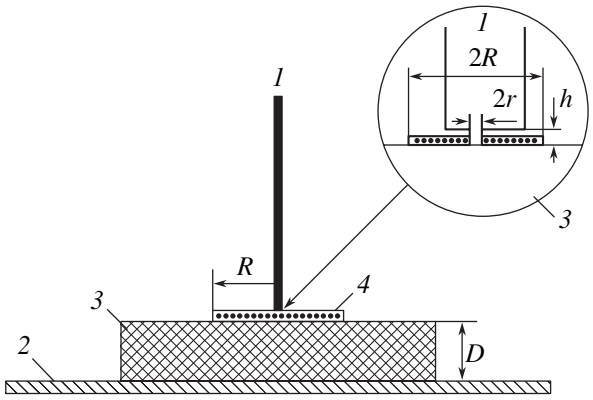

Fig. 3. Schematic diagram illustrating the phenomenon of a pulse breakdown of solid dielectrics: (*1*) rodlike electrode with a microprotrusion; (*2*) flat grounded electrode; (*3*) solid dielectric plate; (*4*) surface discharge plasma. The inset shows the microprotrusion geometry.

The inset schematically shows the contact between electrode *1* and plate *3* in more detail. Here, a microprotrusion has the shape of a cylinder with radius r and height h. We assume that the pulsed voltage U applied between electrodes *1* and *2* increases with time on the pulse front according to a linear law,

$$U = At, \tag{1}$$

where $A = U_a/t_{fr}$ is the voltage ramp, U_a is the pulse amplitude, and t_{fr} is the pulse front width. At a certain applied voltage, electric discharge is developed in the dielectric liquid over the solid surface. Assuming that the discharge plasma formed at the cathode surface occupies a circular region with the radius R and the surface area S, we obtain the relations

$$R = v_l t; \quad S = \pi v_l^2 t^2, \tag{2}$$

where v_l is the velocity of plasma spreading in the liquid over the solid dielectric surface. This plasma geometry is actually observed in the case of a relatively short pulse front ($t_{fr} \le 10^{-7}$ s [6]). After a longer time, the discharge at the solid dielectric surface takes the form of streamers.

If the solid dielectric plate is thick ($D \gg R$), then the spreading plasma layer is characterized by the dynamical capacitance [7]

$$C = 4\varepsilon_0 \varepsilon R = 4\varepsilon_0 \varepsilon v_l t, \tag{3}$$

where ε_0 is the permittivity of vacuum and ε is the relative permittivity of the solid dielectric. This motion also creates a displacement current that can be expressed with allowance for formulas (1) –(3) as

$$i = \frac{dUC}{dt} = 8\varepsilon_0 \varepsilon A v_l t, \tag{4}$$

where the plasma spreading velocity v_l is assumed to be independent of time [6]. If this current passes through the edge of the microprotrusion (see the inset in Fig. 3), the current density is

$$j = \frac{i}{\pi r^2} = \frac{8\varepsilon_0 \varepsilon A v_l}{\pi r^2}. \tag{5}$$

Assuming that the pulse front width t_{fr} is much greater than the characteristic time of thermal processes in microprotrusions, we can write this as [4]

$$t_{fr} \gg \frac{h^2 \rho c}{\lambda}, \tag{6}$$

where ρ, c, and λ are the density, heat capacity, and thermal conductivity of the metal, respectively. In this case, heating of the microprotrusion proceeds like a stationary process, and the explosion takes place when the current density reaches a certain critical level [4]:

$$j_0 = \frac{\pi}{2h}\left(\frac{\lambda}{\kappa_0}\right)^{1/2}. \tag{7}$$

For a linear dependence of the metal resistivity κ on the absolute temperature T, the coefficient κ_0 is determined from the relation

$$\kappa = \kappa_0 T. \tag{8}$$

For the microprotrusion with a height of $h = 1$ μm in copper electrode, the critical current density for explosion is $j_0 = 3 \times 10^8$ A/cm^2 [4].

Equating the current densities according to formulas (5) and (7), we can estimate the time required for the explosion of a microprotrusion on the electrode. Let us assume that the time delay of the breakdown in a liquid dielectric on the solid surface is $t_{st} \ll t_{fr}$. This assumption is quite reasonable, since a very large field enhancement at the microprotrusion end leads to the breakdown initiation even at a relatively small voltage applied to electrodes. Then, the time to the onset of discharge in the solid dielectric is

$$t_d = \frac{\pi j_0 r^2}{8\varepsilon_0 \varepsilon A v_l}. \tag{9}$$

The electric explosion of the microprotrusion gives rise to a narrow plasma jet propagating at a velocity on the order of 10^6 cm/s into the solid dielectric, which leads to the formation of a discharge channel growing in the dielectric at a rate of v_d. This phenomenon resembles the electric spark processing of metals, in which case an analogous plasma jet produces erosion of the opposite metal electrode in micron-wide gaps. At the same time, plasma propagates from the cathode to anode at a velocity of v_l over the dielectric surface and can eventually close the electrode circuit. If no discharge is developed from the anode side, the time required to close the circuit in this way can be estimated as

$$t_l = \frac{l}{v_l}, \tag{10}$$

where l is the interelectrode distance.

Thus, there is a competition of two discharges, which are developed in the liquid and solid dielectrics. A comparison of their velocities shows that $v_l \sim 10^5$ cm/s [6] and $v_d \sim 10^6$ cm/s [1], so that $v_d \gg v_l$. Therefore, the penetration of the discharge into the solid dielectric begins at $t_d < t_l$ and the critical voltage ramp at the pulse front can be evaluated from the condition $t_d = t_l$. Equating the t_d and t_l values given by formulas (9) and (10) and taking into account relation (5), we obtain the formula

$$A_c = \frac{\pi j_0 r^2}{8\varepsilon_0 \varepsilon l} = \frac{\beta}{\varepsilon_0 \varepsilon}\sqrt{\frac{\lambda}{\kappa_0}}, \tag{11}$$

where $\beta = \pi^2 r^2/16hl$ is a geometric factor. Within the framework of the model adopted, the critical voltage

ramp A_c is independent of the velocities of discharge development in the solid and liquid dielectrics, but depends on the permittivity of the solid, the thermal properties of electrodes, the contact geometry, and the interelectrode distance. Let us estimate A_c in a system with copper cathode and $l = 1$ cm. For a dielectric with $\varepsilon = 2–10$ and a microprotrusion with $r = (1–3) \times 10^{-5}$ cm, formula (11) yields $A_c = 10^{10}–10^{11}$ V/s, which is in agreement with the experimental values reported in [2].

In conclusion, it should be noted that electric microexplosions analogous to those described above for the cathode can also take place on the anode. Accordingly, the anode may also feature a discharge in the liquid dielectric over the solid surface, a displacement current related to the dynamic capacitance, and a large energy density in a microprotrusion on the metal electrode surface. As a result, the microprotrusion will exhibit electric explosion with the formation of a thin plasma jet. This jet will penetrate into the solid dielectric and initiate a discharge from the anode side. At the same time, the surface discharge plasma will spread in the liquid over the solid surface from anode to cathode so as to close the discharge circuit between electrodes. Therefore, both discharge plasma flows on the dielectric surface accelerate the shortage of electrodes. This phenomenon has been visually observed in investigations of the Vorob'evs effect [2].

Acknowledgments. This study was supported by the Russian Foundation for Basic Research, project no. 05-02-08240-ofi_a.

REFERENCES

1. A. A. Vorob'ev and G. A. Vorob'ev, *Electric Breakdown and Fracture of Solid Dielectrics* (Vysshaya Shkola, Moscow, 1966) [in Russian].
2. B. V. Semkin, A. F. Usov, and V. I. Kurets, *Principles of Electric Pulse Erosion of Materials* (Nauka, St. Petersburg, 1995) [in Russian].
3. G. A. Mesyats, Pis'ma Zh. Éksp. Teor. Fiz. **57** (2), 88 (1993) [JETP Lett. **57**, 95 (1993)].
4. G. A. Mesyats, *Ectons in Vacuum Discharge: Breakdown, Spark, and Arc* (Nauka, Moscow, 2000) [in Russian].
5. G. A. Mesyats, Dokl. Akad. Nauk **336**, 610 (1994) [Phys. Dokl. **39**, 417 (1994)].
6. V. Ya. Ushakov, *Electric Pulse Breakdown of Liquids* (Tomsk. Gos. Univ., Tomsk, 1975) [in Russian].
7. V. A. Govorkov, *Electric and Magnetic Fields* (Énergiya, Moscow, 1968) [in Russian].

Translated by P. Pozdeev

Technical Physics Letters, Vol. 31, No. 12, 2005, pp. 1065–1067. Translated from Pis'ma v Zhurnal Tekhnicheskoĭ Fiziki, Vol. 31, No. 24, 2005, pp. 60–66.

Calculating Levitation Forces in the Magnet–High-Temperature Superconductor Systems

Yu. S. Ermolaev and I. A. Rudnev

Moscow Engineering Physics Institute (State University), Moscow, 115409 Russia

Received May 4, 2005

Abstract—A new method of calculation of the magnetic levitation force in the permanent magnet–high-temperature superconductor systems is proposed based on the Maxwell equations and the Bean model. The dependences of the levitation force on the gap width calculated for various regimes of superconductor cooling are in satisfactory agreement with experimental data. © *2005 Pleiades Publishing, Inc.*

In recent years, increasing effort has been devoted to the development of devices employing the phenomenon of magnetic levitation [1]. The promising applications of magnetic levitation in systems of the permanent magnet–bulk high-temperature superconductor (PM–HTSC) type include magnetic bearings, flywheel energy storage systems, and magnetically levitated (maglev) trains [1–4]. For designing such systems, it is necessary to develop methods for the preliminary evaluation of the magnetic levitation force at a selected geometry of the PM–HTSC system. Even more important are the preliminary calculations aimed at optimization of the shape and volume of the HTSC unit, proceeding from a preset value of the levitation force. This optimization can significantly reduce the weight, size, and cost of each particular device.

This Letter describes a new approach to the calculation of magnetic levitation forces, current distributions, and spatial profiles of the magnetic field in PM–HTSC systems, which is based on the finite-element method. Using the proposed approach—in contrast, for example, to that described in [5]—it is possible to simulate both the process of zero-field cooling (ZFC) and the regime of cooling in a magnetic field (field cooling, FC) that is used in practice. Moreover, in some cases, our method is advantageous to those based on dynamical system modeling, such as that described, for example, in [6]. Indeed, the calculation of maximum forces using the proposed approach requires the calculations to be performed only for one or two points of the magnetic prehistory, whereas dynamical modeling [6] requires a detailed calculation of the entire magnetic prehistory of a given system.

In order to calculate the magnetic levitation force acting upon a given object (permanent or superconducting magnet), it is necessary to know the spatial distribution of the magnetic field and current in this object. The relationship between the current density **j** and magnetic field can be described in terms of the vector potential **A** using the Maxwell equation:

$$\mathrm{rot}\left(\frac{1}{\mu}\mathrm{rot}\mathbf{A}\right) = \mu_0\mathbf{j}, \tag{1}$$

where $\mu_0 = 4\pi \times 10^{-7}$ H/m is a magnetic constant and μ is the magnetic permeability (the latter quantity is required for ferromagnets; in our case, $\mu = 1$). Equation (1) can be used both for calculating the vector potential for a given current density distribution and for determining currents from the known vector potential.

Using the vector potential, the magnetic field is calculated as

$$\mathbf{B} = \mathrm{rot}\mathbf{A}. \tag{2}$$

Then, the magnetic levitation force is determined by integrating the product of the current density and field over the object volume:

$$\mathbf{F} = \int_v [\mathbf{jB}]dv. \tag{3}$$

If the current density vector in a given superconductor has more than one nonzero component, this relation has to be supplemented by additional conditions for the vector potential on the superconductor surface (including the condition of continuity for the current).

The field of a permanent magnet can be represented as the field of a solenoid with a current passing along the side surface [7]. Then, the magnet contribution to the vector potential can be calculated using Eq. (1). This approach provides the simplest way to calculate the force acting upon the magnet and is very useful when the levitation system includes several magnets.

The approach to the modeling of the ideal superconductor (ideal diamagnetic superconductor in the case of ZFC) is as follows. In order to calculate the current den-

1063-7850/05/3112-1065$26.00

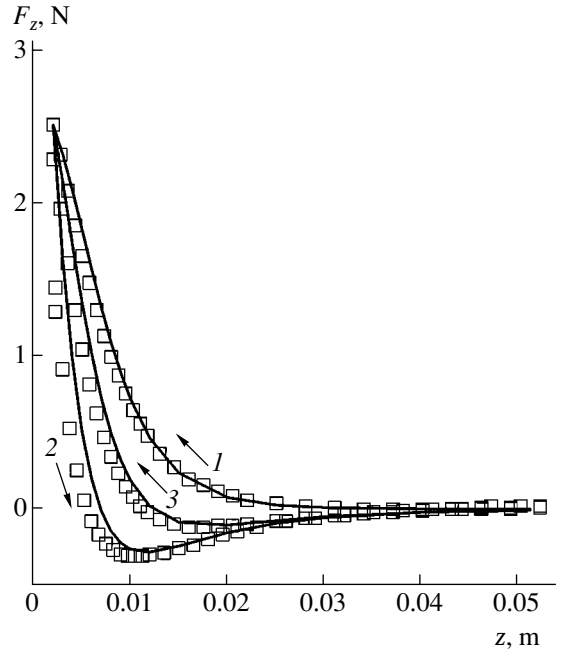

Fig. 1. A comparison of the calculated (curves) and measured (squares) dependences of the magnetic levitation force F_z on the PM–HTSC gap width z in a cylindrically symmetric system refrigerated in the ZFC regime. Arrows indicate the direction of the PM motion relative to the HTSC: (*1*) first approach to the minimum distance; (*2*) subsequent increase in the gap; (*3*) second approach. In the course of repeated cycles, the levitation force follows curves *2* and *3*.

sity distribution in this case, we assume that the vector potential in the volume remains unchanged. Using this condition and taking into account the contribution of the permanent magnet to the potential, we can calculate the distribution of the vector potential. Then, expressing currents via Eq. (1) and writing this expression for the superconductor volume, we obtain the distribution of currents in the superconductor. Finally, the levitation force is calculated using Eqs. (2) and (3) with these distributions of the vector potential and current density.

Let us consider a more realistic case of a superconductor within the framework of the Bean model [8] of the critical state. This model is well applicable to HTSCs of the second type with strong pinning, such as the monodomain $YBa_2Cu_3O_{7-x}$ ceramic superconductors usually employed in magnetic levitation systems. The Bean model postulates that a superconductor bears either a zero current or a nonzero current of the constant critical density j_c. The algorithm according to the Bean model is as follows. First, the vector potential is calculated using the procedure outlined above for the ideal superconductor and, then, the values of currents are corrected by limiting on the j_c level. Then, the vector potential is recalculated at the points where the current was corrected. This procedure of current correction and vector potential recalculation is repeated until the current at all points will not exceed j_c.

The initial distribution of the vector potential in the superconductor depends on the regime of refrigeration: in the ZFC regime, this potential is zero, whereas in the FC regime, the superconductor memorizes the initial vector potential distribution.

In most practical cases, the geometry of magnetic levitation systems is cylindrically symmetric. The typical example is a system of coaxial PM and HTSC. In this configuration, it is convenient to pass to a cylindrical coordinate system (r, φ, z), whereby some vector components will be identically zero: $\mathbf{A} = (0, A_\varphi, 0)$; $\mathbf{B} = (B_r 0, B_z)$; $\mathbf{j} = (0, j_\varphi, 0)$; and $\mathbf{F} = (0, 0, F_z)$. Then, Eqs. (1)–(3) acquire the following form:

$$-\frac{A_\varphi}{r^2} + \frac{\partial^2 A_\varphi}{\partial z^2} + \frac{1}{r}\frac{\partial A_\varphi}{\partial r} + \frac{\partial^2 A_\varphi}{\partial r^2} = -\mu_0 j_\varphi, \qquad (4)$$

$$B_r = -\frac{\partial A_\varphi}{\partial z} \qquad (5)$$

(the expression for B_z is omitted, since this component is of no significance), and

$$F_z = 2\pi \int_0^{ZR}\int_0 j_\varphi(r_1, z_1) B_r(r_1, z_1) r_1 dr_1 dz_1, \qquad (6)$$

where Z and R are the object thickness and radius, respectively. The boundary conditions on the axis of symmetry are as follows: $A_\varphi(r = 0) = 0$ and $B_r(r = 0) = 0$.

In this way, the initial problem reduces to determining the spatial distribution of A_φ from Eq. (4) in the (r, z) coordinates for the given boundary conditions in the bulk of superconductor, preset currents, and $A_\varphi = 0$ at the infinity. Then, the half-plane ($r > 0$, z) is divided into a discrete set of finite elements, and the derivatives entering into Eq. (4) are replaced at each node of the lattice by the difference relations. This yields a system of linear algebraic equations, which can be solved using the Seidel method.

In the case of systems (such as magnet–magnet and magnet–ideal paramagnet) that can be readily calculated using analytical methods, the proposed finite-difference method yields coinciding results to within two decimal digits at a quite acceptable computational time.

The performance of the proposed approach is illustrated in Figs. 1 and 2, which show a comparison of the results of calculations and experiment for the ZFC and FC regimes. The measurements were performed in a coaxial PM–HTSC system in a special experimental setup described previously [9], for a magnet with a diameter of 25 mm, a thickness of 13 mm, and a maximum field of 0.31 T on the axis (that corresponded to a surface current of 7×10^5 A/m). The HTSC was a

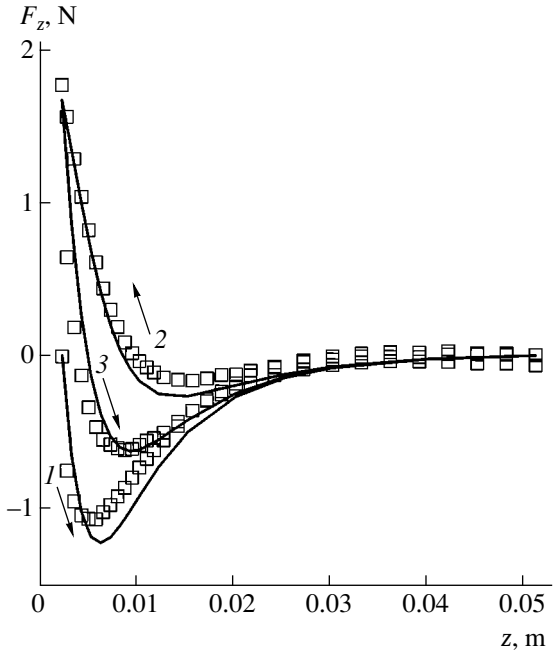

Fig. 2. A comparison of the calculated (curves) and measured (squares) dependences of the magnetic levitation force F_z on the PM–HTSC gap z in a cylindrically symmetric system refrigerated in the FC regime. Arrows indicate the direction of the PM motion relative to the HTSC: (*1*) first approach to the minimum distance; (*2*) subsequent increase in the gap; (*3*) second approach. In the course of repeated cycles, the levitation force follows curves *2* and *3*.

fusion-textured $YBa_2Cu_3O_{7-x}$ ceramic disk with a diameter of 14 mm and a thickness of 2 mm.

As can be seen, despite certain deviations in the range of small levitation gaps, the proposed approach provides for a quite good quantitative coincidence of the calculated and measured curves and, in particular, adequately describes the hysteresis behavior of the magnetic levitation force. The discrepancies can be related both to methodological factors and to experimental uncertainties, including roughness of the Bean model, inhomogeneity and defectness of materials, and measurement errors.

In conclusion, we have developed and verified a new method for calculations of the magnetic levitation force and the distributions of current and magnetic fields in a symmetrically symmetric PM–HTSC system. The results of model calculations show both qualitative and quantitative coincidence with experiment, which confirms the possibility of using the new method for the analysis of magnetic levitation systems using bulk HTSCs, such as magnetic bearings, flywheels, and maglev transport systems.

Acknowledgments. This study was supported by the Ministry of Education and Science of the Russian Federation, project no. A04-2.9-150.

REFERENCES

1. J. R. Hull, Supercond. Sci. Technol. **13**, R1 (2000).
2. N. Koshizuka, F. Ishikawa, H. Nasu, *et al.*, Physica C **378** (2002).
3. S. Nagaya, K. Komura, N. Kashima, *et al.*, Physica C **392**–**396**, 719 (2003).
4. H. Fujimoto, Supercond. Sci. Technol. **13**, 827 (2000).
5. Y.-D. Chun, Y.-H. Kim, J. Lee, *et al.*, IEEE Trans. Appl. Supercond. **11**, 2000 (2001).
6. M. J. Qin, G. Li, H. K. Liu, *et al.*, Phys. Rev. B **66**, 024516 (2002).
7. A. A. Kordyuk, V. V. Nemoshkalenko, R. V. Viznichenko, *et al.*, Appl. Phys. Lett. **75**, 1595 (1999).
8. C. P. Bean, Phys. Rev. Lett. **8**, 250 (1962); Rev. Mod. Phys. **36**, 31 (1964).
9. Yu. S. Ermolaev and I. A. Rudnev, Prib. Tekh. Éksp., No. 1, 164 (2004).

Translated by P. Pozdeev

Technical Physics Letters, Vol. 31, No. 12, 2005, pp. 1068–1070. Translated from Pis'ma v Zhurnal Tekhnicheskoĭ Fiziki, Vol. 31, No. 24, 2005, pp. 67–73.

Studying the Electric Conductivity of the Si(100)$c(4 \times 12)$–Al Surface Phase during Deposition of Indium and Aluminum

M. V. Lavrinaitis, D. V. Gruznev, D. A. Tsukanov, and S. V. Ryzhkov*

Institute of Automation and Control Processes, Far East Division of the Russian Academy of Sciences, Vladivostok, Russia

** e-mail: ryzhkov@iacp.dvo.ru*

Received June 15, 2005

Abstract—The dependence of the electric conductivity of the Si(100)$c(4 \times 12)$–Al surface phase on the surface morphology has been studied using low-energy electron diffraction, scanning tunneling microscopy, and four-point probe conductivity measurement techniques in the course of the vacuum deposition of In and Al. The growth of adsorbate islands acting as additional centers of charge carrier scattering leads to a decrease in the conductivity. © *2005 Pleiades Publishing, Inc.*

In recent years, much attention has been devoted to studying the relationship between the electric conductivity of surface phases and their crystal structure. Previous experimental data showed that the surface phases and ultrathin adsorbed films formed on the surface of single crystal silicon significantly influence the electric properties of samples [1–4].

This Letter presents the results of our investigation into correlated changes in the conductivity and morphology of the Si(100)$c(4 \times 12)$–Al surface phase in the course of the deposition of submonolayer indium and aluminum films, which were characterized by low-energy electron diffraction (LEED), scanning tunneling microscopy (STM), and four-point probe conductivity measurement techniques. The given surface phase comprises rows of Al clusters arranged along the $\langle 011 \rangle$ crystallographic direction and separated by zigzag trenches [5–7]. The aluminum coverage in the initial Si(100)$c(4 \times 12)$–Al surface phase amounts to 0.5 monolayer (ML) [1-ML coverage corresponds to the number density of atoms in the uppermost layer of the nonreconstructed Si(100) crystal face, that is, to 6.8×10^{14} cm^{-2}]. The aim of this study was to determine the effect of adsorbate islands acting as additional surface defects on the electric conductivity of the given surface phase. The Si(100)$c(4 \times 12)$–Al surface phase was selected for the investigation because this phase is characterized by a relatively high conductivity, accounting for up to 25% of the total conductivity of a sample [8], whereas the contributions of surface phases to the conductivity in Au/Si, Ag/Si, In/Si, and Na/Si systems amount to less than 10% [9–11]. Therefore, it might be expected that correlated changes in the conductivity and surface morphology for the selected system will be more pronounced.

The experiments were performed in an ultrahigh-vacuum (UHV) setup with a residual pressure of 5×10^{-10} Torr, which was equipped with a LEED attachment and a device for the conductivity measurements using the four-point-probe technique. The samples were prepared on phosphorus-doped *n*-Si(100) substrates with dimensions $15 \times 5 \times 0.5$ mm and a resistivity of 20 Ω cm. Prior to introduction into the UHV chamber, the samples were rinsed in organic solvents. The final cleaning was effected in vacuum by short-term annealing at 1550 K. The thus pretreated samples exhibited a clear 2×1 LEED pattern characteristic of the atomically clean Si(100) crystal surface. The sample surface structure and morphology was also studied by STM using an instrument of the Omicron Company.

The initial Si(100)$c(4 \times 12)$–Al surface phase was formed under UHV conditions by depositing aluminum to an 0.5-ML coverage onto the Si(100)2×1 substrate surface. The deposition was performed at room temperature and was followed by annealing at 950 K. Then, indium and aluminum were gradually (by controlled portions) deposited onto the samples. Indium was evaporated from a tantalum cell; aluminum was evaporated from a resistance-heated Al-coated tungsten filament. The rate of deposition for both adsorbates was 0.1 ML/min. The electric conductivity of a sample was measured *in situ* using the four-point probe technique, whereby a direct current in the range from 10 to 100 μA was passed between the probes spaced by 1.3 mm.

Figure 1 (curves *1* and *1'*) shows plots of the change $\Delta\sigma$ of the conductivity of the Si(100)$c(4 \times 12)$–Al surface phase versus coverage d of In deposited at room temperature. As can be seen, the conductivity exhibits a sharp drop in the very early stage of In deposition (curve *1*), reaching a level ($\Delta\sigma = 0$) characteristic of the

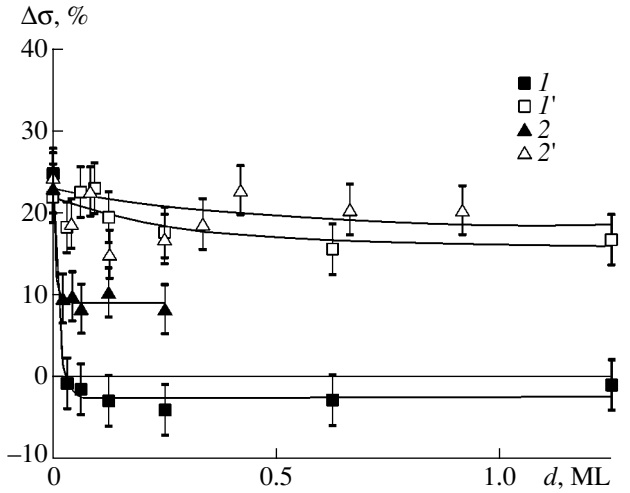

Fig. 1. Plots of the change $\Delta\sigma$ of the conductivity of the Si(100)$c(4 \times 12)$–Al surface phase versus coverage d of (*1*, *1*') In and (*2*, *2*') Al deposited at 300 K for the samples measured (*1*, *2*) before and (*1*', *2*') after vacuum annealing at 700 K [zero level ($\Delta\sigma = 0$) corresponds to the initial clean Si(100)2×1 surface].

initial clean Si(100)2×1 surface. However, the decrease in the conductivity was much less pronounced if the deposition of indium was followed by vacuum annealing of the sample at 700 K (curve *1*'). The results of the STM investigations of the In/Si(100)$c(4 \times 12)$–Al surface (Fig. 2a) showed that room-temperature deposition of In led to the appearance of a high concentration ($\sim 5 \times 10^{11}$ cm^{-2}) of three-dimensional (3D) indium islands on the sample surface. The islands were formed both at the surface steps and on the terraces (Fig. 2b). Upon the subsequent annealing at 400 K, the number of islands decreased to $\sim 1 \times 10^{11}$ cm^{-2} and the remaining islands were arranged predominantly at the steps (Fig. 2c). It should be noted that the STM investigation was performed upon the annealing at 400 K, whereas the conductivity was measured after the annealing at 700 K. It can be expected that the mass transfer in the latter case is more intense and, hence, the number of 3D adsorbate islands on the terraces must be still lower.

The variation of conductivity was analyzed using a model system comprising a Si(100) substrate with a $c(4 \times 12)$–Al surface phase and the 3D adsorbate islands that played the role of additional centers of charge carrier scattering. It was assumed that only the change in the scattering from islands contributes to the conductivity variations. Other scattering mechanisms cannot provide for comparable contributions, since the measurements in both cases (before and after annealing) were performed at the same (room) temperature. The contribution of surface steps to the charge carrier mobility was also ignored: we assumed this contribution to be the same for the sample before and after annealing at 700 K, since this temperature is insufficiently high to produce a significant rearrangement of steps on the sample surface.

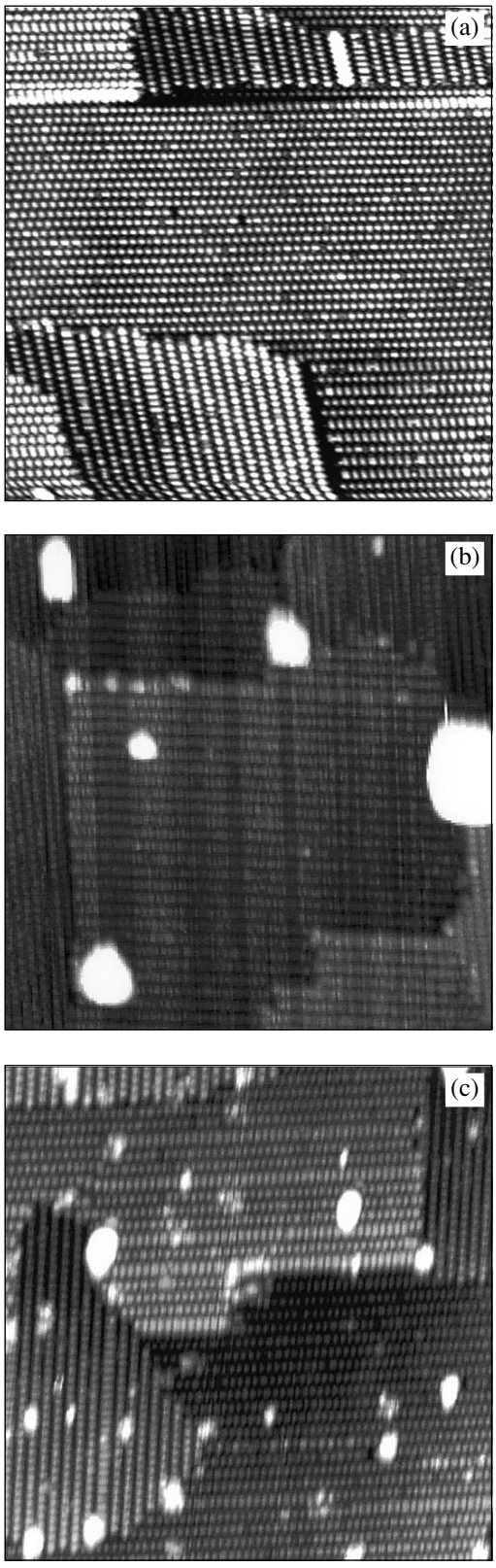

Fig. 2. STM images (100×100 nm) of Si(100) substrates in the filled (2V) state with the Si(100)$c(4 \times 12)$–Al surface phase (a) in the initial state, (b) upon deposition of 0.1 ML of indium at room temperature, and (c) after the subsequent heating of the sample to 400 K.

The total conductivity of a sample was defined as $\sigma = \sigma_1 + \sigma_2$, where σ_1 is the conductivity of a bulk substrate and σ_2 is a contribution due to the surface phase. As is well known, the *n*-type conductivity can be expressed as $\sigma = en\mu$, where e, n, and μ are the electron charge, density, and mobility, respectively [12]. In the case of scattering on neutral centers, the electron mobility can be determined using the formula $\mu = T^k me^3/20\varepsilon h^3 N_0$ [13], where T is the temperature, k is a constant, m is the electron mass, ε is the permittivity, $\hbar$ is the Planck constant, and N_0 is the concentration of neutral scattering centers. According to this formula, the experimentally measured conductivity is inversely proportional to the concentration of scattering centers.

In agreement with the above model, Fig. 1 shows that the conductivity of the (0.1 ML In)/$c(4 \times 12)$–Al system with a higher concentration of islands (after In deposition at room temperature) is lower than that observed upon a decrease in the number of islands caused by the annealing at 700 K. However, it should be noted that, although the concentration of islands upon annealing was decreased by a factor of about five, the conductivity increased only by about 20% to become equal to a value for the clean Si(100)2×1 sample surface. As is known, the 2×1 surface phase does not practically influence (with less than 1% contribution for a 20-nm-thick sample) the conductivity of a crystal substrate [14]. Therefore, the results of conductivity measurements in this case refer predominantly to the bulk component.

Thus, the obtained experimental data show that the formation of In islands on the $c(4 \times 12)$–Al surface phase leads to a sharp decrease in the conductivity of the surface layer (down to a level comparable with the bulk value) because of the increased scattering of free electrons on the grown islands. After the subsequent annealing of the In/Si(100)$c(4 \times 12)$–Al sample, the number of In islands decreases and this scattering component no longer plays a significant role.

In the experiments with aluminum deposition at room temperature onto the Si(100)$c(4 \times 12)$–Al surface phase, the conductivity of samples also exhibited a decrease in the initial stage of increase in the coverage (Fig. 1, curve *2*). As is known, the growth of aluminum layer on the Si(100)$c(4 \times 12)$–Al surface also has an island character [15] (analogous to that in the case of indium deposition) and the concentration of Al islands is about 1×10^{12} cm^{-2}. Although the concentration of islands formed during deposition at room temperature is greater for Al than for In, the conductivity of samples with the same surface coverage is somewhat higher in the former case. This is probably related to the fact that deposited Al atoms form regular crystalline grains [16] rather than shapeless 3D islands (such as in the case of indium). After the annealing at 700 K, the concentration of Al islands decreases to about 2×10^{10} cm^{-2} and the sample conductivity increases (similarly to the case with annealing upon indium deposition) up to a level comparable with the conductivity of the initial $c(4 \times 12)$–Al surface phase (Fig. 1, curve *2*').

To summarize, the experimental results show that the deposition of In and Al onto the Si(100)$c(4 \times 12)$–Al surface phase leads to the formation of adsorbate islands that act as the centers of charge carrier scattering and decrease the conductivity of samples. Subsequent annealing of the samples with deposited indium and aluminum induces mass transfer, whereby the adsorbed metal atoms are rearranged to form islands of greater sizes, which leads to a decrease in the concentration of scattering centers and the corresponding increase in the conductivity.

Acknowledgments. This study was supported by the Russian Foundation for Basic Research (project nos. 04-02-08242 and 05-02-17823), the program "Universities of Russia" (project no. UR 01.01.052), and the Presidential Program of Support for Leading Scientific Schools in Russia (project no. NSh-1369.2003.02).

REFERENCES

1. F. Bauerle, W. Monch, and M. Henzler, J. Appl. Phys. **43**, 3917 (1972).
2. K. R. Kimberlin and M. C. Tringides, J. Vac. Sci. Technol. A **13**, 462 (1995).
3. S. Hasegawa, X. Tong, S. Takeda, *et al.*, Prog. Surf. Sci. **60**, 89 (1999).
4. D. A. Tsukanov, S. V. Ryzhkov, S. Hasegawa, *et al.*, Phys. Low-Dim. Struct. **7**–**8**, 149 (1999).
5. N. Shimizu, H. Kitada, and O. Ueda, Phys. Rev. B **51**, 5550 (1995).
6. N. Shimizu, H. Kitada, and O. Ueda, J. Cryst. Growth **150**, 1159 (1995).
7. Y. Oshima, T. Hirata, T. Yokoyama, *et al.*, Surf. Sci. **465**, 81 (2000).
8. S. V. Ryzhkov, T. Nagao, V. G. Lifshits, *et al.*, in *Proceedings of the WE-Heraeus-Seminar on 2D Conductivity in Surfaces States and Monolayers, Bad Honnef, 2001*.
9. D. A. Tsukanov, S. V. Ryzhkov, D. V. Gruznev, *et al.*, Appl. Surf. Sci. **162**–**163**, 168 (2000).
10. C.-S. Jiang, S. Hasegawa, and S. Ino, Phys. Rev. B **54**, 10389 (1996).
11. S. V. Ryzhkov, D. A. Tsukanov, D. V. Gruznev, *et al.*, Phys. Low-Dimens. Semicond. Struct. **7**–**8**, 7 (1999).
12. C. Kittel, *Introduction to Solid State Physics* (Wiley, New York, 1976; Nauka, Moscow, 1978).
13. V. L. Bonch-Bruevich and S. G. Kalashnikov, *Physics of Semiconductors* (Nauka, Moscow, 1977) [in Russian].
14. K. Yoo and H. H. Weitering, Surf. Sci. **482**–**485**, 482 (2001).
15. S. Itou, A. Nishida, Y. Murata, *et al.*, Surf. Sci. **565**, 121 (2004).
16. S. Itou, O. Kubo, N. Yamaoka, *et al.*, Jpn. J. Appl. Phys. **42**, L432 (2003).

Translated by P. Pozdeev

Technical Physics Letters, Vol. 31, No. 12, 2005, pp. 1071–1073. Translated from Pis'ma v Zhurnal Tekhnicheskoĭ Fiziki, Vol. 31, No. 24, 2005, pp. 74–80.

Absolute Cross Sections for the Electron-Impact Formation of Cytosine Anions

M. I. Shafranyosh, M. I. Sukhoviya, L. L. Shimon, and I. I. Shafranyosh

Uzhgorod National University, Uzhgorod, Ukraine

e-mail: mshafr@tns.uz.ua

Received April 13, 2005; in final form, August 18, 2005

Abstract—The process of negative ion formation by electron impact on cytosine (a nitrous base of nucleic acids) has been studied in crossed molecular and electron beams for electron energies in the interval from 0.4 to 5.0 eV. Using a specially developed method, the molecular beam intensity was determined and the energy dependence of the absolute cross section Q for the formation of cytosine anions was studied. The maximum ionization cross section $\sigma = 4.2 \times 10^{-18}$ cm^2 was observed for an electron energy of 1.5 eV. © *2005 Pleiades Publishing, Inc.*

A high-energy particle penetrating in a solid generates a large number of secondary electrons, predominantly with small energies. According to the existing notions [1], such low-energy electrons mostly account for destructive changes in biological structures on a molecular level, their main targets being genetic macromolecules. The results of our previous experiments [2–5] showed that the electron impact on heterocyclic fragments of such macromolecules induces various physical processes, including excitation, ionization, dissociative excitation, and dissociative ionization.

In recent years, much attention of researchers has been devoted to the resonance phenomena accompanying the interactions of electrons with molecules. It has been established, in particular, that electron impact beginning with almost zero energy leads to the formation of negative molecular ions (anions) [6–8] that give rise to a new cascade of physicochemical reactions. In order to provide a quantitative description of such processes, it is necessary to know their main characteristics—namely, the absolute ionization cross sections.

Reliable data on the ionization cross sections of molecules can be obtained only in high-precision physical experiments, in which the influence of the ambient medium is reduced practically to zero. This approach has been implemented in our investigation using modern equipment and the method of crossed molecular and electron beams. This study was stimulated by the fact that no such experiments have been reported so far.

Experimental setup. The experiments were performed in a setup with crossed electron and molecular beams, which is schematically depicted in Fig. 1. A beam of cytosine molecules was produced by a multichannel thermal effusion source. Cytosine, a nitrous base of nucleic acids, was obtained from the Sigma–Aldrich company (USA). The molecules traveled through the region of interaction with electrons and reached a collector, where a significant amount of cytosine was deposited with time in the form of a condensed spot. The size of this spot was used to determine the molecular beam geometry (beam cross section area, angular aperture), while the weight of the deposit provided an estimate of the molecular beam intensity. The collector was cooled by liquid nitrogen, and its entrance slit S_4 could be blocked with the aid of a shutter.

The electron beam was generated by a five-electrode gun with tungsten cathode, which was described in

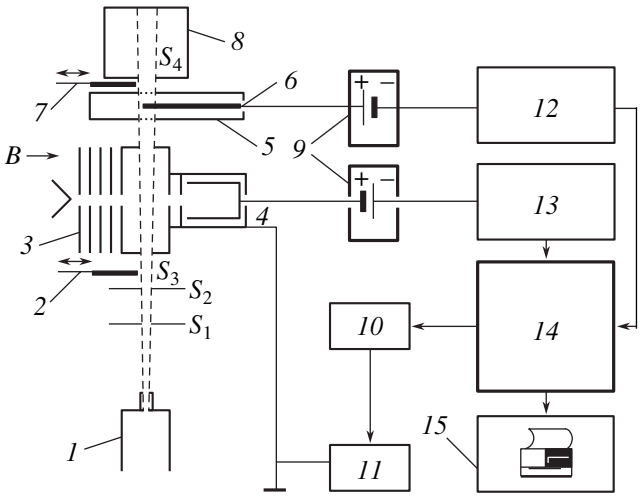

Fig. 1. Schematic diagram of the experimental setup: (*1*) molecular beam source; (*2*, *7*) shutters; (S_1, S_2, S_3, S_4) collimating slits; (*3*) electron gun; (*4*) electron collector; (*5*) ion collector; (*6*) probe; (*7*) ion collector; (*8*) molecular beam collector; (*9*) bias voltage sources; (*10*) digital-to-analog converter; (*11*) voltage amplifier; (*12*) electrometric amplifier; (*13*) electron beam current–frequency (*I–f*) converter; (*14*) personal computer with PIO 3232 interface board; (*15*) printer.

1063-7850/05/3112-1071$26.00 © 2005 Pleiades Publishing, Inc.

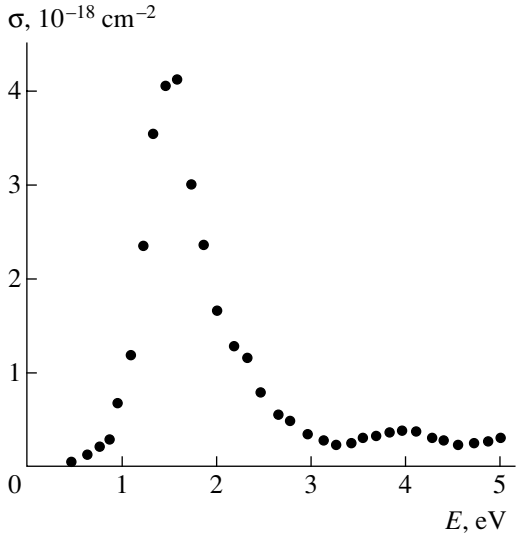

Fig. 2. A plot of the absolute cross section for cytosine anion formation versus electron energy.

more detail elsewhere [9]. The first electrode of the electron gun occurred at a small negative potential, which blocked the ejection of low-energy electrons from the cathode. The electron beam passed through the region of interaction with molecules and struck the electron collector. The measurements were performed for an electron beam current of $\sim 1 \times 10^{-6}$ A, the electron energy varied within 0.4–5.0 eV, and an energy spread of $\Delta E_{1/2} \sim 0.3$ eV (FWHM). The electron energy scale was calibrated relative to the SF_6 resonance peak (whose energy position was set to be zero). The complete collection of ions formed in the region of interaction of the crossed molecular and electron beams was ensured by a transmission collector [10] with an axial probing electrode occurring at a potential of +25 V. The electron gun was operating in a longitudinal magnetic field of $B \sim 1.2 \times 10^{-2}$ T, which prevented the collection of electrons scattered from cytosine molecules and electrode surfaces.

The system of data acquisition and measurement process control comprised an electrometric amplifier of the ion current, electron beam current–frequency (*I–f*) converter, stepwise electron-accelerating potential sweep system (involving a digital-to-analog (DAC) converter and a voltage amplifier), a personal computer with parallel input/output interface board (PIO 34232), and a printer. This system could operate in the regimes of measurement of (i) the ion and electron beam currents at a fixed electron beam energy (for determining the absolute cross section) and (ii) the ion to electron beam current ratio during stepwise electron beam energy variation (for determining the energy dependence of the ionization cross section). The experiments were performed at a residual pressure of $\sim 1 \times 10^{-5}$ Pa.

Method of investigation. The measurements were performed using a three-stage procedure. In the first (control) stage, the collision chamber was filled with SF_6 (via an SNA-2 gas inlet system) to a pressure of 1.3×10^{-3} Pa. Then, the electron gun was switched on and a resonance peak corresponding to the SF_6^- ion formation was detected. The energy position of this resonance was used to calibrate the electron energy scale, and the full width at half maximum (WFHM) was used to estimate the electron energy spread $\Delta E_{1/2}$ in the beam.

In the second stage, the collision chamber was evacuated to a residual pressure of 1×10^{-5} Pa, after which the molecular beam was switched on (shutter *2* was removed and shutter *7* set to block the beam) and the energy dependence of the cross section for cytosine anion formation was measured.

In the third stage, the absolute cross section σ for cytosine anion formation was determined. This quantity was defined as

$$\sigma = J_i / J_e n l, \quad (1)$$

where J_i and J_e are the currents of negative ions and electrons, respectively; n is the number density of molecules in the region of interaction of the molecular and electron beams; and l is the electron path length in the molecular beam. The J_i and J_e values were directly measured, l was evaluated from the molecular beam geometry, and n was determined using the following procedure. First, the molecular beam was blocked by shutters *2* and *7* and the temperature of the cytosine container was increased to the necessary level (not exceeding 430 K). Then, shutter *7* was removed for a preset period of time (with shutter *2* removed) and the ion (J_i) and electron (J_e) currents were measured at an electron energy of 1.5 eV. The time of cytosine condensation in a series of five experiments was varied within $(0.9–3.0) \times 10^3$ s. After termination of these experiments, the condensate was dissolved in distilled water, the UV absorption of this solution was measured, and the condensate mass M was determined from the optical absorption data. The M value is also related to the experimental parameters as

$$M = nSmvt, \quad (2)$$

where S is the area of the region of molecular and electron beam intersection, m is the molecular weight, v is the velocity of molecules in the beam, and t is the period of time for which shutter *7* was removed. The error of determining n was about 17%. The experiments were performed using the beam of cytosine molecules with a concentration of $\sim 8 \times 10^{10}$ cm^{-3}.

Results and discussion. The results of our experiment showed that, using the approach described above, it is possible not only to detect negative ions of heterocyclic molecules (cytosine anions formed via electron impact ionization), but also to measure their absolute

concentration. Figure 2 shows the absolute cross section σ for cytosine anion formation by electron impact as a function of the electron energy. As can be seen, the most effective formation of cytosine anions takes pace in the interval of electron energies below 5 eV. Another important result is that the energy dependence of the cross section exhibits a clear resonance at an electron energy of 1.5 eV, where the maximum ionization cross section is 4.2×10^{-18} cm^2. The measured value of the absolute ionization cross section has a meaning of the total cross section, since it describes the cross section for the formation of anions of both the whole cytosine molecule and its fragments.

It should be noted that, according to the commonly accepted notions [11], the formation of a significant amount of negative ions from whole molecules (i.e., the formation of molecular anions) is unlikely at their small concentration. Indeed, the effective stabilization of molecular ions due to their collisions with particles of the third kind under such conditions cannot take place and, hence, the anion of the whole molecule occurring in an electronically or vibrationally excited state will unavoidably dissociate into neutral and charged fragments. In the region of low electron energies under consideration, the most probable neutral fragment is a hydrogen atom in the pyrimidine ring of cytosine molecule, which possesses the minimum binding energy. Therefore, the formation of cytosine anions proceeds in two stages according to the following scheme:

$$e^- + C_4H_5O \rightarrow [(C_4H_5N_3O)^-]^* \rightarrow (C_4H_4N_3O)^- + H.$$

However, this situation changes in the case of a large concentration of molecules, whose collisions most probably lead to the stabilization of negative ions of the whole molecules. Such conditions take place, for example, in irradiated cells of biological structures.

To summarize, we developed a method for the measurement of the intensity of a molecular beam. Using this method, we have experimentally determined for the first time the absolute cross section for the formation of cytosine anions under the conditions of electron impact at an electron energy of 0.4–5.0 eV. The maximum ionization cross section $\sigma = 4.2 \times 10^{-18}$ cm^2 is observed for an electron energy of 1.5 eV. It is established that the maximum contribution to the cross section of cytosine anion formation is due the dissociative ionization channel.

REFERENCES

1. C. Sonntag, *The Chemical Basis for Radiation Biology* (Taylor & Francis, London, 1987).
2. M. I. Sukhoviya and I. I. Shafran'osh, *Elementary Processes in Collisions of Atomic and Molecular Particles* (ChGU, Cheboksary, 1987), pp. 121–124 [in Russian].
3. M. I. Sukhoviya, V. N. Slavik, I. I. Shafranyosh, *et al.*, Biopolim. Kletka **7** (6), 77 (1991).
4. M. I. Sukhoviya, M. I. Shafranyosh, and I. I. Shafranyosh, in *Proceedings of the 8th Conference "Spectroscopy of Biological Molecules: New Directions," Enschede, 1999* (Kluwer, Dordrecht, 1999), pp. 281–282.
5. M. I. Sukhoviya, I. I. Shafranyosh, and L. L. Shimon, Vestn. Kharkov. Gos. Univ., Ser.: Biofiz. **434** (3), 39 (1999).
6. K. Aflatooni, G. A. Gallup, and P. D. Burrow, J. Phys. Chem. A **102**, 6205 (1998).
7. M. A. Huels, I. Hahdorf, E. Illenberger, and L. Sanche, J. Chem. Phys. **108**, 1309 (1998).
8. M. I. Sukhoviya, M. I. Shafranyosh, L. L. Shimon, *et al.*, in *Proceedings of the 23rd International Conference on Photonic Electronic and Atomic Collisions (ICPEAC), Stockholm, 2003*, p. Tu067.
9. I. I. Shafranyosh and V. I. Marushka, Pis'ma Zh. Tekh. Fiz. **29** (22), 16 (2003) [Tech. Phys. Lett. **29**, 930 (2003)].
10. I. I. Shafranyosh and M. O. Margitich, J. Phys. B **33**, 905 (2000).
11. H. S. W. Massey, *Negative Ions* (Cambridge Univ. Press, Cambridge, 1976).

Translated by P. Pozdeev

Technical Physics Letters, Vol. 31, No. 12, 2005, pp. 1074–1077. Translated from Pis'ma v Zhurnal Tekhnicheskoĭ Fiziki, Vol. 31, No. 24, 2005, pp. 81–87.

The Exact Finite Difference Method: A New Approach to the Calculation of Leak Modes in Multilayer Waveguide Structures

E. I. Golant

"ISTOK" State Unitary Enterprise, Fryazino, Moscow oblast, Russia

Received July 11, 2005

Abstract—A new approach to the calculation of electromagnetic modes in optical waveguides (OWGs), which is based on the exact finite difference method (EFDM) representing a combination of the finite difference method and the transmission matrix technique, is described. The efficacy of the EFDM is demonstrated in application to the calculation of leak modes in multilayer planar OWGs of the ARROW type, featuring antiresonance reflection from a multilayer shell (rather than the total internal reflection from the shell–core interface as in the usual OWGs). The proposed method can be used for calculations of both the electromagnetic modes in dielectric OWGs and the quantum states of electrons in multibarrier semiconductor heterostructures. The parameters of a nine-layer OWG calculated using the EFDM are compared to the published data obtained by solving a dispersion equation within the framework of the transmission matrix technique. The results of calculations of the spectrum of radiative losses for the first (leak) TE mode in planar OWGs with various numbers of layers are presented. © *2005 Pleiades Publishing, Inc.*

Introduction. The problem of determining guided modes in a multilayer planar optical waveguide (OWG) can be reduced to the solution of a stationary wave equation (Schrödinger equation) in a medium with a piecewise-constant (stepwise) profile of the refractive index (potential energy):

$$\frac{d^2\psi}{dx^2} + k_j^2\psi = 0, \qquad (1)$$

where $k_j = \sqrt{n_j^2 k_0^2 - \gamma^2}$ is the transverse wavevector of the jth section of the given OWG, n_j is the corresponding refractive index, $\gamma = \beta - i\alpha$ is the longitudinal (in the general case, complex) propagation constant of a wave running along the z axis with a phase factor of $\exp[i(\omega t - \gamma z)]$, $k_0 = \omega/c$ is the wavevector of the free space, ω is the circular frequency, c is the velocity of light in vacuum, and $\psi = E_y$ (for TE waves) or H_y (for TM waves).

The boundaries between layers with different refractive indices must obey the following matching conditions:

$$\psi(x_{j+}) = \psi(x_{j-}), \frac{1}{\mu_j}\frac{d\psi}{dx}\bigg|_{x_{j+}} = \frac{1}{\mu_{j-1}}\frac{d\psi}{dx}\bigg|_{x_{j-}}, \qquad (2)$$

where $\mu_j = 1$ for TE waves and $\mu_j = n_j^{-2}$ for TM waves; the signs "plus" and "minus" refer to the layers occurring on the positive and negative sides from the point j, respectively. It should be noted that, for electron waves in semiconductor heterostructures, we have $\mu_j = \frac{m_j^*}{m_0}$, where m_j^* is the effective mass of electron and m_0 is the free electron mass.

Let us consider an OWG bounded by half-spaces with the indices n_s and n_c, and the positive direction of the x axis corresponding to the passage from n_s to n_c. For $x_j \le x \le x_{j+1}$, the general solution of Eq. (1) can be written as

$$\begin{aligned}\psi(x) &= A_j\cos[k_j(x - x_j)] + B_j\sin[k_j(x - x_j)] \\ &= R_j e^{ik_j(x - x_j)} + S_j e^{-ik_j(x - x_j)}.\end{aligned} \qquad (3)$$

Using the conditions (2), it is possible to obtain explicit expressions for the coefficients of T_j matrices [1] relating the wave function ψ to the continuous quantity $\mu_j^{-1}\psi' = \mu_j^{-1}\frac{d\psi}{dx}$ in the adjacent OWG sections. A product of the T_j matrices yields the so-called transmission matrix $T = T_{N-1}\ldots T_2T_1 = \begin{bmatrix} t_{11} & t_{12} \\ t_{21} & t_{22} \end{bmatrix}$ that relates the wave function and its derivatives in the adjacent sections.

Let us assume that $\psi(x) = R_s e^{ik_s(x - x_1)}$ for $x < x_1$ and $\psi(x) = S_c e^{-ik_c(x - x_N)}$ for $x > x_N$, which implies that only

Comparative data on the mode characteristics of a nine-layer ARROW structure calculated using the proposed EFDM scheme and a standard method

	Present method		Reference [3]	
mode	β/k_0	α/k_0	β/k_0	α/k_0
TE_1	1.457920191	$0.0071059441 \times 10^{-4}$	1.457920191	$0.007106242 \times 10^{-4}$
TE_2	1.457791244	$0.0090529995 \times 10^{-4}$	1.457791244	$0.009053396 \times 10^{-4}$
TE_3	1.453780369	$0.1145698295 \times 10^{-4}$	1.453780369	$0.114698816 \times 10^{-4}$
TE_4	1.453045405	$0.4186909382 \times 10^{-4}$	1.453045406	$0.420121480 \times 10^{-4}$
TE_5	1.451864810	$0.6904035922 \times 10^{-4}$	1.451864807	$0.693651857 \times 10^{-4}$
TE_6	1.450269492	$0.7293545637 \times 10^{-4}$	1.450269491	$0.732515869 \times 10^{-4}$

Note: The calculations were performed for $n_s = 3.5$, $n_1 = 1.46$, $n_2 = 1.50$, $n_3 = 1.46$, $n_4 = 1.50$, $n_5 = 1.46$, $n_6 = 1.50$, $n_7 = 1.46$, $n_8 = 1.50$, $n_9 = 1.46$, $n_c = 1.0$, $d_1 = 2.0$ μm, $d_2 = 448$ μm, $d_3 = 4.0$ μm, $d_4 = 0.448$ μm, $d_5 = 2.0$ μm, $d_6 = 0.448$ μm, $d_7 = 4.0$ μm, $d_8 = 0.448$ μm, $d_9 = 2.0$ μm, $\lambda = 0.6328$ μm.

outgoing (and, for a real ik, decaying) waves exist in the boundary half-spaces. Then, we readily obtain the following dispersion equation for the longitudinal complex propagation constant γ:

$$\mu_c^{-1} ik_c t_{11} - \mu_s^{-1}\mu_c^{-1} k_s k_c t_{12} + t_{21} + \mu_c^{-1} ik_s t_{22} = 0. \quad (4)$$

The roots of this equation, $\gamma = \beta - i\alpha$, determine the real propagation constant β and the attenuation constant α for the OWG leak modes. With some insignificant modifications, the above approach is used in most of the known numerical calculations of modes in OWGs of the ARROW type, featuring antiresonance reflection from a multilayer shell (rather than the total internal reflection from the shell–core interface as in the usual OWGs).

Description of the new method and results. The approach described above encounters two main difficulties.

(i) The calculation of the complex coefficients of the T matrix as the direct product of T_j leads to the accumulation of rounding errors, and even a small distortion of the dispersion equation (4) leads to serious errors in the complex propagation constant. This behavior is qualitatively explained by the fact that the presence of exponentially growing components in the general solution of the initial differential equation impairs the computational robustness (for rigorous proof, see [2]).

(ii) Determination of the complex roots of the transcendental dispersion equation (4) involves extremely complicated computational procedures [1, 3].

Both these difficulties become even more significant when the number N of OWG layers is increased. On the other hand, the need for calculations of the OWGs as well as semiconductor heterostructures (e.g., for the quantum cascade lasers [4]) containing tens or even hundreds of layers becomes more urgent.

This Letter describes a new approach to the problem outlined above, according to which the explicit form of T_j matrices [1] is used for constructing a difference scheme that relates the values of the wave function ψ at the three sequential points (ψ_{j-1}, ψ_j, ψ_{j+1}):

$$\left[\mu_j^{-1}\frac{k_j d_j}{\sin(k_j d_j)}\left(\frac{\psi_{j+1}-\psi_j}{d_j}\right)\right.$$

$$\left. - \mu_{j-1}^{-1}\frac{k_{j-1} d_{j-1}}{\sin(k_{j-1} d_{j-1})}\left(\frac{\psi_j - \psi_{j-1}}{d_{j-1}}\right)\right]\frac{2}{d_j + d_{j-1}} \quad (5)$$

$$+ \left[\mu_j^{-1} k_j^2 \frac{\tan(k_j d_j/2)}{k_j d_j/2} + \mu_{j-1}^{-1} k_{j-1}^2 \frac{\tan(k_{j-1} d_{j-1}/2)}{k_{j-1} d_{j-1}/2}\right]\psi_j = 0,$$

where $d_j = x_{j+1} - x_j$ is the jth layer thickness.

The proposed scheme is typical of a stationary difference approximation of Eq. (1) with matching conditions (2). Moreover, scheme (5) in the limit of $\max(d_j) \longrightarrow 0$ transforms into the standard difference scheme of second-order accuracy for Eqs. (1) and (2). However, in contrast to the standard scheme, the proposed one is exact for the OWGs with stepwise transverse index profile. Upon selecting the appropriate boundary conditions for the system of equations (5), we obtain a closed system of N linear algebraic equations with N unknowns and a real symmetric tridiagonal matrix. An important advantage of scheme (5) is the possibility of using effective and robust numerical methods (in particular, the method described in [5]) developed for the solution of difference equations with tridiagonal matrices.

The obtained system of equations is solved assuming that the attenuation is absent ($\alpha = 0$) and the wave

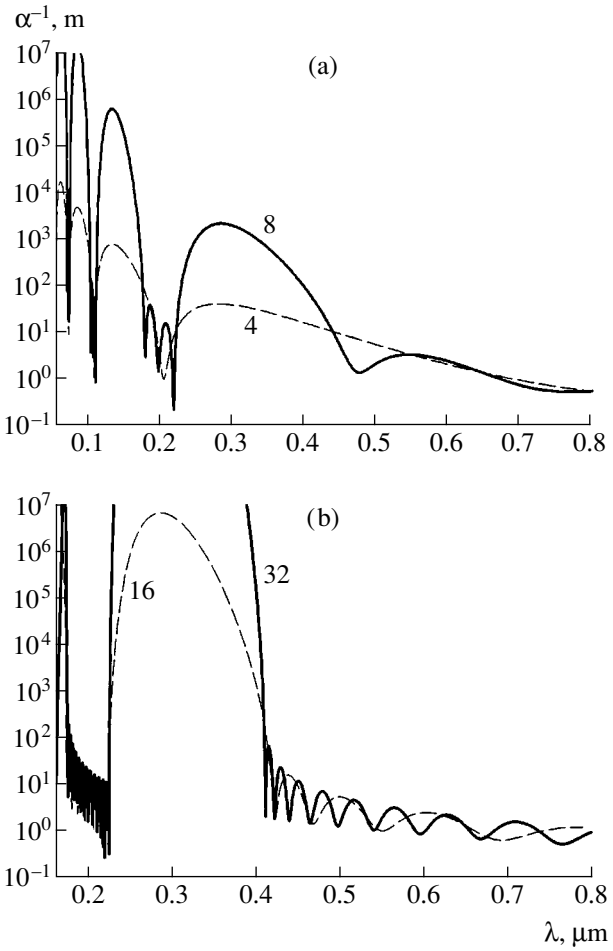

The characteristic attenuation length α^{-1} as a function of the light wavelength in the free space for the first (leak) TE mode of symmetric planar Bragg's waveguides comprising a 80-μm-thick core surrounded by a shell consisting of 0.323-μm-thick layers with alternating (1.50/1.46) refractive indices. Figures at the curves indicate the number of alternating pairs in the shell: (a) 4 and 8; (b) 16 and 32.

function ψ_N is real. The imaginary part α of the complex propagation constant, which is assumed to be small (for the calculation of long-lived modes), is determined in the next stage of the calculation. This is one of the main distinctive features of the proposed approach, whereby the calculations of the real and imaginary parts of the complex propagation constant are performed separately. As a result, the solution of Eqs. (5) for a preset longitudinal propagation constant β and real values of the wave function ψ_0 (or its derivative ψ_0') at the boundary (with the corresponding boundary conditions) yields real values of the wave function at all other points (sections) of the given OWG structure.

In this approach, it is implied that the OWG is supplied from outside (via one or both boundaries with the outer half-spaces) with electromagnetic energy that provides for the absence of attenuation of the propagating wave. The supplied power is evidently equal to that radiated by the wave into the outer space. Let us denote this power (per unit area of the radiating surface) by P_x, and the power transferred by the wave propagating inside the OWG in the z direction, by P_z (per unit length in the direction perpendicular the xz plane). The ratio of $P_x(\beta)/P_z(\beta) = \alpha$ has the meaning of the attenuation coefficient of the given mode, which is dependent on β. The minima in the $P_x(\beta)/P_z(\beta)$ ratio correspond to the most long-lived modes, for which the given OWG provides the most favorable conditions of antiresonance reflection from the ARROW shell. Using the values of the wave functions determined as described above, the $P_x(\beta)$ and $P_z(\beta)$ functions are analytically calculated in a closed form.

Thus, there are two substantial features that ensure the efficiency of the proposed approach: (i) use of the exact finite difference approximation and (ii) use of the new method (modified as compared to the known one [6]) for calculating the attenuation factor related to the radiative losses.

In order to evaluate the efficacy of the EFDM, the proposed scheme was used to calculate the first six TE modes for a nine-layer ARROW structure, which were previously calculated in [1] using complicated numerical methods involving the search for complex roots of dispersion equations (4). The comparative results are presented in the table. As can be seen from these data, the values of propagation constants (effective indices) obtained using the proposed method completely coincide (to within ten digits) with the solutions of a complex dispersion equation obtained in [3]. As for the radiative losses (attenuation coefficient), the agreement is (as expected) much worse: the data coincide to within 4–5 digits for the modes with low losses and to within 2–3 digits for the modes with relatively large losses. However, this accuracy of determination of the attenuation coefficient is sufficient in most practical applications. An increase in the relative accuracy with decreasing attenuation is explained by a resonance character of the interference of waves in the ARROW shell. Under such resonance conditions, the proposed method ensures a very good approximation for determining the radiated (lost) power, which is even more improved for sharper resonances (i.e., for more long-lived modes).

Another illustration of the possibilities of the proposed method is provided by data in the figure, which show the results of calculations of the characteristic attenuation length α^{-1} as a function of the light wavelength in the free space for the first (leak) TE mode of a planar Bragg's waveguide. The waveguide had a 80-μm-thick core and a shell consisting of 0.323-μm-thick layers with alternating (1.50/1.46) refractive indices. As can be seen, an increase in the number of layers

in the shell leads to the formation of transmission and quenching bands in the waveguide.

Acknowledgments. This study was supported by the Russian Foundation for Basic Research, project nos. 04-02-16441 and 04-02-17177.

REFERENCES

1. C. Chen, P. Berini, D. Feng, *et al.*, Opt. Express **7**, 260 (2000).
2. A. Mayer and J.-P. Vigneron, Phys. Rev. E **59**, 4659 (1999).
3. E. Anemogiannis, E. N. Glytsis, and T. K. Gaylord, J. Lightwave Technol. **17**, 929 (1999).
4. B. Kramer, Adv. Solid State Phys. **43**, 351 (2003).
5. E. I. Golant, A. A. Kal'fa, S. B. Poresh, and A. S. Tager, Élektron. Tekh., Ser. 1: Élektronika SVCh, No. 7, 23 (1981).
6. W. P. Huang, R. M. Shubair, A. Nathan, and Y. L. Chow, J. Lightwave Technol. **10**, 1015 (1992).

Translated by P. Pozdeev

Technical Physics Letters, Vol. 31, No. 12, 2005, pp. 1078–1081. Translated from Pis'ma v Zhurnal Tekhnicheskoĭ Fiziki, Vol. 31, No. 24, 2005, pp. 88–94.

Thermal Stability of Multilayer Contacts on Gallium Nitride

A. E. Belyaev, N. S. Boltovets, V. N. Ivanov, R. V. Konakova*, Ya. Ya. Kudryk, P. M. Lytvyn, V. V. Milenin, and Yu. N. Sveshnikov

Lashkarev Institute of Semiconductor Physics, National Academy of Sciences of Ukraine, Kiev, Ukraine
"Orion" State Research Institute, Kiev, Ukraine
Malachite-ELMA Joint-Stock Company, Moscow, Russia
** e-mail: konakova@isp.kiev.ua*

Received August 8, 2005

Abstract—The results of investigation of a new system of metallization for nonrectifying contacts on *n*-GaN are presented. The new contact metallization system involves the following sequence of layers: Au(200 nm)–Ti(TiB_x)(100 nm)–Al(20 nm)–Ti(50 nm), where the TiB_x layer plays the role of a diffusion barrier. The contacts with the TiB_x layer retain their layer structure and electrical characteristics upon annealing up to 700°C, whereas the usual Au–Ti–Al–Ti structure exhibits degradation upon rapid thermal annealing at $T = 700$°C. Further increase in the annealing temperature to 900°C leads to smearing of the layer structure of the Au–TiB_x–Al–Ti–GaN contact. Physical factors responsible for the change in the parameters of such contact systems are considered. © *2005 Pleiades Publishing, Inc.*

Gallium nitride (GaN)—a wide-bandgap semiconductor with a high carrier mobility and good thermal stability—is a promising material for a broad spectrum of solid-state devices, including those for the microwave frequency range [1–3]. At present, the lack of detailed data on the mechanisms of contact formation and the related physicochemical processes at such interfaces in GaN-based heterostructures is the main factor hindering the realization of their potential advantages. It is important not only to study the characteristic features of these processes, but also to reveal the possibilities for excluding undesired reactions between contacting materials, which detrimentally influence the electrical properties of metal–GaN junctions.

In this context, we have performed a complex investigation into the process of contact formation in multilayer metallization systems of the Au–Ti(TiB_x)–Al–Ti–*n*-GaN–GaN type and established the possible factors influencing the thermal stability of such systems.

Experimental. The experiments were performed with Au–Ti(TiB_x)–Al–Ti–*n*-GaN structures with contact layers manufactured by means of magnetron sputter deposition of the films of metals and a quasi-amorphous TiB_x alloy. The thicknesses of sequential layers in the sample structures were as follows: Au(200 nm)–Ti(100 nm), TiB_x(100 nm), Al(20 nm), and Ti(50 nm). These structures were deposited at 150–200°C onto ~1-μm-thick films of *n*-type GaN with a donor impurity concentration of $\sim 10^{17}$ cm^{-3}, grown on sapphire. Prior to deposition, the film surface was subjected to photon cleaning. After deposition of the Ti and Al layers, the samples were annealed for $t = 30$ s at $T = 900$°C in N_2 atmosphere. Finally, either TiB_x or Ti and Au layers were deposited.

We have studied the samples of two types, representing the test structures and the device structures. Structures of the former type had the form of 5×5-mm samples with continuous metallization layers and were used for structural investigations. The device structures in the form of 100-μm-diam chips were mounted in the standard metal-ruby cases. The mechanisms of contact formation and the stability of contacts with respect to thermal factors were studied using a combination of methods providing mutually complementary information, including Auger electron spectroscopy (AES), atomic force microscopy (AFM), and the measurement of stationary current–voltage (*I–U*) characteristics.

Results and discussion. The *I–U* curves of the contacts showed evidence of an ohmic character and retained their parameters upon the passage from Ti to TiB_x. The values of the contact resistance in these contact structures varied within $\rho_k \approx (1–3) \times 10^{-6}$ Ω cm^2. This result indicates that solid-phase reactions between GaN and the adjacent Al and Ti layers are the main factor ensuring the ohmic character of the contact. The layers of Ti and TiB_x play the role of diffusion barriers.

The same values of contact resistances for the Ti/Al metallization were reported [1, 2] for the structures heat-treated in the optimum regimes. The optimum temperatures of thermal annealing varied within 600–900°C, depending on the method of semiconductor sur-

1063-7850/05/3112-1078$26.00

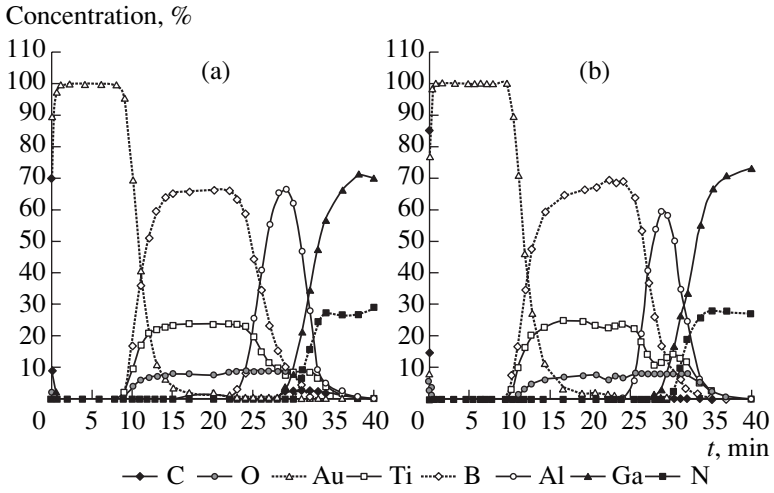

Fig. 1. Elemental composition–depth profiles of Au–TiB_x–Al–Ti–GaN contacts measured by AES in combination with ion-beam sputtering (a) before and (b) after rapid thermal annealing (700°C, 30 s); t is the ion-beam sputtering time.

face preparation, doping level, deposition conditions, and metal layer thickness.

In our experiments, the annealing at 700°C did not change the resistance of contacts with TiB_x layers, but sharply (by 1.5–2 orders of magnitude) increased ρ_k in structures of the second type with a titanium buffer layer. An increase in the contact resistance upon annealing probably reflects a structural and phase disorder of the transition layers formed as a result of the chemical reactions between the metal and semiconductor at the contact interface. The presence of such layers was confirmed by changes in the morphology of metal–semiconductor interfaces upon heat treatment.

The results of investigations of the morphology of the GaN surface by AFM upon removal of the metallization layers are presented in the table. As can be seen, the parameters of the surface roughness observed upon the removal of metallization differ from the corresponding values for the initial substrate surface: all the values exhibit a significant increase, and this growth is more pronounced in the contacts without TiB_x layers.

The annealing leads to an increase in the surface roughness, but this geometric inhomogeneity becomes more pronounced in the contact structures with TiB_x layers. The observed changes in the surface morphology may be caused by two substantially different processes: (i) usual interphase diffusion and (ii) a more complicated process involving the formation and growth of new phases (reactive diffusion).

In order to elucidate the dominating mechanisms involved in the formation of interphase boundaries, we have studied the features of composition profiles in the structures before and after heat treatment. Figure 1 shows the elemental composition–depth profiles of Au–TiB_x–Al–Ti–GaN contacts measured by AES in combination with ion-beam sputtering. The obtained elemental profiles characterize the solid-phase reactions at various interfaces of the contact structures, primarily at the metal–semiconductor junction, which influence the electrical properties of the contacts under consideration.

Based on the published results [1, 2], we believed that reactions of at least three types could predominate

Effect of rapid thermal annealing on the morphology of metal–GaN interfaces

Structure	Treatment	R_q, nm	R_a, nm	R_y, nm
n-GaN–Al_2O_3	Initial	1.4	1.1	24.8
Au–TiB_x–Al–Ti–n-GaN	Initial	12.2	8.4	182.3
Au–TiB_x–Al–Ti–n-GaN	700°C	47.1	36.4	372.4
Au–Ti–Al–Ti–n-GaN	Initial	18.5	14.3	208.8
Au–Ti–Al–Ti–n-GaN	700°C	46	35.2	432.2

Note: Roughness characteristics according to AFM data: R_q is the rms roughness height; R_a is the arithmetic-mean roughness height; R_y is the difference between the highest and lowest points of the surface profile.

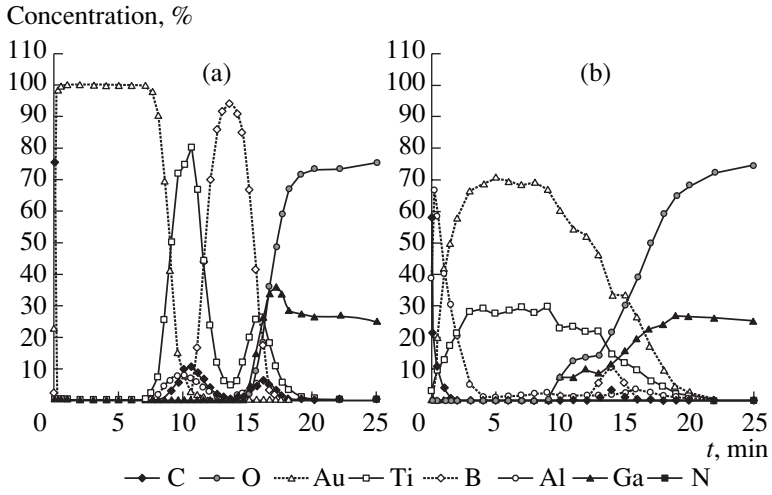

Fig. 2. Elemental composition–depth profiles of Au–Ti–Al–Ti–GaN contacts measured by AES in combination with ion-beam sputtering (a) before and (b) after rapid thermal annealing (700°C, 30 s); *t* is the ion-beam sputtering time.

under the heat treatment conditions studied in our experiments:

$$\mathrm{Ti + GaN \longrightarrow TiN_x + GaN_{1-x}}, \quad (1)$$

$$\mathrm{Al + GaN \longrightarrow Al_xGa_{1-x}N}, \quad (2)$$

$$\mathrm{Ti + 3Al \longrightarrow Al_3Ti}. \quad (3)$$

These reactions must render the interphase boundary chemically inhomogeneous and, hence, increase the structural inhomogeneity as well (see table).

However, the data of AES profiling showed that processes at the interphase boundaries in the structures studied were more complicated than was predicted by Eqs. (1)–(3) and involved the active participation of oxygen species. Evidently, the same complex reactions involving the formation of local oxynitride phases can dominate during the annealing at 700°C and account for the observed increase in the semiconductor surface roughness.

In the course of annealing to 900°C, the layer structure of the contact is additionally smeared due to the contribution of the reactive diffusion component [4]. For comparison, Fig. 2 presents the elemental composition profiles of a contact structure with the TiB_x layer replaced by Ti (of the same thickness), measured before and after the annealing at 700°C. The annealing-induced changes in the layer structure of this contact were comparable with those observed in the structures with TiB_x layers upon the annealing at 900°C.

In conclusion, let us consider in more detail the factors responsible for the formation of nonrectifying contacts in the structures under consideration. As is well known, the conversion of a barrier contact into the nonrectifying one on a semiconductor surface takes place provided that either an enriched (weak barrier) band bending or an ultimately high concentration of the main dopant is created in a subsurface layer of the semiconductor. Apparently, both these factors are operative in the contact structures under consideration.

The chemical bonds in GaN are not purely covalent and, hence, this material obeys the rule according to which semiconductors with a stronger ionic component of the bond form barriers of the Schottky type. Taking into account the work function values of TiN (3.87 eV [5]) and GaN (4.1 eV [6]), we conclude that the potential barrier height in the contact is ≅0.2 eV and cannot account for a low ρ_k, but nevertheless well explains the low values of contact resistances observed in our experiments.

A more preferred model is that involving the formation of a subsurface n^+ layer as a result of solid-phase reactions. It has been demonstrated [7, 8] that, in this case, the formation of a thin interlayer of nitrogen-containing compounds leads to the appearance of a near-surface layer with a high carrier density. For example, a 10-nm-thick TiN layer provides for the predominating tunneling current at the contact, since the carrier density in the adjacent layers amounts to $\cong 10^{20}$ cm^{-3}. Apparently, processes related to the oxidation of reaction products do not significantly influence the mechanism of current transfer (since the doping level remains unchanged), and ρ_k only slightly varies because of an oxidation-induced change of the conductivity of the products of interphase reactions.

Thus, although the ρ_k values in the samples studied somewhat differ (being increased by half an order in magnitude) from the ultimately low values reported for the metal–GaN junctions [9] and are 2–3 times smaller than those observed in the GaN contacts with TiN barriers [10, 11], the contacts under consideration still retain their characteristics upon heat treatments at temperatures above 700°C. Therefore, the use of titanium

borides in metallization systems allows the threshold of thermal degradation of such structures to be significantly increased.

REFERENCES

1. H. Morkoc, *Nitride Semiconductors and Devices* (Springer-Verlag, Berlin, 1999).
2. P. Kordos, in *Proceedings of the 3rd International Euro Conference on Advanced Semiconductor Devices (ASDAM), Smolenice Castle, 2000*, p. 47.
3. M. S. Shur, Solid-State Electron. **42**, 2131 (1998).
4. N. S. Boltovets, V. N. Ivanov, R. V. Konakova, *et al.*, Fiz. Tekh. Poluprovodn. (St. Petersburg) **38**, 769 (2004) [Semiconductors **38**, 737 (2004)].
5. V. S. Fomenko, *Emission Properties of Materials* (Naukova Dumka, Kiev, 1981) [in Russian].
6. V. N. Danilin, Yu. P. Dokuchaev, T. A. Zhukova, *et al.*, "High-Power, High-Temperature, and Radiation Resistant Microwave Devices of New Generation on Broadband AlGaN/GaN Heterostructures," in *Obzory Elektron. Tekhnol., Ser. SVCh Tekh.* (GUP NPP "Pulsar," Moscow, 2001), No. 1 [in Russian].
7. Q. Z. Lin and S. S. Lau, Solid-State Electron. **42**, 677 (1998).
8. Suparna Pal and Takashi Sugino, Appl. Surf. Sci. **161**, 263 (2000).
9. Mohammad S. Noor, J. Appl. Phys. **95**, 7940 (2004).
10. E. Kaminska, A. Piotrowska, M. Guziewicz, *et al.*, Mater. Res. Soc. Symp. Proc. **449**, 1055 (1997).
11. S. E. Mohney, B. P. Luther, S. D. Wolter, *et al.*, in *Proceedings of the 4th International High Temperature Electronics Conference (HiTEC), Albuquerque, 1998*, p. 134.

Translated by P. Pozdeev

Technical Physics Letters, Vol. 31, No. 12, 2005, pp. 993–996. Translated from Pis'ma v Zhurnal Tekhnicheskoĭ Fiziki, Vol. 31, No. 23, 2005, pp. 1–7.

Photoluminescence of Heterostructures with Highly Strained $Ga_{0.76}In_{0.24}As$ Quantum Wells Separated by $GaAs_yP_{1-y}$ Compensating Barriers

V. V. Shamakhov, D. A. Vinokurov*, A. L. Stankevich, V. A. Kapitonov, S. A. Zorina, D. N. Nikolaev, A. V. Murashova, A. D. Bondarev, and I. S. Tarasov

Ioffe Physicotechnical Institute, Russian Academy of Sciences, St. Petersburg, 194021 Russia

** e-mail: dmitry.vinokurov@pop.ioffe.rssi.ru*

Received June 22, 2005

Abstract—Based on the results of model calculations and the data of photoluminescence measurements and transmission electron microscopy, the optimum composition ($GaAs_{0.85}P_{0.15}$) of compensating barriers for a structure with four highly strained $Ga_{0.76}In_{0.24}As$ quantum wells (QWs) has been established that excludes the relaxation of elastic stresses in these QWs. Laser heterostructures with four such QWs separated by said compensating barriers have been grown by means of hydride metalorganic chemical vapor deposition. Laser diodes with short (~100 μm) resonators based on these heterostructures operate at $\lambda = 1060$ nm with an output radiation power of 100 mW in the continuous regime. © *2005 Pleiades Publishing, Inc.*

Single-frequency semiconductor lasers can be obtained using different approaches, including distributed feedback, composite resonator, external grating, and a combination of laser, optical fiber, and Bragg grating [1]. Stable single-mode operation of such lasers is achieved for devices with small (below 200 μm) resonator lengths. In order to provide for the maximum gain under these conditions, active regions are created based on heterostructures with quantum wells (QWs) [2]. In semiconductor lasers intended for the operation at wavelengths above 1000 nm, such active regions are usually obtained using highly strained solid solutions of the $Ga_xIn_{1-x}As$ system. It is important to eliminate the relaxation of stresses in the structures with QWs, since this is accompanied by the formation of dislocations leading to deterioration of the optical characteristics of laser diodes. This problem can be solved by introducing barriers capable of compensating for strains in the active region.

This paper reports the results of investigation of the photoluminescence (PL) of laser heterostructures with four highly strained $Ga_{0.76}In_{0.24}As$ quantum wells separated by $GaAs_yP_{1-y}$ compensating barriers with various compositions in the range $0.85 \le y \le 1$. Based on the obtained data, we have selected the optimum composition of the compensating barrier, which excludes the relaxation of elastic stresses in these QWs.

The samples for the PL investigation were prepared in an Encore GS3100 metalorganic chemical vapor deposition (MOCVD) system with a vertical reactor. The growth was carried out at a reduced pressure (77 Torr), a substrate holder rotation rate of 1000 rpm, and a substrate temperature of 700°C. The undoped heterostructures grown on (100)-oriented *n*-GaAs substrates consisted of $Al_{0.3}Ga_{0.7}As$ emitter layers, GaAs waveguide layers, and active regions. The active region contained four $Ga_{0.76}In_{0.24}As$ quantum wells with $\Delta a/a = 1.7 \times 10^{-2}$ and a thickness of 10 nm, separated by three 32-nm-thick $GaAs_yP_{1-y}$ compensating barriers with $0.85 \le y \le 1$, so that the total active region thickness was about $H = 136$ nm. The compositions of $GaAs_yP_{1-y}$ solid solutions in the compensating barriers were determined from the data of high-resolution X-ray diffraction measurements.

We have calculated the critical thickness H_c of the active region for the $GaAs_yP_{1-y}$ compensating barriers of various compositions. The calculations were performed using a formula based on the transcendental Matthews equation [3, 4]:

$$H_c = \frac{b(1-\nu\cos^2\varphi)}{2\pi f(1+\nu)\sin\varphi\cos\theta}\left(\ln\frac{H_c}{b\sin\theta}+1\right), \qquad (1)$$

where b is the Burgers vector, ν is the Poisson ratio, φ is the angle between the Burgers vector and the line of misfit dislocation ($\varphi = 60°$), θ is the angle between the slip plane and the interface ($\theta = 54.74°$), and f is the

1063-7850/05/3112-0993$26.00 © 2005 Pleiades Publishing, Inc.

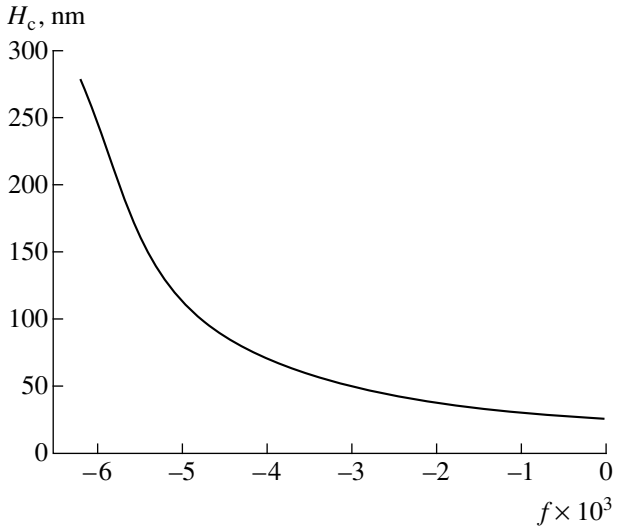

Fig. 1. A plot of the critical thickness H_c of the active region versus lattice mismatch f between the GaAs substrate and the $GaAs_yP_{1-y}$ compensating barrier, calculated for heterostructures with four $Ga_{0.76}In_{0.24}As$ quantum wells grown at 700°C.

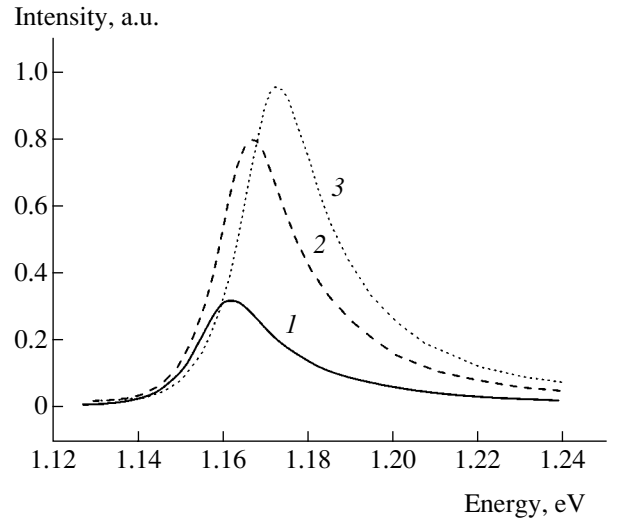

Fig. 2. Room-temperature PL spectra of the heterostructures with $GaAs_yP_{1-y}$ compensating barriers of various compositions corresponding to $y = 1$ (*1*), 0.92 (*2*), and 0.85 (*3*).

mismatch of the lattice periods of the epitaxial layer and substrate.

Since formula (1) was originally obtained for the critical thickness of a single layer, whereas the active region in our case has a multilayer structure, we replace the parameter f with an equivalent lattice mismatch f_{eq}, which implies that the multilayer active region is modeled by a single layer with an effective averaged mismatch of the lattice periods. The equivalent lattice mismatch f_{eq} is defined in terms of the equivalent strain ε_{eq} and determined as $f_{eq} = -\varepsilon_{eq}$, where ε_{eq} is given by the formula

$$\varepsilon_{eq} = \frac{n\varepsilon_1 h_1 + m\varepsilon_2 h_2}{nh_1 + mh_2}. \quad (2)$$

Here, n and m are the numbers of QWs and compensating barriers in the active region, respectively; ε_1 and ε_2 are the strains of the QW and the compensating barrier, respectively; and h_1 and h_2 are the thicknesses of the QW and the compensating barrier, respectively. The strains of the QW and the compensating barrier were determined as

$$\varepsilon_i = \frac{a_{sub} - a_i}{a_i}, \quad (3)$$

where a_{sub} is the lattice period of the substrate and a_i is the lattice period of the ith layer (i.e., of the QW or the adjacent compensating barrier) of the active region in the unstrained state.

Figure 1 presents the calculated plot of the critical thickness H_c of the active region at 700°C as a function of the lattice mismatch f between the GaAs substrate and the $GaAs_yP_{1-y}$ compensating barrier. As can be seen, H_c increases with the level of compensating stresses, that is, with the content of phosphorus in the $GaAs_yP_{1-y}$ solid solution. For a $GaAs_yP_{1-y}$ barrier layer with the composition $y \approx 0.855$, which corresponds to a lattice mismatch of $f \approx -5.2 \times 10^{-3}$, the calculated critical thickness is equal to a preset value of 136 nm. Therefore, active regions containing compensating barriers with the compositions $GaAs_yP_{1-y}$ corresponding to $y \le 0.855$ (and $f \le -5.2 \times 10^{-3}$) have thicknesses below the critical value ($H \le H_c$). This implies that QWs separated by such $GaAs_yP_{1-y}$ compensating barriers do not exhibit relaxation of elastic stresses and, hence, the formation of misfit dislocations capable of significantly deteriorating the optical characteristics of laser diodes.

In order to check the results of model calculations, we studied the PL characteristics of epitaxial heterostructures with various compositions of $GaAs_yP_{1-y}$ compensating barriers, corresponding to $y = 1$ (structure 1), 0.92 (structure 2), and 0.85 (structure 3). Figure 2 shows the PL spectra of these structures measured at $T = 300$ K. As can be seen, the PL intensity grows with the level of compensating stresses, which increases on the passage from structure 1 to structure 3. We believe that this behavior is related to the fact that an increase in the level of compensating stresses in the barriers is accompanied by a decrease in the degree of relaxation of the elastic stresses in QWs and, hence, in

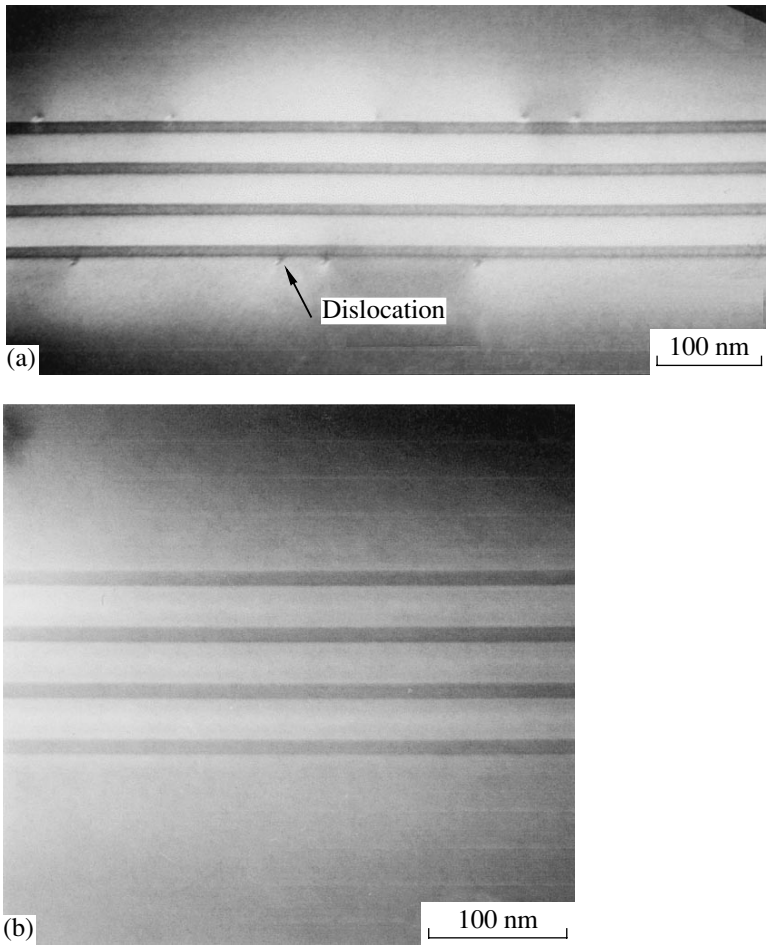

Fig. 3. TEM images of the transverse sections of heterostructures containing multilayer active regions of with compensating barrier compositions (a) GaAs and (b) $GaAs_{0.85}P_{0.15}$. The arrow indicates a misfit dislocation formed a result of stress relaxation at the interface.

the number of structural defects. This assumption was additionally confirmed by significant variations in the intensity of PL spectra measured at different points of the samples of structures 1 and 2. The degree of inhomogeneity of the PL intensity decreased with increasing level of compensating stresses and vanished in the case of structure 3. From the entire set of data presented above, we infer that structure 3 with $GaAs_yP_{1-y}$ compensating barriers with the composition $y \approx 0.85$ does not feature the relaxation of elastic stresses, in agreement with the results of theoretical calculations of the critical thickness of the active region.

The results of PL measurements were also consistent with the data obtained using transmission electron microscopy (TEM). Figure 3 shows the typical TEM images of the transverse sections of the active region for the heterostructures with compensating barrier compositions GaAs and $GaAs_{0.85}P_{0.15}$. As can be seen, the structure with GaAs barriers (Fig. 3a) contains dislocations (imaged as dark spots) in the active region, whereas the structure with $GaAs_{0.85}P_{0.15}$ barriers (Fig. 3b) is free of dislocations.

Taking into account the obtained data, we have grown laser heterostructures with the optimum composition and fabricated laser diodes based on these heterostructures. The laser diodes with 100-μm-ling resonators operated at 1060 nm with an output radiation power of 100 mW in the continuous lasing regime.

To summarize, we have selected, based on the PL and TEM data, the optimum composition ($y \approx 0.85$) of $GaAs_yP_{1-y}$ compensating barriers in the heterostructure with highly strained $Ga_{0.76}In_{0.24}As$ quantum wells, which prevents the relaxation of elastic stresses in the QWs. The obtained experimental data agree well with the results of theoretical calculations performed within the framework of the Matthews model using the equivalent lattice mismatch parameter (f_{eq}) for the multilayer active region. Using the selected structure, it is possible to obtain laser diodes with small resonator lengths, which operate at $\lambda = 1060$ nm and possess high output characteristics.

Acknowledgments. The authors are grateful to M.A. Yagovkina for carrying out the X-ray diffraction investigation and to Yu.G. Musikhin for conducting the PL measurements.

This study was supported in part by the Russian Foundation for Basic Research (project no. 04-02-17641), the St. Petersburg Administration Program of Research and Technological Activities, and the program of the St. Petersburg Scientific Center of the Russian Academy of Sciences.

REFERENCES

1. M. Ziari, J.-M. Verdiell, J.-L. Archambault, *et al.*, in *Proceedings of the Conference on Lasers and Electro-Optics (CLEO-97), Baltimore, 1997.*
2. L. A. Coldren and S. W. Corzine, *Diode Lasers and Photonic Integrated Circuits* (Wiley, New York, 1995).
3. J. W. Matthews, S. Mader, and T. B. Light, J. Appl. Phys. **41**, 3800 (1970).
4. J. W. Matthews, J. Vac. Sci. Technol. **12**, 126 (1975).

Translated by P. Pozdeev

Technical Physics Letters, Vol. 31, No. 12, 2005, pp. 997–1000. Translated from Pis'ma v Zhurnal Tekhnicheskoĭ Fiziki, Vol. 31, No. 23, 2005, pp. 8–16.

Heteropolytype Structures with SiC Quantum Dots

A. A. Lebedev, V. N. Petrov, A. N. Titkov, L. M. Sorokin*, A. S. Tregubova, G. N. Mosina, A. E. Cherenkov, and M. P. Shcheglov

Ioffe Physicotechnical Institute, Russian Academy of Sciences, St. Petersburg, 194021 Russia

** e-mail: lev.sorokin@mail.ioffe.ru*

Received August 15, 2005

Abstract—Epitaxial silicon carbide layers of 3C-SiC polytype with an array of nanodimensional SiC quantum dots (QDs) have been obtained for the first time using an improved method of sublimation epitaxy in vacuum. The X-ray topography and X-ray diffraction data unambiguously confirm the formation of a 3C-SiC epilayer with twinned regions on the surface of a 6H-SiC substrate. The surface topography of epilayers was studied by atomic force microscopy (AFM), and the microstructure of a near-surface layer of the deposit was investigated by transmission electron microscopy (TEM). Using the AFM and TEM data, the presence of QDs (representing SiC nanoislands) is established, and their average dimensions and concentration are evaluated. © *2005 Pleiades Publishing, Inc.*

As is known, silicon carbide (SiC) crystallizes in various modifications, called polytypes, which have the same stoichiometric chemical composition but may significantly differ in physical properties. For example, the bandgap width ranges from 2.4 eV in 3C-SiC to 3.3 eV in 2H-SiC.

Previously, we demonstrated [1] that 3C-SiC epilayers with highly perfect structure can be grown using the method of sublimation epitaxy in vacuum (SEV) on 6H-SiC substrates. Diode heterostructures based on such epilayers were obtained, and their electrical properties were studied [2].

This paper presents the results of investigations devoted to the further development of the sublimation growth technology with the aim of obtaining nanodimensional islands of a cubic SiC polytype inside a matrix of hexagonal polytypes.

The growth of 3C-SiC on the surface of a hexagonal SiC substrate in the case of SEV proceeds due to a greater partial pressure of Si vapor in the growth zone. An increase in the Si/C atomic ratio leads to an increase in the number of twins in the 3C-SiC epilayer, while the area of each twin tends to decrease. This behavior is indicative of the large number of 3C-SiC nuclei simultaneously formed on the surface of the hexagonal substrate in the initial stage of the epitaxial process. In order to obtain small-size 3C-SiC inclusions (quantum dots, QDs) inside a hexagonal matrix, it is necessary that (i) the rate of the epitaxial growth of 3C-SiC be relatively low and (ii) the technological conditions on the subsequent stages favor the growth of a hexagonal SiC polytype. The latter implies that it is necessary to provide for a rapid decrease in the Si/C atomic ratio in the growth zone. Low growth rates in the SEV technology are achieved by decreasing the temperature gradient between the source and substrate [3].

We succeeded in obtaining 3C-SiC quantum dots in a hexagonal SiC matrix using an experimental technological scheme which stipulated the following:

(i) Preparation of a source ensuring sufficiently high pressure of Si vapor in the initial stage of epitaxial growth.

(ii) Conducting the growth at a small temperature gradient between the source and substrate so as to ensure sufficiently slow growth of epilayers.

(iii) A sharp increase in the growth cell temperature, which is accompanied by rapid evaporation of Si from the source and the resulting decrease in the Si/C ratio in the growth zone.

The crystal structure and surface topography of the grown epilayers were studied using X-ray diffraction, X-ray topography, atomic force microscopy (AFM), and transmission electron microscopy (TEM). The X-ray topographs were measured in the backscattering geometry using CuK_α radiation and the asymmetric (311) or (331) reflections, which provided the optimum conditions for revealing the regions of 3C-SiC polytype in the epilayer by means of the orientation contrast. These regions are imaged on the topographs as spots of dark or bright contrast with various dimensions, representing an epilayer structure composed of twins misoriented by 60° relative to each other. Accordingly, a 60° azimuthal rotation of the crystal results in inversion of the contrast of regions on the X-ray topograph.

Figure 1 shows the typical X-ray topograph measured in the (311) reflection for a 3C-SiC epilayer grown on an (0001)6H-SiC substrate. This pattern confirms that the entire growth surface with an area of ~1 cm^2 is covered by a continuous 3C-SiC layer composed of twinned regions with dimensions ranging from ~1 mm^2 to substantially smaller ones. High-reso-

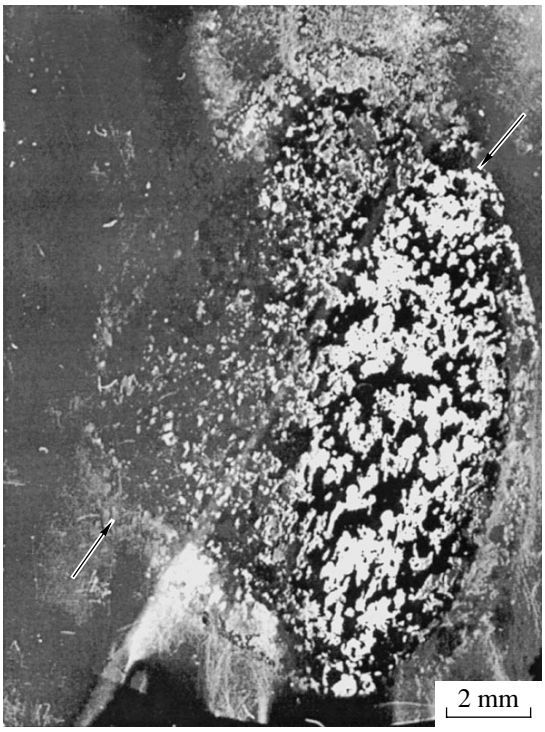

Fig. 1. The typical X-ray topograph measured in the (311) reflection: the oval region represents a 3C-SiC epilayer grown on an (0001)6H-SiC substrate (arrows indicate the boundaries of the epilayer).

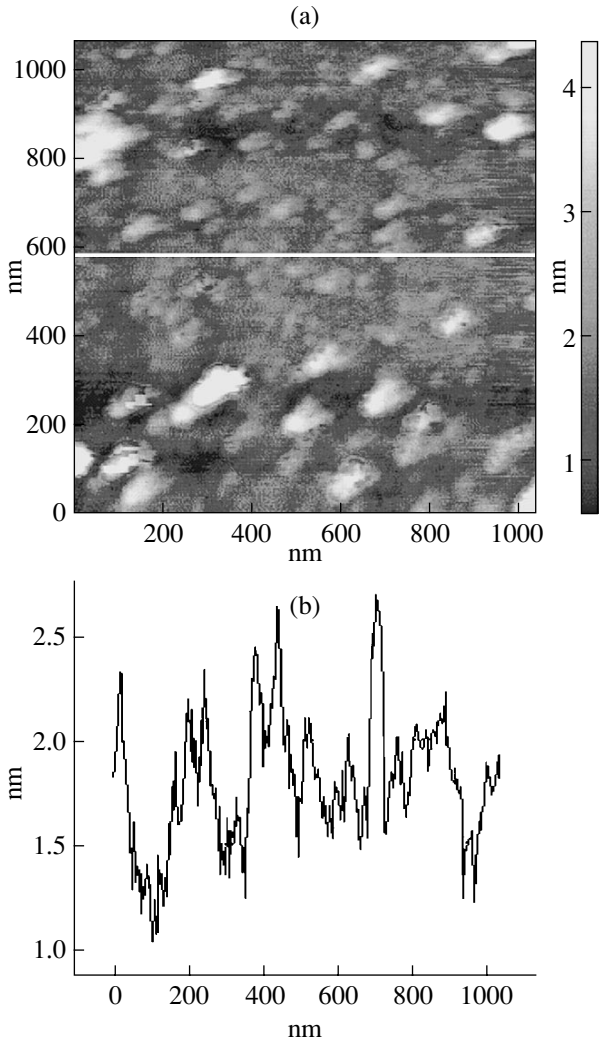

Fig. 2. (a) The typical AFM image of the growth zone, with QD-like objects in the central region; (b) the surface profile measured from left to right along the white line in Fig. 2a, which shows that QDs have a height of about 1 nm and lateral dimensions below 50 nm.

lution AFM and TEM measurements (see below) revealed the presence of nanodimensional islands, apparently, of the 3C-SiC polytype.

The X-ray diffraction measurements performed in the two-crystal geometry unambiguously confirmed the presence of epilayers with the 3C-SiC polytype structure on 6H-SiC substrates. The full width at half maximum (FWHM) of the rocking curves measured using CuK_α radiation for the (00012)6H-SiC and (111)3C-SiC reflections was 30 and 40 seconds of arc, respectively. This difference is related to an insignificant bending of the samples as a result of the epitaxial layer growth. The bending is also manifested in the X-ray topographs.

The surface topography of SiC epilayers on a nanometer scale was studied by AFM. The AFM measurements were performed in air using a P-47 SEMI instrument (NT-MDT company) with platinum-coated silicon probes. The AFM data revealed several characteristic features in the surface topography of SiC epilayers and showed a significant difference of this topography from that of the substrate.

As is known, the preparation of 6H-SiC substrates for the subsequent epitaxial growth is a complicated procedure, which has not yet been completely elaborated. The surface topography of 6H-SiC substrates exposed to atmosphere is characterized by a pattern of closely spaced hills, each with a height of up to several nanometers and a diameter within several tens of nanometers. Approximately such a topography, with nanodimensional hills having an average diameter of about 20 nm and a height of 1–2 nm, was observed for our 6H-SiC substrates.

The surface topography of SiC epilayers was different from that of the substrates. The observed patterns were of two types. In one of these, the X-ray topographs exhibited a regular arrangement of atomically smooth terraces, which covered the entire observed field with an area of up to several tens of square microns. The terraces were several microns long and 200- to 400-nm wide and had a height of about 0.2 nm, which is close to the length of Si–C bonds (0.187 nm). These structural parameters allowed us to interpret the surface topography of the first type as belonging to an

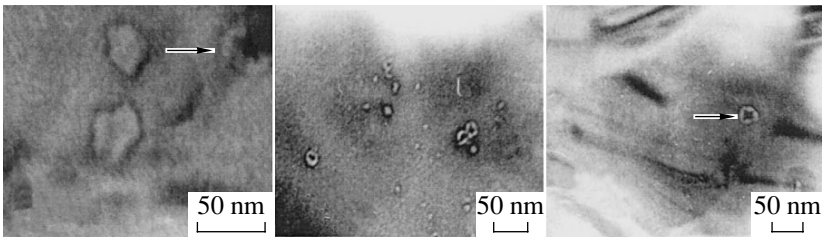

Fig. 3. TEM micrographs showing the defect structure of a near-surface region of SiC epilayers. Arrows indicate nanoislands appearing as the typical quantum dots.

epitaxial film of the hexagonal 6H-SiC phase grown on the substrate surface. The relative fraction of such regions on the epilayer surface did not exceed several percent.

Most of the surface of SiC epilayers exhibited topographs of a different type, where the aforementioned flat terraces were absent. The surface was characterized by a general roughness on a level of 0.5 nm and contained separate nanodimensional islands with a height of 1–3 nm and an average diameter of 50 nm (Figs. 2a and 2b). These islands did not reproduce the structure of the substrate surface and were definitely of growth origin. In some cases, the symmetry of islands was distorted and they appeared elongated in a certain common direction. The elongated islands had a height of up to 5 nm, a width up to 150 nm and a length up to 600 nm.

The samples for electron-microscopic investigation were prepared from the same region of the epilayer that was studied by AFM. The samples for TEM measurements were thinned by conventional methods from 0.25 mm to a thickness transparent for 100-keV electrons and then cut by scribing to a size corresponding to the standard TEM sample holder. The growth surface of the epilayer was protected from contamination and mechanical damage by a wax layer, and the samples were ground from the side of the 6H-SiC substrate surface by dimpling to a thickness of 15–20 μm in the central region of the meniscus. Then, the wax layer was removed by repeated washing with toluene and ethyl alcohol, and the samples were further thinned by ion-beam etching (Ar^+ ions, $U = 5$ kV, $I = 10$ μA) from the substrate side until the appearance of perforation sites at the center of the beam spot.

Figure 3 presents a series of TEM micrographs obtained in the diffraction contrast mode (two-beam approximation). The images, displaying separate nanodimensional objects present in a SiC epilayer, reveal a complicated internal structure of this layer. In most cases, such nanoislands comprise a dark nucleus surrounded by a bright region, which is bounded by a thin dark ring. The presence of a bright region around the central nucleus is indicative of a somewhat smaller sample thickness in this region. Analogous regions surrounding QDs are called trenches [5]. The dimensions of nanoislands fall within ~15–20 nm, and their surface concentration varies from 1×10^8 to 1×10^9 cm^{-2}.

The images of two nanoislands indicated by arrows in Fig. 3 display dark nuclei, one having the shape of a cross and another, of a six-arm star. These patterns resemble the images of QDs observed in a GaAs/GaAlAs system [5]. On these grounds, we may ascertain that the electron micrographs presented in Fig. 3 reveal nanoislands formed on the surface of a SiC epilayer. The patterns of electron microdiffraction from the corresponding regions showed that the epilayer represents the 3C (cubic) polytype of SiC with a (111) orientation. We have also prepared and studied the transverse sections of the substrate–epilayer junctions, but the results of these measurements did not provide additional information.

Figure 4 presents TEM images showing the objects of another type. In some cases, these objects appear as central triangles surrounded by homogeneous regions of a darker contrast as compared to that observed for the epitaxial layer. We may suggest that these images reveal nanoparticles of the 3C-SiC polytype occurring at a certain depth inside the epilayer rather than on its surface.

A comparison of the structural data obtained by different analytical methods leads to the conclusion that an array of nanoislands, probably with a structure of the

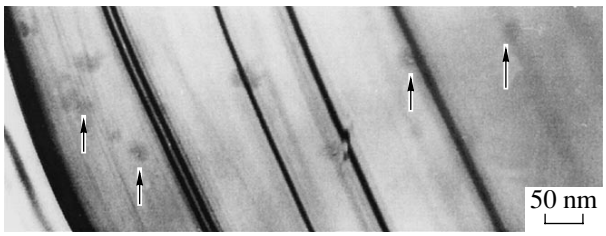

Fig. 4. The TEM image of the region of a SiC epilayer with nanoislands (indicated by arrows) surrounded by the characteristic regions of dark contrast. The inclined dark bands are the extinction contours related to bending of a thin sample.

3C-SiC polytype, is formed on the surface of a 3C-SiC epilayer. It is also possible that some of these 3C-SiC nanoislands can be overgrown by an epilayer of 6H-SiC or 3C-SiC polytypes. At present, there is no convincing structural data for judging between these possibilities, although the photoluminescence spectra of the samples of such structures were similar to the spectra of 3C-SiC/6H-SiC heterostructures [4], which is evidence in favor of the former (6H-SiC) polytype. Elucidation of the mechanisms of growth of SiC epilayers with arrays of SiC nanoislands, both surface and overgrown, requires additional investigations.

Acknowledgments. This study was supported by the Russian Foundation for Basic Research, project nos. 03-02-16054b and 04-02-01-6632a.

REFERENCES

1. A. A. Lebedev, G. N. Mosina, I. P. Nikitina, *et al.*, Pis'ma Zh. Tekh. Fiz. **27** (24), 57 (2001) [Tech. Phys. Lett. **27**, 1052 (2001)].
2. A. A. Lebedev, A. M. Strel'chuk, D. V. Davydov, *et al.*, Pis'ma Zh. Tekh. Fiz. **28** (18), 89 (2002) [Tech. Phys. Lett. **28**, 792 (2002)].
3. N. S. Savkina, A. A. Lebedev, D. V. Davydov, *et al.*, Mater. Sci. Eng., B **77**, 50 (2000).
4. A. A. Lebedev, D. K. Nel'son, B. S. Razbirin, *et al.*, Fiz. Tekh. Poluprovodn. (St. Petersburg) **39**, 1236 (2005) [Semiconductors **39**, 1194 (2005)].
5. B. Cockayne *et al.*, in *Proceedings of the Conference on Microscopy of Semiconducting Materials, Oxford, 2001*; Inst. Phys. Conf. Ser., No. 192, Section 10, p. 376.

Translated by P. Pozdeev